Investigation of the Cavitation Bubble Oscillation Period During Laser Shock Peening

Nicholas J. Stiekema

Student number: 675563
Supervisor: Prof. C. Polese
Co-Supervisor: Dr D. Glaser

A dissertation submitted to the Faculty of Engineering and the Built Environment, University of the Witwatersrand, Johannesburg, in fulfilment of the requirements for the degree of Master of Science in Engineering.

Johannesburg, May 2021

Declaration

I declare that this dissertation is my own, unaided work, except where otherwise acknowledged. It is being submitted for the degree of Master of Science in Engineering in the University of the Witwatersrand, Johannesburg in the year 2021. It has not been submitted before for any degree or examination at any other university.

Signed this 21st day of May 2021

Nicholas J. Stiekema

Acknowledgements

I would like to thank the following persons:

Prof. Claudia Polese for her continued and generous guidance, support and understanding.

Dr Daniel Glaser for his patience, advice, sandwiches, phone calls, knowledge in all things lasers and help within the lab.

Mr Herman Rossouw for his willing and enthusiastic help with cables, signals and all things related to electronics in the lab.

All those at the National Laser Centre in the CSIR, who allowed me to use the lasers.

Dr Randall Paton for the extended loan of a pressure transducer.

Mr Shaun Riekert and the workshop staff in the Mechanical Engineering Workshop at Wits, for all the manufacturing assistance, machining jobs, advice and good banter.

Mrs Marina Labuschagne for all the generous guidance and help in Wits administration.

All those who arduously proof-read the drafts; Prof. Polese, Dr Glaser, Lior Sinai, Francesco Pietra, Sean van Staden, Hilton Goodhead, John Stiekema.

Rena João for her encouragement, love and support through the course of this degree and beyond.

My parents and family, for doing so much more than just keeping me alive.

God Almighty for creating the observed phenomena, as well this observer.

The Rental Pool Programme, funded by the Department of Science and Innovation (DSI) that covered transportation costs and enabled the academic use of lasers at the CSIR.

Wits Commercial Enterprise for supporting prior studies, upon which this research is built.

DSI-NRF Centre of Excellence in Strong Materials (CoE-SM) for the generous financial and administerial support, without which this dissertation could not be possible.
Opinions expressed and conclusions arrived at are those of the author and are not necessarily to be attributed to the CoE-SM.

Abstract

Laser Shock Peening (LSP) under a thick water confinement layer produces cavitation bubbles that rapidly expand and collapse emitting at least two shock waves in the surrounding water. The time between the first shock (laser pulse) and the second shock (first bubble collapse) is understood as the first bubble oscillation period or bubble lifetime and is evaluated here for use as a real time process diagnostic in the LSP process. Within this study, it was found that first bubble oscillation periods could be correlated to an increasing laser power intensity up to $6\,\mathrm{GW/cm^2}$. Thereafter, systematic saturation in laser energy transfer occurs. The saturation, apparent in all tests above this power intensity, is attributed to the laser energy being absorbed in dielectric breakdown of the water before reaching the target. The stability of bubble lifetimes was most appreciably improved with the presence of flowing water along the beam path. The target geometry (corners, cavities, semi-cylinders) produced an overall change (increase or decrease) in cavitation bubble lifetime that is present regardless of beam energy, water flow or laser pulse rate. Promising applications for this diagnostic at present would be in cases of unchanging or predictable target geometries such as large flat or uniform panels (pressure vessels and aircraft skin structures) with the use of high water flow rates to maintain the confinement layer along the beam path.

Contents

Declaration i

Acknowledgements ii

Abstract iii

Contents iv

List of Figures ix

List of Tables xvi

List of Symbols xviii

List of Acronyms xix

1 Introduction 1

1.1 Laser Shock Peening in South Africa 1

1.2 Cavitation Bubble as a Process Diagnostic 2

2 Literature Survey 4

2.1 Laser Shock Peening 4

2.1.1 Residual Stress Treatment 4

2.1.2 Process Mechanism 5

2.2 Confinement 7

2.3 Cavitation 10

2.4 Cavitation in LSP 11

2.4.1 Cavitaton Bubbles near Geometry 12

2.5 LSP Cavitation Diagnostic 13

2.5.1 Cavitation Energy 15

2.6 Other Diagnostics 18

2.6.1 Acoustic Emission Measurement 19

2.6.2 Plasma Emission Spectrum 21

2.7 Literature Summary 22

3 Research Question and Objectives **23**

4 Apparatus **24**

4.1 Laser 24

4.2 Energy Meter 26

4.3 Test Samples and Articulation 26

4.3.1 3D Printer 27

4.4 Water Tank 28

4.5 Measurement System 30

4.6 Transducer 31

4.7 High Speed Camera 32

4.8 Full Experimental Overview 32

5 Methodology **34**

5.1 Producing Observable Cavitation Bubbles . . . 34
5.1.1 Operating the Laser . . . 34
5.1.2 Water Tank Preparation . . . 34
5.1.3 Measuring the Spot Size . . . 35
5.2 Measure Cavitation Bubbles . . . 38
5.2.1 Observing with High Speed Images . . . 38
5.2.2 Observing Pressure Data . . . 41
5.3 Measure First Bubble Oscillation . . . 42
5.4 Testing Industry Conditions . . . 43
5.5 Experimental Outline . . . 44
5.6 Broad Test Procedure . . . 47

6 Data Processing **48**

6.1 Peak Detection . . . 48
6.2 Flow Velocity . . . 50
6.3 Uncertainty Analysis . . . 50
6.3.1 Design Stage Uncertainty Analysis . . . 51
6.3.2 Uncertainty of Multiple Data Points . . . 51
6.3.3 Uncertainty of Terms within Bubble Energy . . . 53
6.4 Sampling . . . 54
6.5 DAQ Voltage Calibration for Energy . . . 56

7 Results and Discussion **58**

7.1 Data Collection Assessment 59
7.1.1 Spot Size Variation 59
7.1.2 Pressure Measurement 60
7.1.3 Transducer Characteristics 61
7.1.4 Transducer Pressure Uncertainty 64
7.2 Stagnant Water Tests 67
7.3 Effect of Repetition Rate and Laser Energy on Cavitation Bubbles 74
7.4 Effect of Test Duration 78
7.5 Tests in Tap Water 81
7.6 Tests in a Tube of Water 84
7.6.1 Flow at Low Repetition Rates 85
7.6.2 Further Flow Tests 88
7.6.3 Process Control Chart 89
7.6.4 Bubble Lifetime Saturation 90
7.7 Near Edge Effect 93
7.8 Geometrical Boundary Effects 99
7.8.1 Explanation of Experiment 99
7.8.2 Bubble Lifetime Observations 101
7.8.3 Discussion 104
7.8.4 High Speed Image Observations 105
7.8.5 Discussion 106
7.9 Experimental Summaries 109

8 Discussion **112**

8.1 Objectives Achieved 112

8.2 Unexpected Results 113

8.3 Limitations 114

8.4 Findings 116

9 Conclusions **117**

10 Recommendations **118**

References **119**

A Appendix **127**

A.1 Data Acquisition Uncertainty Analysis 127

A.1.1 Laser Energy Uncertainty 128

A.1.2 Uncertainty of Pressure Transducer 129

A.1.3 Sequential Perturbation 130

A.1.4 Sequential Perturbation of Bubble Energy 131

A.2 Marlin Firmware Modifications 134

A.3 GCODE Run on the 3D Printer 136

A.4 MATLAB Scripts 137

A.5 Laser SOP 138

List of Figures

1.1 The lifetime of a laser induced cavitation bubble [7]. 2

1.2 A prototype of the patent hardware and anticipated pressure pulses [14]. . . . 3

2.1 Fatigue life curves for untreated, shot peened and laser shock peened 7074 aluminium alloy [2]. 5

2.2 The process of LSP; shock waves create plastic deformation, inducing a compressive residual stress field on and below the surface. 5

2.3 Micrograph cross section of AZ31B Mg alloy showing grain refinement after Laser Shock Peening (LSP) impacts [20]. 6

2.4 Residual stress profiles for LSP treated Ti-6Al-4V samples at different power intensities [22]. 7

2.5 An illustration of thin water LSP alongside an image of the process. 8

2.6 The variation of peak pressure with laser power intensity for different target thicknesses. The laser was at 532 nm [27]. 8

2.7 The variation of peak pressure with laser intensity for different laser wavelengths after [31]. 9

2.8 Vortex cavitation on a hydrofoil tip, an example of hydrodynamic cavitation [34]. 10

2.9 Laser induced plasma in open water, creating a shock wave (outer ring) that surrounds a growing cavitation bubble (tear drop shaped cavity) [35]. 11

2.10 Laser induced cavitation growth and collapse under 5 mm of water [36]. 11

2.11 The formation of a laser induced cavitation bubble [37]. 12

2.12 The bubble lifetime is extended near flat and concave boundaries. 13

2.13 Water spray typically contaminates the beam path, limiting beam measurements to before the final window/lens. 14

2.14 Signal from hydrophone of the laser breakdown and cavitation bubble collapse [41]. 2T_{c_1} is the whole bubble lifetime. The largest bubble radius occurs at T_{c_1} after initial spike. 15

2.15 Signals from a PVDF transducer immediately after the laser induced plasma and at the bubble collapse [43]. 15

2.16 Energy balance of laser induced breakdown in water [44]. 17

2.17 Prior innovations in LSP monitoring, at different points in the LSP process. . 18

2.18 Non destructive evaluation patent. Adapted from [60]. 20

2.19 Experimental results of a submerged sample from Enoki et al. [28]. 20

2.20 Detected AE waveforms during laser shock peening. [61]. 21

2.21 Photomultiplier tube voltage responding to the emission levels of 455 nm light at different laser energy densities [13]. 21

4.1 CR20 Pro 3D printer from Creality [68]. 27

4.2 Image of filled tank with inlet and outlet pipes within the 3D printer frame, viewed through glass panes above the high speed camera. 29

4.3 Complete pressure measurement system. 30

4.4 Zener clipper circuit, limits the voltage across the output. V_{ZD} is 10 V [70]. . 31

4.5 Photograph of the tank showing the 3D printer articulating an almen strip target, a submerged transducer, high speed camera and light source viewed from above. 32

4.6 Image of filled tank showing inlet and outlet pipes, 3D printer articulating the target and a submerged transducer, high speed camera, beam path mirrors and lens on precision slide, conductivity meter, PC. 33

4.7 Layout of the complete experimental laser induced cavitation bubbles system. 33

5.1 The spot size of a single test, measured from an average of seven spots. 37

5.2 Relationship between the measured lengths and actual lengths was calibrated 37

5.3 Illustration of the main measured experimental parameters. 38

5.4 Clear tape focal plane, being exposed to the laser. This tape was the reference centre plane of the laser beam path. 40

5.5 Screen shot of the LabVIEW Virtual Instrument (VI) application window. . . 41

5.6 The pressure information can be shown to represent the reality seen in pictures [7, 61]. The bubble energy is dependent on the time between the two pressure spikes raised to the third power, in Equation 2.6. 42

6.1 The general method by which peaks are found using the `findpeaks` function in MATLAB. Other features of this function such as peak width are not used [74]. 49

6.2 Procedure for combining multiple measurements [75]. 51

6.3 Uncertainty of calculated bubble energy associated with varying bubble lifetimes and bubble energy. This study produced bubble lifetimes not larger than 1.6 ms. 54

6.4 Shock wave passing transducer. 55

6.5 Diagram of voltage energy relationship within the data acquisition system. . . 56

7.1 Summary of the experiments undertaken. 58

7.2 Spot sizes over the course of the testing period. Each point represents an average of at least four spots, error bars are the measurement uncertainty of that average. 59

7.3 Comparison of different shock waves defining a single bubble's first oscillation period or lifetime. 60

7.4 Shape of laser induced (left) and cavitation collapse (right) shock waves. . . . 62

7.5 Waveform of the 6 mm convex shape near an internal corner clamp. 62

7.6 Erroneous transducer output. 63

7.7 Clipped transducer signal with a hypothetical unclipped signal. 64

7.8 Different shock wave peak locations for varying power intensities 2.5 GW/cm^2 to 17 GW/cm^2. 65

7.9 Experimental set up of the edge test. 67

7.10 Life time of a cavitation bubble produced by a 13 GW/cm^2 laser pulse in Deionised (DI) water. 69

7.11 13 GW/cm^2 bubble in tap water. 70

7.12 Bubble size for a 13 GW/cm^2 laser pulse in DI and tap water. 70

7.13 13 GW/cm^2 bubble in tap water with 40 mm tube surrounding the beam. . . 71

7.14 Suspected expansion wave upon bubble collapse. 13 GW/cm^2 laser pulse. . . . 71

7.15 Laser irradiation in deionised water 19 GW/cm^2 and 1.9 GW/cm^2. 72

7.16 Laser irradiation in tap water Top: 12 GW/cm^2 and 4.0 GW/cm^2. Bottom: beam off a plate edge 0.047 ms after pulse at 8.3 GW/cm^2. 72

7.17 Water breakdown at 13 GW/cm^2 0.047 ms after laser irradiation. 73

7.18 Line graph showing bubble lifetime per shot number for various energy levels in stagnant DI water at 1 Hz. 75

7.19 Bar graph showing percentage difference in bubble lifetime between the first shot and the average of all subsequent shots at laser energies at 1 Hz. 75

7.20 Bar graph showing difference in bubble lifetime between the first shot and the average of all subsequent shots for varying repetition rates. 76

7.21 Experimental set up of the edge test. 78

7.22 Average bubble life time and water conductivity over the long duration test, error bars represent the measurement uncertainty for an average of 20 pulses. 79

7.23 Experimental set up of the stagnant tap water tests. 81

7.24 Each point represents the average bubble lifetime of at least six shots with measurement uncertainty bars for stagnant tap water conditions. No Tube check is plotted for comparison with the following section. 82

7.25 The average bubble energy of at least six shots per point for stagnant tap water conditions. Error bars denote the uncertainty associated with each average. . 83

7.26 Experimental set up of the stagnant tap water tests within a tube. 84

7.27 Stagnant tap water tests, each point showing an average and measurement uncertainty bars of 10 single shots. 85

7.28 Experimental set up of the flowing tap water tests. 85

7.29 Raw data scatter plot of the bubble times in blue and first shock magnitudes in red. Each laser pulse is fired at 1 Hz. 87

7.30 Flowing tap water tests at two repetition rates and the previous stagnant water test. Each point showing an average of 10 shots at 0.05 Hz and 29 shots at 1 Hz plot along with their measurement uncertainty bars. 87

7.31 Experimental set up of the flowing tap water tests on a large flat plate target. 88

7.32 Summary of various tests done with water flowing along the beam path. . . . 89

7.33 An example of a process control chart showing the variability and limits. . . . 90

7.34 Control boundaries based on the fitted curve in Figure 7.32. 91

7.35 Analytical points of saturation for different tests. 91

7.36 Experimental set up of the flowing tap water tests on a large flat plate target. 93

7.37 Collection of first frames from the edge tests, each being 0.047 ms after a 8.3 GW/cm^2 laser pulse. The green dot shows the relative position of the 1 mm laser spot to the edge of the plate. 94

7.38 High speed imagery of edge tests at varying distances (0 mm - 20 mm) from the edge. Maximum bubble radius along beam path was 7.06 mm. All tests at 8.3 GW/cm^2. 95

7.39 Bubble lifetime at varying distances from the edge of a plate. Each point shows an average of three bubbles and each error bar represents the measurement uncertainty. 97

7.40 Experimental set up of the flowing tap water tests on varying chromium steel target geometries. 100

7.41 Various curvature shapes tested. 100

7.42 Convex radii were assigned positive values, concave radii were assigned negative values. Flat targets had no curvature, or zero radii. 100

7.43 Plot showing average bubble lifetime (of at least 9 points) of concave geometry plotted against target radius at 1 Hz at 8.3 GW/cm^2, with flowing water at 2.23 m/s. 101

7.44 Plot showing average bubble lifetime (of at least 3 points) of convex geometry plotted against target radius at 1 Hz at 8.3 GW/cm^2, in stagnant and flowing water at 2.23 m/s. 102

7.45 Plot showing average bubble lifetime (of at least 3 points) of flat geometry irradiated at 1 Hz, 8.3 GW/cm^2, in stagnant and flowing water at 2.23 m/s. 102

7.46 Average of at least 10 bubble lifetime points plotted against target radius with 8.3 GW/cm^2 laser pulses at 1 Hz and 10 Hz, in stagnant and flowing water at 2.23 m/s. 103

7.47 Average of at least 10 Laser Energy points plotted against target radius at 1 Hz and 10 Hz. Points were slightly displaced horizontally for clarity. 103

7.48 Summary of high speed images for flat, concave and convex geometry changes. 105

7.49 Progression of bubble collapse from maximum radius for flat target near corner (Row B in image above). Produced by laser pulse at 8.3 GW/cm^2, in stagnant tap water. 107

7.50 Cavitation bubbles in flowing water at 2.23 m/s at an average power intensity of 8.3 GW/cm^2. 108

A.1 This study produced bubble lifetimes not larger than 1.6 ms. 133

A.2 The behaviour of bubble energy uncertainty with tiny bubbles. 133

A.3 GCODE raster scanning pattern. 136

List of Tables

2.1 Examples of prior technology patents for monitoring laser shock peening. . . . 18

4.1 Specifications for Saga HP laser published by Thales [63]. 25

4.2 Properties of Almen strips made of AISI 1070 carbon steel, Grade 304 stainless steel and Din No 1.4939 12CrNiMo martensitic steel [66]. 26

4.3 Table of NI9775 analogue input card characteristics. 30

4.4 Table of 113B21 pressure transducer performance characteristics [69]. 31

5.1 Measured input and output instruments. 39

5.2 Assumed values of constant inputs and outputs. 39

5.3 High speed camera settings used. 40

5.4 Summary of experimental flow. 44

6.1 Design uncertainties of the pressure and laser energy measurements. 51

6.2 Each individual uncertainty u_i for perturbation of the bubble energy. 53

6.3 Calibration values for the energy meter output. 57

7.1 Stagnant DI water test conditions. 67

7.2 Repetition rate test parameters. 74

7.3 Paramaters for the duration test. 78

7.4 Stagnant tap water test parameters. 81

7.5 Initial tube test parameters 84

7.6 Flowing water test conditions. 86

7.7 Details of multiple tests done in water flow and increasing power intensity. . . 88

7.8 Edge test parameters. 93

7.9 Geometery test parameters. 99

A.1 Specification of data acquisition 127

A.2 Energy meter specifications 128

A.3 Specification of pyroelectric sensor 128

A.4 Specification of pressure transducer 129

A.5 Each individual uncertainty u_i. 132

A.6 Example using the sequential perturbation technique to obtain the uncertainty at a single operating point. 132

List of Symbols

The units of quantities defined by a symbol are indicated in square brackets following the description of the symbol. Quantities with no indicated units may be assumed to be dimensionless.

A_1	area of tube exit [mm^2]
A_2	area of nozzle exit [mm^2]
A_s	the irradiated spot area on the target [cm^2]
E_b	hemispherical bubble energy [J]
E_{laser}	energy output of the laser [J]
E_{scale}	energy scale of the energy meter [J]
PI	the power intensity of a laser pulse [GW/cm^2]
P_v	vapour pressure of the water being 2330 [Pa]
P_0	static pressure of the water taken as 87000 [Pa]
U_0	interpolation error
U_c	instrument error
U_d	design stage uncertainty
V_{out}	voltage output of the energy meter [V]
V_{scale}	output voltage range of the energy meter [V]
$\dot{V}$	volumetric flow rate of water 175×10^3 [mm$^3/s$]
ρ	density of the water which is 998.2 [kg/m^3]
τ	the pulse width of the laser [ns]
τ_b	first bubble oscillation period [s]
ξ	curved boundary parameter
d	spot diameter [mm]
v_1	water exit velocity from the tube [m/s]
v_2	water exit velocity from the nozzle [m/s]
T_{c_1}	time taken for a cavitation bubble to collapse from its largest radius [s]

List of Acronyms

3D	Three Dimensional
AE	Acoustic Emission
BSP	British Standard Pipe
CL	Control Line
cRIO	Compact Reconfigurable Input/Output
CSIR	Council for Scientific and Industrial Research
DAQ	Data Acquisition Device
DI	Deionised
ICP	Integrated Circuit Piezoelectric
LCL	Lower Control Limit
LSP	Laser Shock Peening
Nd:YAG	Neodymium doped Yttrium Aluminium Garnet
NDE	Non Destructive Evaluation
NLC	National Laser Centre
OD	Optical Density
PPE	Personal Protection Equipment
PVC	Polyvinyl Chloride
PVDF	Poylyvinylidene Difluoride
SOP	Standard Operating Procedure
SP	Shot Peening
TDMS	Technical Data Management Streaming file format
UCL	Upper Control Limit
VI	Virtual Instrument

1 Introduction

Since the first observation of fatigue in the conveyor chains within the mines of Oberharz, and the subsequent catastrophic and frequent failures of rail road carriages in the nineteenth century, mechanical engineers have long have sought to reduce failing metal components [1].

Many post manufacturing techniques have been developed and implemented to increase the fatigue life of components. Since the vast majority of fatigue cracks start on the surface of metal parts, surface techniques are most practical when lengthening fatigue life. The most effective are those that induce compressive residual stresses within the surface of the susceptible metal part. These residual stresses serve to counteract tensile stresses that would otherwise open up microscopic flaws (which propagate into larger cracks) on the surface, making the component last longer in service. A particularly effective technique for inducing compressive residual stress is a specialised process called Laser Shock Peening (LSP).

LSP makes use of a high power pulsed laser to treat the surface of materials [2]. Similar to conventional Shot Peening (SP) - which is a standardised practise of impacting metal components with hard spherical balls at high velocities - LSP aims to induce compressive residual stresses in metal components, but with a greater degree of consistency and control, to stress magnitudes and depths greater than that of SP [3].

Amongst other metal improvements, LSP effectively enhances the fatigue life and resistance to stress corrosion cracking in metal components such as the core shroud of nuclear reactors [4] or treating turbine blades to increase low-cycle fatigue resistance [5].

1.1 Laser Shock Peening in South Africa

The South African LSP (SA-LSP) group was officially formulated in 2012 within a framework between Airbus (Germany), the South African National Aerospace Centre, the University of the Witwatersrand, and the National Laser Centre (NLC) at the Council for Scientific and Industrial Research (CSIR) with the support of the Department of Science and Innovation - National Research Fund, Centre of Excellence in Strong Matrials (DSI-NRF COE-SM). Numerous numerical evaluations of LSP were performed by Airbus in the European aerospace sector at the time.
The South African partnership sought to compliment this with the experimental development

of the process. The SA-LSP work-cell began with a number of fundamental investigations into aspects not well documented in the literature, such as the details for effective inertial confinement, typically water.

Under certain circumstances, the occurrence of the cavitation event was revealed in the water layer using high speed Schlieren photography [6]. It appeared that the bubble size and collapse time correlated well to the laser pulse energy delivered to the target and a fundamental evaluation of the cavitation bubble oscillation period as a process diagnostic was conducted [7]. The SA-LSP group continues to conduct research and development into a number of LSP applications such as aerospace [8, 9, 10], power generation [11, 12], and a number of key aspects related to the process.

1.2 Cavitation Bubble as a Process Diagnostic

Often, safety-critical high value components (turbine blades, aircraft structures [12, 8, 13]) are treated with LSP. This has the implication that the process and performance of the LSP system needs to adhere to the safety and reliability standards of these industries. Diagnostics and in-process monitoring are important when controlling a LSP process and ensuring that the correct residual stresses are generated in the surface of the treated part. In addition to this, as the process of LSP relies on the quality of the laser beam which can deteriorate or be blocked, diagnostics ensure that failures are recorded and rapidly resolved.

When sufficient water covers the target surface during LSP, the shock event initiates a cavity (see Figure 1.1) that grows to a maximum size and collapses with a second shock wave. This cavity is known as a cavitation bubble and the longest period of growth and collapse is known as the first bubble oscillation period.

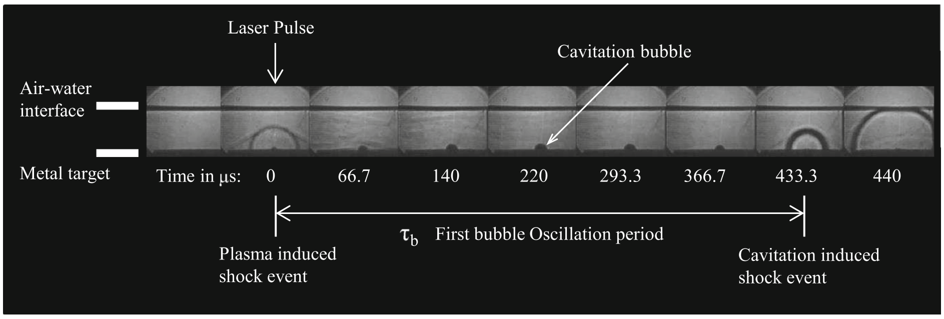

Figure 1.1: The lifetime of a laser induced cavitation bubble [7].

Recently, the SA-LSP group found that the first cavitation bubble oscillation period generated in LSP could be correlated to the energy of the laser pulse [7]. This time measurement (between pulses, indicated as '86', in Figure 1.2) is easily done since the formation and collapse creates two prominent pressure signals. The period between pulses relies on the temporal location of the peaks rather than their magnitude, making this measurement insensitive to the precise location of pressure transducers.

Once the life time and corresponding bubble size is known, the energy of the first cavitation bubble can be calculated, potentially informing researchers of the localised laser energy deposition for peening - as close to the process as is viably possible [7]. The use of cavitation bubbles to verify the energy being delivered to the target was patented (Figure 1.2) by Dr D. Glaser (CSIR) and Prof. C. Polese (Wits), along with the method of creating a water layer to support cavitation [14]. This patent merited a research and development grant from the South African government Department of Science and Innovation by means of a Technology Innovation Agency Seed Fund allocation.

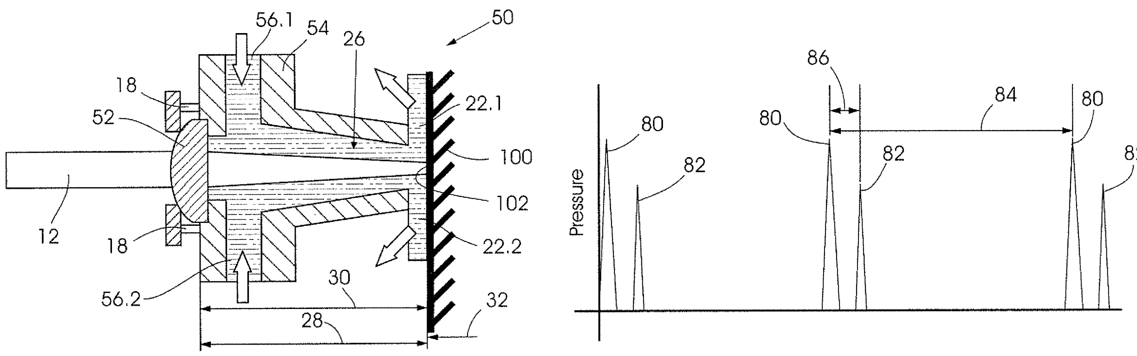

Figure 1.2: A prototype of the patent hardware and anticipated pressure pulses [14].

The studies prior to filing the aforementioned patent were performed in a static water tank with single laser shots. This deviates significantly from how the process would be applied industrially. Further insight and understanding of the limitations, attributes and successful operating conditions is therefore necessary if the diagnostic monitoring technique is to be further developed.
The context of this research is to develop a physical understanding of a cavitation bubble diagnostic for potential industrial implementation.

2 | Literature Survey

2.1 Laser Shock Peening

As described prior, Laser Shock Peening (LSP) is a surface treatment process that uses a laser to create shock waves that effectively induces compressive residual stresses within metal components, thereby enhancing their resistance to fatigue failure. This can have significant cost-saving benefits, particularly if the failure of the part in question is hugely expensive.
The first observations and studies in laser shock processing were done in the 1960s by Batelle Columbus Laboratories in the United States of America [15]. Subsequent research was undertaken by the Laboratoire pour l'Application des Lasers de Puissance (LALP) in France focussing on modelling mechanical effects, characterizing shock waves and industrial applications [3, 15]. Toshiba Corporation successfully applies LSP to prevent stress corrosion cracking on nuclear power plant core shrouds in Japan [4].

2.1.1 Residual Stress Treatment

LSP is one of numerous techniques of inducing compressive residual stresses in metals. Amongst others, effective techniques include shot peening, low plasticity burnishing, cavitation peening, ultrasonic impact treatment [16, 17, 18, 19].
Shot Peening (SP) is a long standing, well established compressive residual stress enhancement technique and profitable industry in which hard spherical balls are accelerated to high velocities with compressed air and impacted into metal parts. The impacts leave a plastically deformed surface resulting in a compressive residual stress. Compared to an untreated part, the resistance to cracking from fatigue is greatly improved when treated with SP.

Peyre et al. demonstrated the advantage of using both SP and LSP in Figure 2.1. The significant increase of fatigue strength (infinite life at a given cyclic load) after treatment with SP is further improved by LSP [2].

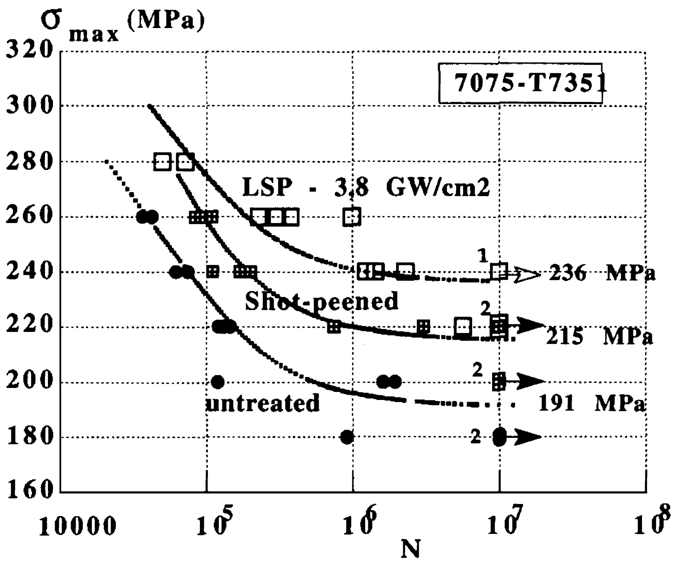

Figure 2.1: Fatigue life curves for untreated, shot peened and laser shock peened 7074 aluminium alloy [2].

2.1.2 Process Mechanism

The process of LSP (see Figure 2.2) begins by firing a laser to emit a nanosecond pulse of laser radiation. This beam is focused to a specific spot size on the work piece being treated. Energy is transferred to the surface of the material at a rapid rate, ablating (vaporising) part of that surface. As the laser pulse is absorbed, ionisation take place and the metal vapour quickly becomes a hot expanding plasma. The rapid expansion (or explosion) creates a very high pressure front (shock wave) which propagates both into the material and away from the surface, transferring kinetic energy as it travels [2].

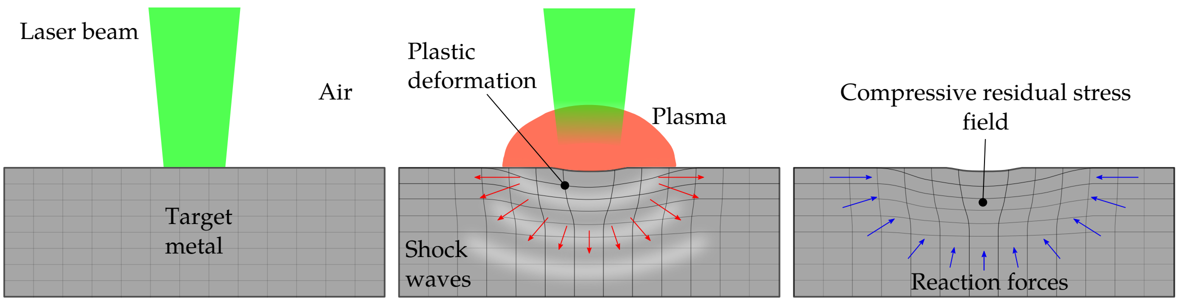

Figure 2.2: The process of LSP; shock waves create plastic deformation, inducing a compressive residual stress field on and below the surface.

The energy that is transferred by the shock wave passing through the surface of the material is sufficient to overcome the material's dynamic yield strength and that material undergoes local plastic deformation. Afterwards, this deformation is opposed by the surrounding unaltered material resulting in a compressive residual stress in the treated location [5]. In this way, the process of LSP relies on strong shock waves to create compressive residual stress.

The high strain rates ($10^6\,s^{-1}$) produced by LSP refines the metal grain structure (see Figure 2.3) thereby increasing the number of dislocations, which leads to increased microhardness. This refined grain structure improves crack arresting and hinders stress corrosion cracking [20]. An increase in hardness has also been linked to higher fatigue strength, tensile strength and wear resistance [21].

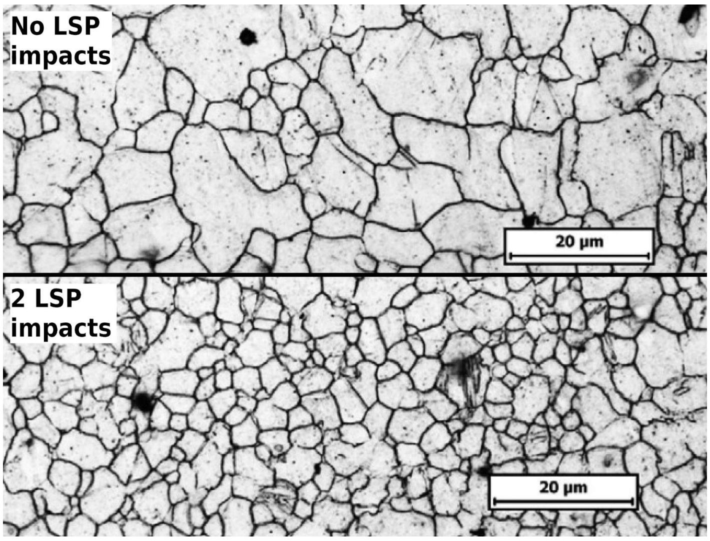

Figure 2.3: Micrograph cross section of AZ31B Mg alloy showing grain refinement after LSP impacts [20].

In LSP, the laser radiation on a target is dependent on the spot size, pulse duration and the energy of the beam. Combining these gives a measure called laser power intensity, given by Equation 2.1.

$$\begin{aligned} PI &= \frac{E_{laser}}{\tau \cdot A_s} \\ &= \frac{E_{laser}}{\tau \cdot \frac{\pi d^2}{4 \cdot 10^2}} \end{aligned} \tag{2.1}$$

where:
PI is the power intensity [W/cm^2]
E_{laser} is the laser energy [J]
τ is the pulse width of the laser [ns]
A_s is the irradiated spot area on the target [cm^2]
d is spot diameter in [mm].

Adhering to the convention within the field of LSP, the units of power intensity is not stated as [W/cm^2] but rather [GW/cm^2].

By increasing the magnitude of the laser power intensity (and correspondingly the pressure of the shock wave) the magnitude and depth of the residual stress will increase. Conversely, if the power intensity is reduced the residual stress within the metal is diminished. This is illustrated by the vertical shift of the lines in Figure 2.4.

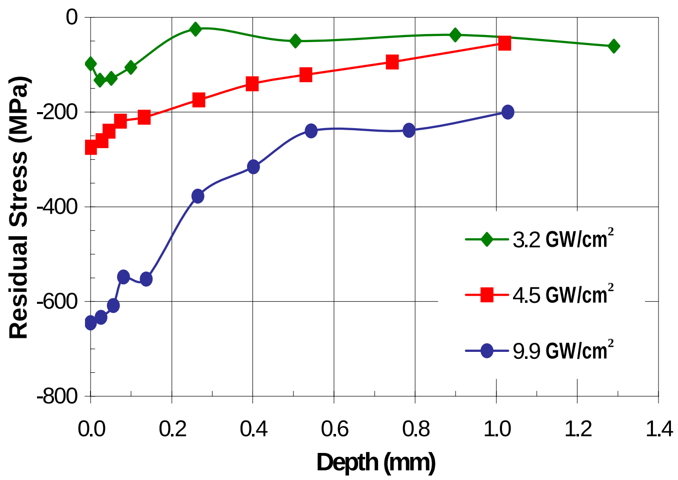

Figure 2.4: Residual stress profiles for LSP treated Ti-6Al-4V samples at different power intensities [22].

2.2 Confinement

While LSP has been performed on bare metal surfaces, the strength (pressure magnitude) of the shock wave and resulting depth of plastic deformation into the metal surface can both be increased if the laser driven shock event is contained using a laser-transparent tamping or confinement layer such as water, glass, acrylic and silicon rubber [3, 23, 24].

Water, as illustrated in Figure 2.5, is the preferred method of confinement in LSP as it is cheap, relatively transparent, is in wetted contact (very close) to the surface, is self renewing for multiple pulses and produces confinement pressures slightly lower than glass [3].

LSP has been used with a water confinement layer of varying thickness. A thin water layer is typically considered between 1 to 2 mm thick [25] but up to 5 mm thick water has been studied [23]. An industrial advantage to using a thin water layer is the low flow rate (for an equivalent wetted area) and greater flow control, making it cost effective when using high purity water.

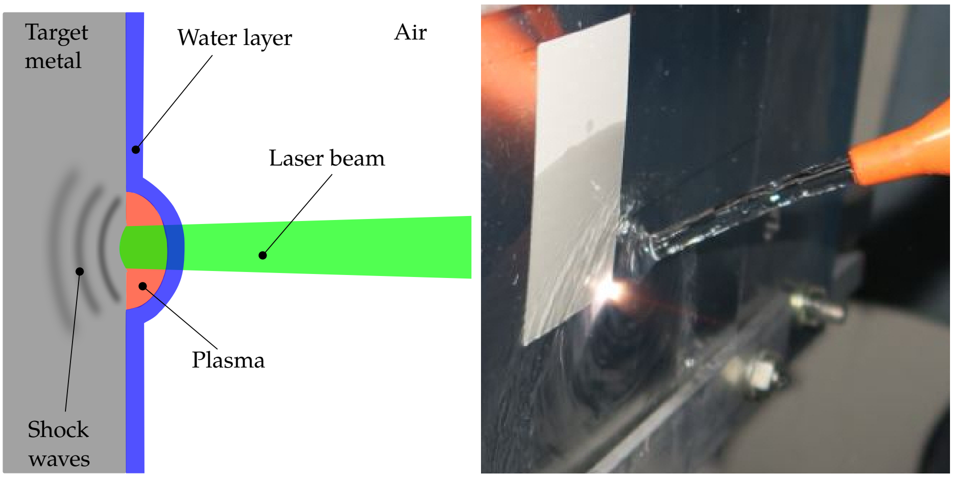

Figure 2.5: An illustration of thin water LSP alongside an image of the process.

Peening with thicker water layers ensures that the layer is effectively restored after the shock event with minimal directional control and allows the formation of laser induced cavitation bubbles, but allows for greater absorption of laser energy prior to arriving at the target.

The power intensity of the laser can be increased effectively up to a limit, as the laser energy is not effectively delivered after a certain magnitude. Beyond this point, an increase in the power intensity does not increase the peak pressure experienced by the metal and so limits the peak residual stress. This limit has been documented in several papers [26, 27, 5, 28]. The primary reason for this limit is the "breakdown plasma" that occurs in the confinement layer when the laser power intensity reaches a certain threshold.

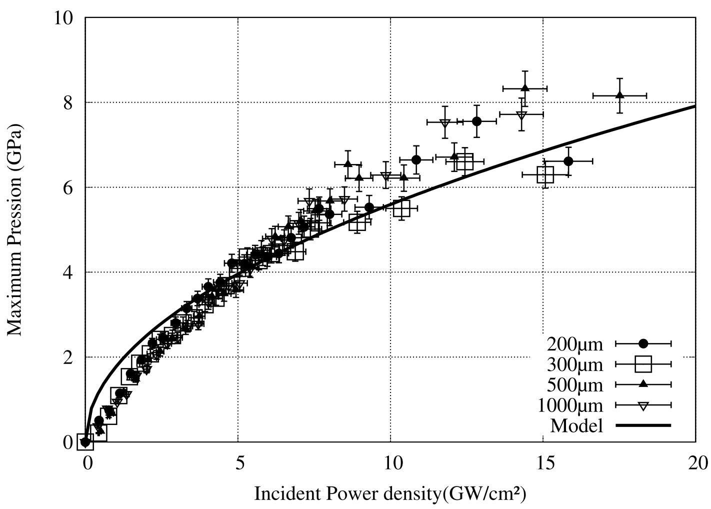

Figure 2.6: The variation of peak pressure with laser power intensity for different target thicknesses. The laser was at 532 nm [27].

Optical breakdown occurs when a critical free electron density of $10^{18}\,\text{cm}^{-3}$ to $10^{20}\,\text{cm}^{-3}$ is exceeded, typically near the focal point within a converging laser pulse. Two mechanisms lead to plasma formation; directly ionising the medium, which is called multiphoton ionisation, or via inverse Bremsstrahlung absorption, which is called cascade or avalanche ionisation and requires one or more free electrons at the beginning of the laser pulse [29].

Noack et al. made use of streak photography to determine laser induced shock pressures and their decay with distance. For 6 ns laser at 10 mJ, the shock wave was attenuated by two orders of magnitude over r = 65 μm. It was concluded that the smaller the plasma r_0 (or the further a measurement is taken r from the edge of the shock wave source, increasing the ratio r/r_0), the greater the decay of the shock wave pressure. Limiting laser repetition rate to avoid interaction with following laser pulses was also briefly mentioned [30].

The wavelength of the laser has an effect on the type of ionisation and the power intensity at which the peak pressure saturation occurs. At laser wavelengths of 1064 nm, avalanche ionisation is dominant in the breakdown process and at shorter wavelengths multiphoton ionisation dominates. This ionisation, which results in a flattening or saturation of delivered laser energy, is shown to occur at different power intensities.

The greater dispersion of all points in Figure 2.6 (increased stochastic or random breakdown and absorption) occurs at around 7 GW/cm^2. In Figure 2.7, the 532 nm points also flatten nearer to 6 GW/cm^2 compared to 1064 nm wavelengths that saturate later, near 10 GW/cm^2 [31, 27]. It is not beneficial for this reason, that LSP with laser pulse lengths of a few ns at 532 nm, be implemented at power intensities above 6 - 7 GW/cm^2.

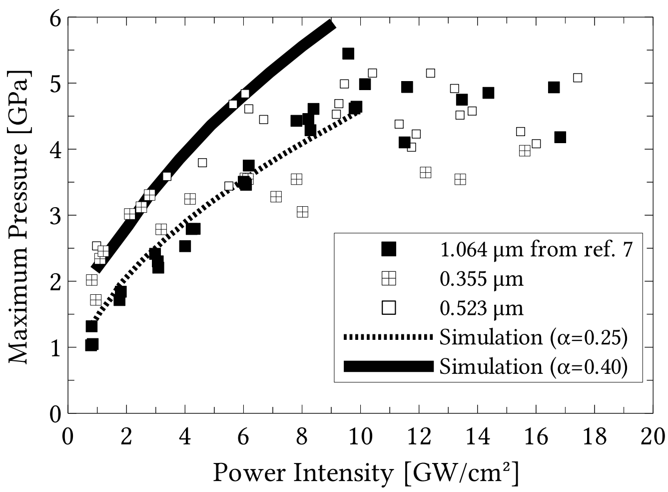

Figure 2.7: The variation of peak pressure with laser intensity for different laser wavelengths after [31].

2.3 Cavitation

Hydrodynamic Cavitation

Cavitation bubbles occur within high flow environments such as in valve constrictions and on impeller blade surfaces within pumps or marine vessels (such as the hydrofoil in Figure 2.8) [32]. This will occur in an area where the fluid flow is sped up to a sufficient speed that the local static pressure drops to below the vapour pressure of the fluid [33]. This leads to a bubble of vapour forming creating a void within the liquid. This void is called a cavitation bubble. As the bubble travels (due to a pressure gradient typically driving the flow) to an area of higher localised pressure, the void is no longer sustained and collapses.

Figure 2.8: Vortex cavitation on a hydrofoil tip, an example of hydrodynamic cavitation [34].

Due to the inertia given to the water rushing towards the centre of the bubble, the collapse is violent and displays powerful fluid dynamics. These include shock wave emission and high speed liquid jets that can both cause severe erosion of the surface over time [32].

Laser Induced Cavitation

A laser induced physical disturbance can provide sufficient kinetic energy for cavitation, by energising molecules with high intensity laser, either in the water or on a target. This target matter rapidly turns to vapour which is then ionised by the beam photons, thus creating extremely hot, rapidly expanding plasma. This plasma produces a very sharp (almost vertical) rise in pressure and the discontinuity is manifested in the form of a shock wave in the fluid, seen in the frames of Figure 2.9.

The high temperatures (60 K to 15000 K) of the plasma inevitably vapourises surrounding liquid water, creating a vapour bubble that grows outward.

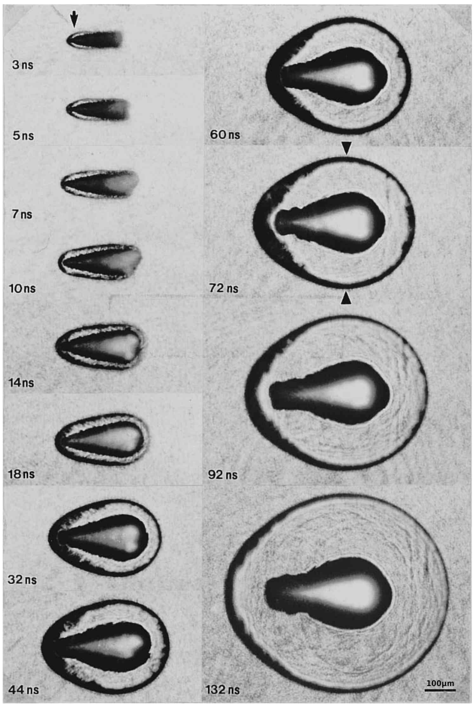

Figure 2.9: Laser induced plasma in open water, creating a shock wave (outer ring) that surrounds a growing cavitation bubble (tear drop shaped cavity) [35].

This bubble will grow to a maximum size until the conditions supporting the cavity are no longer present. As the hot plasma cools and water vapour inside the bubble condenses on the walls, the bubble collapses. The shape of the collapse is heavily dependent on static forces and surrounding geometry in the water.

2.4 Cavitation in LSP

Figure 2.10 shows that if the confinement layer conditions are correct, the laser induced burst of plasma on the target surface is not only sufficient to produce shock waves within the metal below but will also initialise a cavitation bubble which grows and collapses.

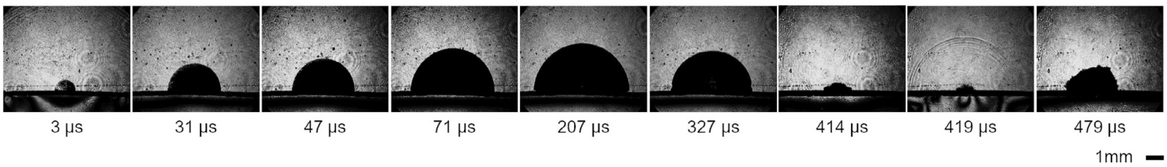

Figure 2.10: Laser induced cavitation growth and collapse under 5 mm of water [36].

In LSP, a water layer thickness of 5 mm or more will be required to allow the growth and collapse of cavitation bubbles at laser power intensities higher than 2.5 GW/cm^2 [6]. The higher the laser energy input, the thicker the water layer that is needed to contain a larger cavitation bubble.

Upon collapse, a second shock wave is emitted from the site of collapse [37, 36]. Since the bubble is initialised on the surface of the metal part, it takes the form of a hemisphere and then rapidly collapses on itself in a toroid shape, often producing a high speed water jet. This is illustrated in Figure 2.11.

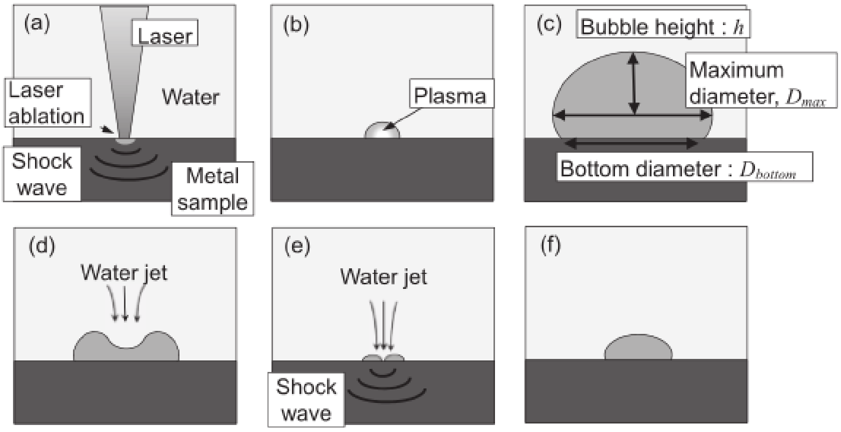

Figure 2.11: The formation of a laser induced cavitation bubble [37].

With ultra short laser pulses, it is often difficult to observe breakdown plasma. In these instances, the detection of cavitation bubbles is a suitable indicator for laser induced breakdown [38].

For applications in thick water LSP, the wavelength of the laser should be that which is least likely to be absorbed by the water layer (infrared) but not also likely to cause breakdown at the surface (ultraviolet). A convenient compromise is to use the second harmonic of Neodymium doped Yttrium Aluminium Garnet (Nd:YAG) lasers, at a wavelength of 532 nm, which is visible green light [5].

2.4.1 Cavitaton Bubbles near Geometry

The lifetime of a hemispherical cavitation bubble in contact with a solid boundary is increased when compared to a perfectly spherical cavitation bubble away from any boundary. Godwin et al. postulates two reasons for this delay in collapse time [39]. The first is likely due to the toroidal flow that hinders surrounding water that is drawn toward the centre of the bubble cavity during collapse. The second is the presence of the wall that also inhibits fluid flow toward the bubble centre [39]. It can be seen from Figure 2.12a, that a hemispherical bubble

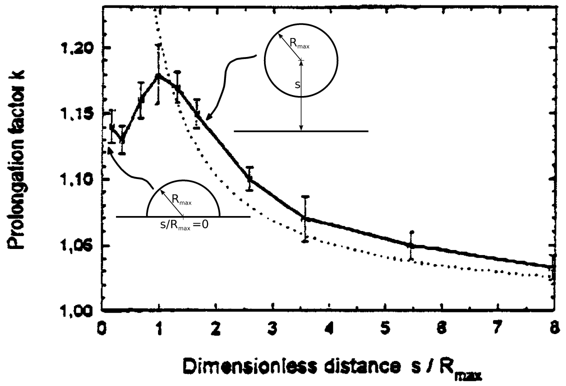

(a) Prolongation factor versus the normalized stand off distance from a wall [39].

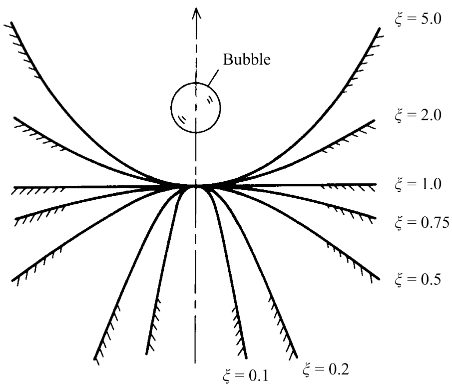

(b) Curved boundary parameter ξ used by Tomita et al. [40].

Figure 2.12: The bubble lifetime is extended near flat and concave boundaries.

on the wall (s/$R_{max} = 0$) will have a lifetime approximately **1.146** times longer than that of an isolated spherical bubble with the same energy.

Tomita et al. conducted several simulations and experiments to understand the motion of cavitation bubbles and jet formation near curved rigid boundaries [40]. Figure 2.12b shows the curvature defined by a parameter ξ whereby concavity was shown as $\xi > 1$, a flat surface $\xi = 1$ and convexity $\xi < 1$. Importantly, the time between growth and collapse was found to be lengthened with a concave surface and shortened with a convex surface [40].

2.5 LSP Cavitation Diagnostic

Not all the laser energy arrives at the surface being treated in an LSP process. When high powered lasers are used, some energy is absorbed in the premature ionisation and dielectric breakdown of the water (and sometimes air) between the laser and sample being treated [7]. The extent to which this happens outside of control (due to dissolved ions in water [41], random dust particles and airborne water droplets in air) is a fluctuation that is difficult to describe empirically. Since any breakdown will produce a highly absorbent plasma, the local energy that reaches the sample surface is not known with certainty.

In addition, most (if not all) laser monitoring can only take place before the final focussing optic, as shown in Figure 2.13. This means that if a disturbance of the beam delivery (such as premature plasma breakdown, blockage or broken optic) occurs after the energy meter, it will not be recorded or quantified until post process analysis of the sample has been completed.

In addition, the greatest beam variance and energy loss in a LSP system occurs at narrow beam diameters, nearest to the target.

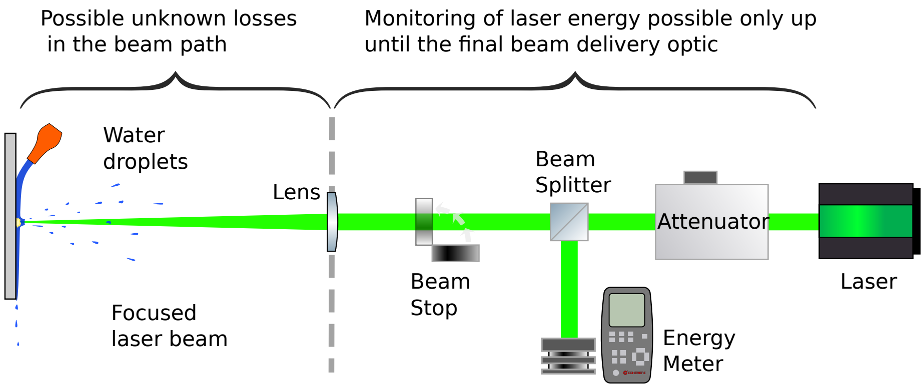

Figure 2.13: Water spray typically contaminates the beam path, limiting beam measurements to before the final window/lens.

Hydrophone Measurement

In water, the high pressure shock wave (mentioned in Section 2.1.2) travels rapidly outward (both in the metal and outside) from the site of the LSP process. If the water confinement layer permits, the shock wave can be recorded with a high speed (short rise time) pressure transducer known as a hydrophone. The waveform output from a needle hydrophone of a laser induced (though not peening) cavitation event is shown in Figure 2.14.

This signal allows the pressure dynamics of the cavitation event to be understood graphically. Firstly, the prominence of the pressure spikes should be noted. The peak pressures of the laser-induced and first collapse shock waves make them easily distinguishable from the compression and expansion dynamics of the fluid displaced by the bubble and subsequent shock reflections. The time between these peaks is called the first bubble oscillation period or more colloquially, bubble lifetime. Subsequent collapses are difficult to distinguish from the surrounding fluid dynamics.
Due to pressures of over 200 kbar from the laser-driven breakdown of metal to plasma, the first shock wave in Figure 2.14, is seen as almost vertical spike in pressure [42]. The second shock event or first bubble collapse, shows a similar steep rise on the hydrophone signal. It, however, is not as steep and has both a wider peak and longer preceding slope.

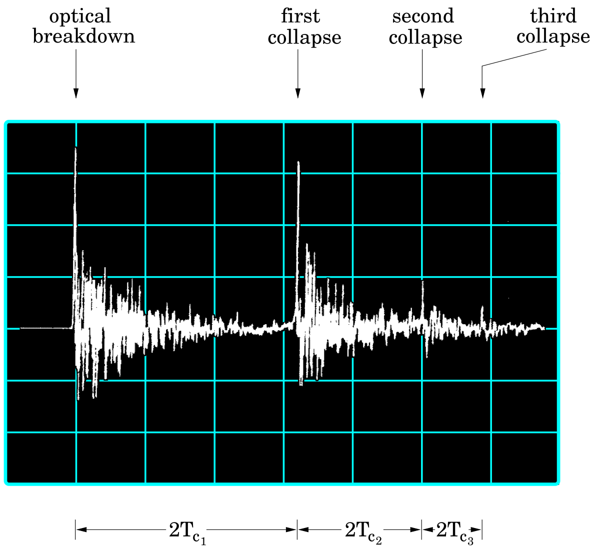

Figure 2.14: Signal from hydrophone of the laser breakdown and cavitation bubble collapse [41]. 2T$_{c_1}$ is the whole bubble lifetime. The largest bubble radius occurs at T$_{c_1}$ after initial spike.

The pressure information from a Poylyvinylidene Difluoride (PVDF) transducer in Figure 2.15 illustrates this well. Here the lower, slower pressure rise preceding the peak in the bubble collapse waveform can be seen [43].

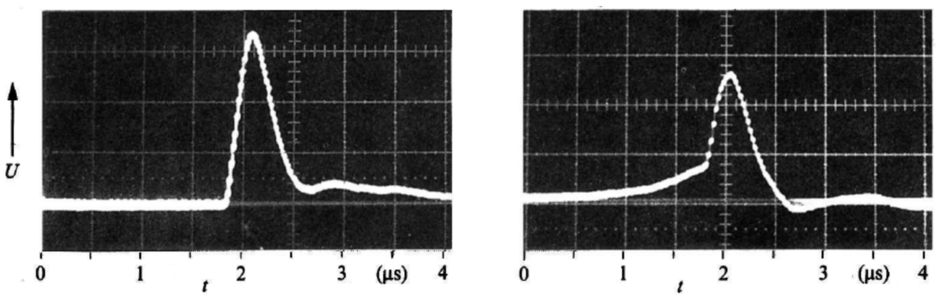

Figure 2.15: Signals from a PVDF transducer immediately after the laser induced plasma and at the bubble collapse [43].

2.5.1 Cavitation Energy

The energy required to create an isolated, spherical cavitation bubble E_B is derived from the energy or work needed to expand a volume ΔV against a restoring pressure derived force F;

$$E = F \cdot \Delta x, \qquad F = \Delta P \cdot A, \qquad \Delta V = A \cdot \Delta x$$

$$\therefore E = \Delta P \cdot \Delta V$$

For an infinitesimally small volume dV and pressure difference ΔP:

$$dE = \Delta P \cdot dV$$

The pressure across the boundary of a bubble is the difference between the static pressure P_0 and the vapour pressure P_v.

Integrating over the volume as well as substituting the pressure difference across the boundary of the bubble as a constant ($\Delta P = P_0 - P_v$):

$$E_B = \int_0^{V_{max}} (P_0 - P_v) dV$$

From the volume of a sphere $V = \frac{4}{3}\pi r^3$ with radius r:

$$dV = 4\pi r^2 dr$$

$$\therefore E_B = \int_0^{R_{max}} (P_0 - P_v) 4\pi r^2 dr$$

For a hemispherical bubble, the volume is halved, giving:

$$E_b = \int_0^{R_{max}} (P_0 - P_v) 2\pi r^2 dr$$

$$E_b = \frac{2\pi}{3}(P_0 - P_v) R_{max}^3 \tag{2.2}$$

The collapse time from maximum bubble radius to zero radius, τ_c, for a spherical bubble was found by Rayleigh [35]:

$$\tau_c = 0.915 R_{max} \sqrt{\frac{\rho}{(P_0 - P_v)}} \tag{2.3}$$

As Figure 2.14 illustrates, the theoretical time interval between the initialisation and the collapse pulses τ_{th}, which is also called the first bubble oscillation period for a bubble in open water, is assumed as twice the collapse time [35]:

$$\tau_{th} = 1.83 R_{max} \sqrt{\frac{\rho}{(P_0 - P_v)}} \tag{2.4}$$

As literature suggests, a prolongation factor, $k = 1.146$, may be included to account for longer actual bubble lifetimes when on a rigid wall:

$$\tau_b = \frac{\tau_{th}}{k} \tag{2.5}$$

Rearranging for R_{max} and substituting Equation 2.4 into Equation 2.2, the cavitation bubble E_b is given as [7]:

$$E_b = \frac{(P_0 - P_v)^{\frac{5}{2}}}{\left(1.43031\rho^{\frac{1}{2}}\right)^3}\,\tau_b^3 \tag{2.6}$$

where:

E_b = hemispherical bubble energy [J]

P_0 = static pressure of the water taken as 87000 [Pa]

P_v = vapour pressure of the water being 2330 [Pa]

ρ = density of the water which is 998.2 [kg/m^3]

τ_b = first bubble oscillation period [s]

When constants are simplified to become a coefficient, the relationship between bubble energy and first bubble oscillation period is a cubed one:

$$E_b = Constant \cdot \tau_b^3 \tag{2.7}$$

Vogal et al. determined a complete energy balance for breakdown produced by nano and femtoseond lasers in water. Figure 2.16 describes some of their findings with small bubbles, notably, that the conversion of laser energy (E_{in}) to bubble energy (E_B) is around 30% efficient [44]. While this conversion is unlikely to remain constant with larger bubbles (from the change in E_B percentage between 1 mJ an 10 mJ), this demonstrates the principle that a relationship between laser energy and bubble energy exists.

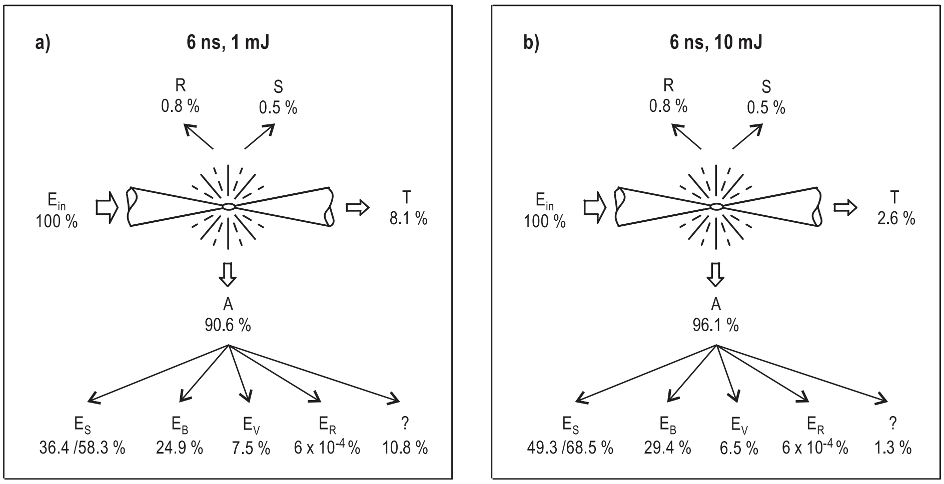

Figure 2.16: Energy balance of laser induced breakdown in water [44].

By determining cavitation bubble energy in thick water layers and correlating it to the laser input energy, the peening process can be monitored [7]. This is the manner in which the first bubble oscillation period may serve as a diagnostic (mentioned in Section 1) in the LSP process.

2.6 Other Diagnostics

The need to better understand the LSP process in an industrial setting has motivated numerous researchers to create different LSP diagnostic techniques that attempt to monitor the process after the final beam delivery optic.

Prior patented methods of LSP monitoring can be categorised as measuring post-processing or interrupted-processing test coupons, optical changes, acoustic emissions and plasma spectra. These are summarised in Table 2.1 and Figure 2.17.

Table 2.1: Examples of prior technology patents for monitoring laser shock peening.

Patent No.	Title	Year	Owner
	Post Processing Methods		
US5948293	Laser Shock Peening Quality Assurance by Volumetric Analysis of LSP Dimple	1999 [45]	General Electric Company
US5951790	Method for Monitoring and Controlling LSP using in plane deflection test coupon	1999 [46]	General Electric Company
US6094260	Holographic Interferometry for monitoring and controlling LSP	2000 [47]	General Electric Company
	Acoustic Methods		
US6512584B1	Quality Control For Laser Peening	2003 [48]	LSP Technologies Inc.
US6629464B2	LSP Quality assurance by acoustic analysis	2003 [49]	Suh et al.
US6914215B2	Real Time LSP Quality Assurance by Natural Frequency Analysis	2005 [50]	General Electric Company
US7816622B2	System and method for controlling LSP	2010 [51]	General Electric Company
US8520470B2	LSP measurement system and method	2013 [52]	General Electric Company
	Plasma Methods		
US6075593	Method for monitoring and controlling laser shock peening using temporal light spectrum analysis	2000 [53]	General Electric Company
US6254703B1	Quality Control Plasma Monitor for LSP	2001 [54]	LSP Technologies Inc.
US6554921B2	Quality Control Plasma Monitor for LSP	2003 [55]	LSP Technologies Inc.
US7273998B2	System and Method for Monitoring LSP	2007 [56]	General Electric Company
	Beam Methods		
US8810792B2	Polarization Compensated Beam Splitter and Diagnostic System for High Power laser Systems	2014 [57]	Metal Improvement Company
US7148448B2	Monitored Laser Shock Peening	2006 [58]	General Electric Company
	Other Methods		
US7906746B2	LSP System with time of flight monitoring	2011 [59]	General Electric Company

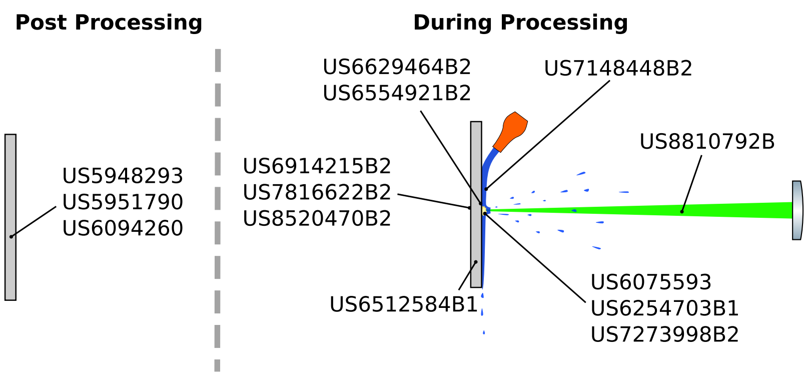

Figure 2.17: Prior innovations in LSP monitoring, at different points in the LSP process.

The post processing measurements of coupons that have been treated with LSP cover the greatest number of studies, providing deep understanding about the process. These include residual stress measurements, hardness, roughness and geometry tests, fatigue life tests and corrosion tests [2, 20]. The optical methods do not assess the efficacy of the process so much as monitor the known correct conditions (beam energy, shape, pulse width, water layer presence) for LSP.
Acoustic monitoring within the metal rely on a coupling between the part being monitored and the sensor that receives the acoustic emissions. Acoustic emission in air or water are also monitored, but this relies on the fixed distance between the transducer and the shock source. Plasma light emissions are used to determine the composition of the elements, ensuring that the process consistently vaporises the same constituents of both metal and water.

2.6.1 Acoustic Emission Measurement

Suh et al. have registered a patent that makes use of the acoustic emissions both within the work piece and in the air as a method of real time Non Destructive Evaluation (NDE), shown in Figure 2.18 [49]. Within the patent, two methods of acoustic signal monitoring are disclosed: through a workpiece mounted transducer and with a microphone in the air nearby. The signal acquired from these two instruments can be used (with the aid of a computer capturing the signals) to calculate acoustic energy parameters of the plasma, the maximum amplitude and the integral of the signal over time (area under the curve). This ensures that there are at least four values that can be correlated to a pass or fail criterion for every laser pulse [49].

Enoki et al. performed experiments with aluminium submerged underwater. The broadband acoustic emission within the sample was detected with an Acoustic Emission (AE) sensor attached to the rear surface of the sample, opposite the area irradiated with the laser pulse. This AE emission was sampled at 10 MHz with a continuous wave memory (CWM) system previously developed by the same research group. The waveform (shown in Figure 2.19a) clearly shows the cavitation collapse with almost the same amplitude as the laser shock event. The interval time between these events are shown (Figure 2.19b) plotted against the laser spot power density. The authors state that for power densities greater than 10 GW/cm^2 there is no substantial change in either interval time or simulated pressure. This saturation is attributed to the parasitic plasma breakdown that occurred in the water before the target [28].

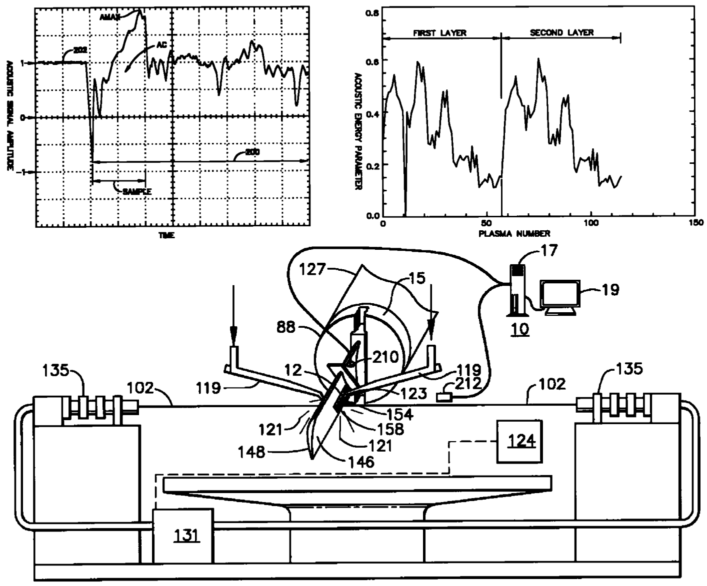

Figure 2.18: Non destructive evaluation patent. Adapted from [60].

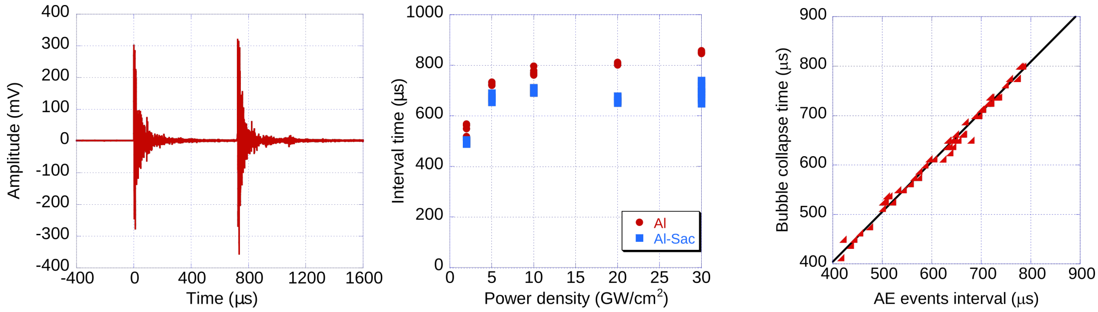

(a) AE waveform on rear surface.

(b) Shock interval versus power density.

(c) Bubble collapse time versus AE event interval.

Figure 2.19: Experimental results of a submerged sample from Enoki et al. [28].

There is a good linear correlation between AE-measured interval time and high speed image bubble collapse time, shown in Figure 2.19c, making the interval time a good metric for cavitation bubble lifetime in reality.

Takata et al. made use of deconvolution technique to determine the forces and pressures of cavitation bubbles collapsing with AE sensors submerged in water. It was stated that the magnitude of the sensor output alone was not sufficient to characterise the shock wave because it was dependent on the distance from the shock peening event, which will change if the laser moves relative to these sensors [61]. It was also noted, however, that attaching an AE sensor on the sample is not viable for process monitoring due to the use of one sensor per workpiece. Takata et al. show that the generated waveform of an AE sensor submerged in the water tamping layer is in good agreement with the waveform of a sensor physically attached to the workpiece [61] .

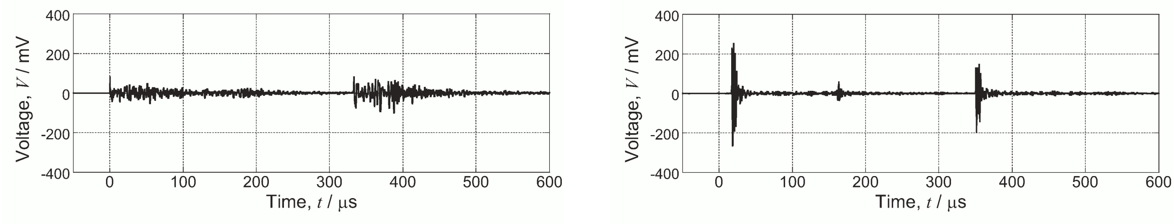

(a) AE waveform from sensor on the surface of the sample.

(b) AE waveform from sensor in the water confinement layer.

Figure 2.20: Detected AE waveforms during laser shock peening. [61].

A water based sensor allows for greater location flexibility, detection of laser induced breakdown (see the small second peak at 160 μs in Figure 2.20b) and easier installation than that of an adhered sensor.

2.6.2 Plasma Emission Spectrum

The use of plasma emission spectra for monitoring LSP in real time was studied by Benicewicz et al. [13]. As the plasma (consisting of excited molecular and atomic elements) cools, it emits light due to the de-excitation of the plasma constituents. The elemental composition of the vaporised material may be accurately determined through spectral analysis of light emitted from the plasma. To simplify the process, the magnitude of an emission frequency of interest (in this case 455 nm) can be detected through the use of a narrow bandpass filter in conjunction with a gated photomultiplier tube (PMT). This is done at multiple laser energy levels, shown in Figure 2.21. The laser used in this study had a relatively high energy; 2-20 J with a 20 ns pulse duration. One successful application was the detection of water breakdown [13].

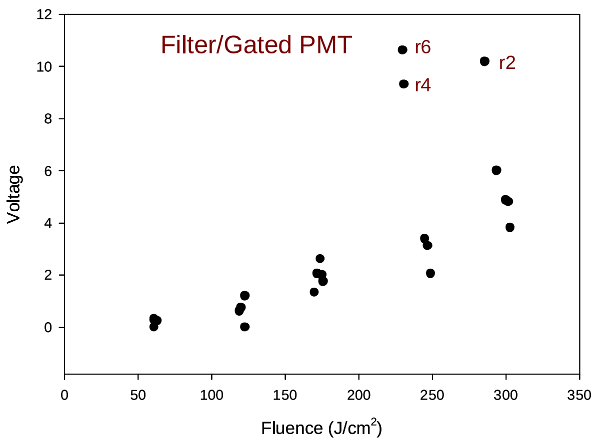

Figure 2.21: Photomultiplier tube voltage responding to the emission levels of 455 nm light at different laser energy densities [13].

2.7 Literature Summary

LSP is a surface treatment technique to effectively increase the fatigue resistance of metal parts by inducing compressive residual stresses. It is a process that relies on shock waves that travel through the metal part, leaving a region of plastic deformation beneath the surface. These shock waves are produced by rapidly expanding metal plasma which is produced as a result of the ionisation within the focal region of a focussed laser beam. Confining the expansion with a layer of water is found to increase the efficacy of LSP.

An interesting phenomenon of laser induced breakdown under sufficient body of water is the formation of cavitation bubbles. These bubbles are affected by their surroundings and input energy.

Before the laser beam reaches the required spot size, the laser power intensity may be sufficiently high that breakdown occurs before the target surface, known as premature breakdown. Since plasma readily absorbs the incoming radiation, this leads to the saturation of laser energy available for peening. This is most obvious in thicker water confinement regimes where the ions in the water allow for greater opportunity to absorb laser energy and begin premature ionisation and water plasma creation. The extent to which absorption occurs is variable. This creates a certain level of uncertainty in the process.

As LSP treats high value parts, diagnostics to monitor the process with thin and thick water layers have been developed that use post processing of coupons, acoustic emission, plasma emission and beam quality methods. There are few to no options that directly reflect the effective laser energy which arrives at the target surface, after all optics and confinement layers.

3 Research Question and Objectives

Research Question

Literature has confirmed the existence of cavitation bubbles as a by-product of submerged LSP. Since this will continue to occur as long as the submerged LSP conditions are met, there is much room for understanding of their formation, maximum size, stability and shape. It may be possible to use insight into this phenomenon to inform a process diagnostic of submerged LSP. In light of this, it is pertinent to ask:

To what extent can the growth and collapse of laser induced cavitation bubbles be used as a diagnostic tool in the LSP process?

To answer this, the following objectives are set out:

- Develop an experimental configuration to evaluate cavitation bubble oscillation periods in the context of LSP.
- Correlate bubble energy with increasing delivered laser power intensity for a range of experimental conditions (i.e. stagnant water, tap water, DI water, flowing, nozzle).
- Determine the effect that target geometries (flat plates, concave channels and convex semi-cylinders with 5 mm to 10 mm radii) and flow regimes have to the behaviour (stability) of laser induced cavitation bubbles.

4 | Apparatus

To achieve the first part of this study's first objective (to develop an experimental configuration), apparatus has been designed, built and commissioned to function with a 532 nm laser. This entailed directing a laser beam into a tank specifically used to conduct cavitation experiments. The tank was created to implement high speed photography while simultaneously capturing the acoustic pressure information within the water. The water tubes and inlets are removable in order to accommodate different flow conditions in the tank. A target movement system allows for sequential laser pulses to hit new material as in would be implemented in a LSP process.

4.1 Laser

Pulsed lasers with sub-hundred nanosecond pulse widths are used in order to generate the high power intensities required to ablate material at relatively low laser output energies [62]. The laser light source used in this investigation is the Thales Saga pulsed laser unit at the second harmonic wavelength of 532 nm. This uses a flash-pumped Nd:YAG rod active medium and a Xenon gas flash tube pump source within a reflective jacket. Ownership and maintenance is undertaken by the NLC in the CSIR in Pretoria, South Africa. A summary of the specifications can be found in Table 4.1.

Directly in front of the laser, an optics box is placed housing a photo diode, a laser attenuator, and a 90/10 beam splitter. The fast acting photo diode allows an oscilloscope to display the full wave at half maximum (FWHM) laser pulse width. The attenuator is actuated by computer controlled stepper motors to allow the laser energy (which is fixed coming out of the laser) to be scaled to any value between 2 and 930 mJ. The beam splitter ensures 90% of the laser energy continues to the target with 10% going to an energy meter. This way the final laser energy can be calculated after attenuation.

The laser beam is reflected by three mirrors to bring it to the same level and location as the optical window in the tank. All mirrors are specified for 532 nm laser light and can be adjusted on their mounts as needed for alignment. The lens is a plano-convex lens with a focal distance in air of 167.8 mm (or a curvature of 50.8 mm), and is mounted on a precision translation stage. This stage allows the position of the lens along the beam path to be finely adjusted, thereby modifying the spot size at the target location. The optical window on the tank is a 50 mm diameter, 8 mm thick, fused silica-glass window, also specified at 532 nm.

Table 4.1: Specifications for Saga HP laser published by Thales [63].

Specification	**Value**
Repetition Rate [Hz]	1 to 10
Energy per pulse [J]	
▷ At 1064 nm	2.5
▷ At 532 nm	1.8
Pulse to pulse energy stability [% rms]	<1.2
Pulse duration [ns]	4 to 8
Time jitter [ns rms]	0.5
Typical beam diameter [mm]	15
Divergence [mrad]	<0.5
Beam pointing stability [μ rad]	± 50
Beam spatial profile [near field]	Top hat
Average Power consumption [kW]	2.4

Since the stimulated emission is not an efficient process, optical pumping of a laser can generate significant heat due to absorption of the light within the lasing medium. This heat is removed by means of a transparent cooling jacket. As such, due to the highest heat transfer being on the periphery of a Nd:YAG laser rod, there is a temperature gradient that develops radially towards the centre of the rod. This results in a gradient of optical refractive index, thermal strain within the medium and elongation that alters the end-face curvature of the rod. These all contribute to making the Nd:YAG rod a positive lens with two focal distances - an effect that is called thermal lensing [64]. This effect will alter the power intensity of the spot since the beam profile as well as the optical spot size will change as the laser warms up, even if the laser output energy does not.

In order to mitigate the effect that thermal lensing has on experiments in LSP, the laser should be operated under steady state temperature conditions whereby any thermal gradients (and therefore laser spot size and beam profile) are relatively constant with time.

4.2 Energy Meter

The energy meter is the FieldMaxII-P and compatible pyroelectric sensor suitable for pulsed laser energy from Coherent Incorporated. This device has an analogue output voltage V_{out} that is proportional to the received energy, E_{laser}. This relationship is given by Equation 4.1 [65]. The input range E_{scale}, full deflection output voltage V_{scale} and wavelength are set manually on the device.

$$E_{laser} = V_{out} \left(\frac{E_{scale}}{V_{scale}} \right) \tag{4.1}$$

The meter is not accurate below 10% of the selected input range, and as such needs to have the range altered for lower laser energies. E_{scale} ranges used here were 3 J and 300 mJ.

4.3 Test Samples and Articulation

Steel was chosen as a suitable target material as these experiments involve repetitive ablation of the target material. This treatment will progressively erode the surface of comparatively soft targets (such as aluminium alloy AA7075-T6511) faster than harder, denser metals such as steel.

The available material included carbon steel Almen strips (AISI 1070 C type grade 1; dimensions 2.38 mm × 19 mm × 76 mm), 304 stainless plate (1.5 mm × 80 mm × 120 mm) and low pressure steam turbine blade alloy (12% Cr martensitic steel 20 mm × 20 mm × 12 mm).

Table 4.2: Properties of Almen strips made of AISI 1070 carbon steel, Grade 304 stainless steel and Din No 1.4939 12CrNiMo martensitic steel [66].

Properties:	AISI 1070 carbon steel	304 stainless steel	12CrNiMo martensitic steel
Density	7.7-8.03 g/cm^3	7.85 - 8.06 g/cm^3	7.8 g/cm^3
Elastic modulus	190-210 GPa	190 - 203 GPa	204 GPa
Poisson's ratio	0.27-0.30	0.265 - 0.275	0.28
Melting Point	1693 - 1733 K	1673 - 1723 K	1693 - 1733 K

4.3.1 3D Printer

To ensure the surface that is ablated is renewed, the sample is moved so that each laser pulse falls on the a different location to the last pulse. An affordable Creality CR20 Pro Three Dimensional (3D) printer (see Figure 4.1) performs this function. With lightweight samples, the articulation accuracy of this device easily conforms to the tolerance of $\pm$ 0.020 inch ($\pm$ 0.5 mm) found in the AMS2546A standard for Laser Peening [67]. Both the pre-existing software and hardware was modified to be better suited to running simple two dimensional scans. An example of the custom GCODE run on the 3D printer in the experiment is found in Appendix A.3.

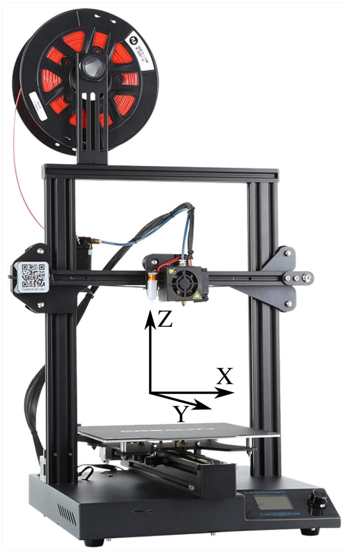

Figure 4.1: CR20 Pro 3D printer from Creality [68].

Hardware Modifications:

- All printing actuators and heating elements were unscrewed and removed.
- The carriage on the X-axis is left intact to bolt onto a matching interface plate.
- The Y-axis is removed from the base of the printer entirely increasing the space within the Z-axis frame and providing a stable, flat area for a tank.
- The X-axis beam is removed and placed on the other side of the Z-axis to ensure there is sufficient clearance such that:
    1. the tank does not obstruct the printer display interface
    2. the high speed camera had sufficient space to image the target site.

- A micro-switch hardware stop is installed for the Z-axis rather than the touch probe which is no longer connected.

Software Modifications:
Because the hardware is altered, some functionality and checks needed to be disabled within the software. The following changes were made on the open-source Marlin firmware:

- All functions that relied on the Y-axis were disabled or commented out, including homing and checks.
- The direction of the X-axis actuation was inverted.
- The Z-axis and X-axis limits were altered to fit the new constraints of the tank walls.
- The default automatic homing and bed levelling functions were set to manual or removed altogether.
- A microswitch hardware stop for the Z-axis was enabled rather than the touch probe.
- Some messages on the display were removed or altered.

Details of each line that is altered can be found in Appendix A.2.

4.4 Water Tank

A transparent water tank was built, containing enough water to confine the laser induced plasma explosion and bubble collapse. Various materials of varying thickness were tested and selected for optical clarity. The sides of the tank were made of common household window glass; when thin enough this had the best optical clarity and availability. Construction consists of two opposing panes of 2 mm glass and 3 panes of 12 mm thick acrylic panes. The outside dimensions of the tank were 300 mm long × 240 mm wide × 220 mm tall. These were chosen purely for the tank to occupy the greatest volume within the physical limitations of the 3D printer frame. When filled to operating capacity (a water level mark 40 mm from the top) it held 11.6 l of water.

The front acrylic pane of the tank had a 55 mm hole milled in the centre of the pane to receive the optical window flange. In addition to this, a second hole is milled on the bottom left corner of this front pane. This second hole is used to receive the female pipe fitting that supplies water inlet from a hose outside. The rear pane had a 5/8 inch British Standard Pipe

(BSP) thread machined to accept a drainage fitting to remove the water from within the tank. The acrylic panes and flange are bonded together using a chloroform solvent and then sealed with silicone caulk. The glass panes and pipe fittings were adhered to the acrylic using the same silicone adhesive. Figure 4.2 displays the glass panels and water pipes used to fill and empty the tank.

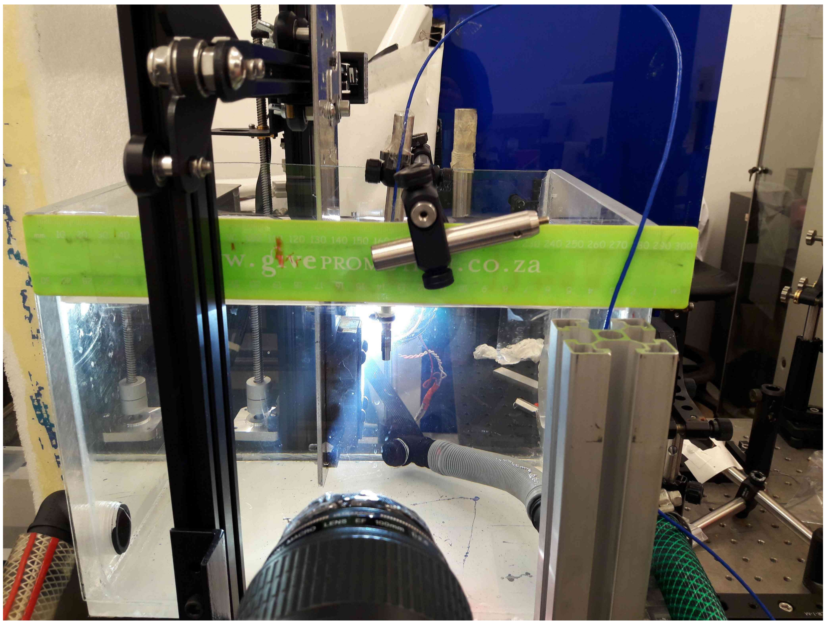

Figure 4.2: Image of filled tank with inlet and outlet pipes within the 3D printer frame, viewed through glass panes above the high speed camera.

A laser grade optical window ensures clarity for the laser beam entering the tank. This optic, being the final interface with the laser in the air, has a coating to reduce dangerous back reflections that could damage the laser. It is made of fused silica glass 50 mm in diameter and 8 mm thick. It is pressed into the flange with a second acrylic ring and M6 bolts. Rubber gaskets ensures a water tight interface with the flange and window surfaces.
For directing water along the beam path, a 50 mm (40 mm bore), 145 mm long, acrylic tube is fitted by a firm friction fit with the optical window flange. Four holes were drilled in the side of the tube and a water jacket (manufactured with a 3D printer) is glued around these holes to allow water to fill and flush through the 40 mm bore along the beam path. This jacket is fed with a flexible hose and Polyvinyl Chloride (PVC) standard pipe elbows attached to the water inlet fitting. A one inch flexible hose is connected to the tank outlet to drain the water easily and safely into a nearby drainage point within the laser laboratory.

4.5 Measurement System

The pressure measurement system, consists of the transducer, signal conditioner, clipper circuit, a Compact Reconfigurable Input/Output (cRIO) chassis with NI9775 analogue acquisition card (outlined in Table 4.3) and a LabVIEW© Virtual Instrument on a computer that records the pressure information. This Data Acquisition Device (DAQ) is illustrated in Figure 4.3. This means of acquiring data was chosen since LabVIEW© is widely used in industry and is readily configurable, ensuring this platform can serve as the basis for any future work or industrial application.

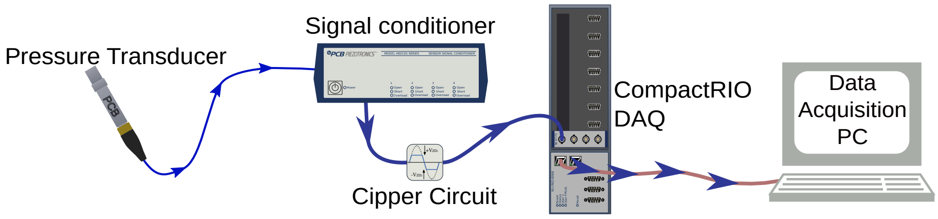

Figure 4.3: Complete pressure measurement system.

Table 4.3: Table of NI9775 analogue input card characteristics.

Specification	Value
Number of channels	4 (simultaneously sampled)
Input type	Reference single-ended
Input impedance	1 MΩ
Input capacitance	24 pF
Input range	Nominal ±10 V
Overvoltage protection	±30 V DC, safe operating area
Input coupling	DC
ADC resolution	14 bits
Typical Gain Error	±0.32%
Typical Offset Error	±0.08%
Non-Linearity	≤ 1.0% full scale
Sample Rate	5 MS/s
Acquisition Length:	10 000 samples/shot

4.6 Transducer

The transducer available for this research, model number 113B21, is a Integrated Circuit Piezoelectric (ICP) sensor from PCB Piezotronics, Inc. This transducer is typically used in compressible gas dynamics and is a fair compromise between affordability and response time. The device and its characteristics of this device is shown in Table 4.4.

Table 4.4: Table of 113B21 pressure transducer performance characteristics [69].

Specification	Value
Useful Overrange(for ± 10 V output)	2758 kPa
Sensitivity(±15%)	3.6 mV/kPa
Maximum Pressure	6895 kPa
Resolution	0.007 kPa
Resonant Frequency	≥ 500 kHz
Rise Time	≤ 1.0 μsec
Low Frequency Response (-5%)	0.5 Hz
Non-Linearity	≤ 1.0% Full Scale

Given the specifications for the analog acquisition card in Table 4.3, when the signal conditioner is turned on, the bias voltage of 24 V would initially exceed the voltage measurement range of ±10 V. As a precautionary measure a clipper circuit (Figure 4.4) made of a pair of reverse biased 10 V Zener diodes was placed in series with the signal conditioner, before the analogue input card to limit the voltage to 10 V.

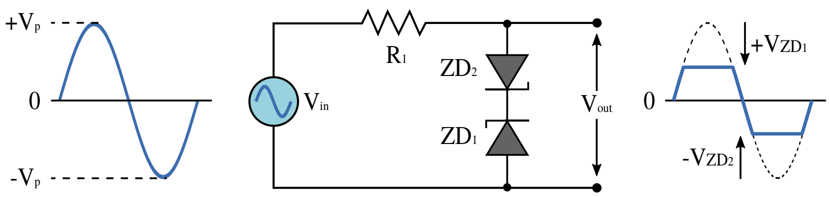

Figure 4.4: Zener clipper circuit, limits the voltage across the output. V_{ZD} is 10 V [70].

4.7 High Speed Camera

The CSIR has ownership of a Phantom V611 Mono high speed camera with a Canon EF100mm f/2.8 USM Macro lens. It can record at a frame rate of around 680 000 frames per second (fps) at a 128×8 pixel frame. An automotive LED light source is used for the illumination of the bubbles at high frame rates. The camera has a brightness threshold trigger based on selected pixels within the field of view. This way the high speed acquisition is triggered when the flash of the plasma saturates a selected region of pixels. The number of frames saved before the trigger point can be configured as well as frame rates and exposure time at various pixel resolutions. The light source and camera are shown in Figure 4.5.

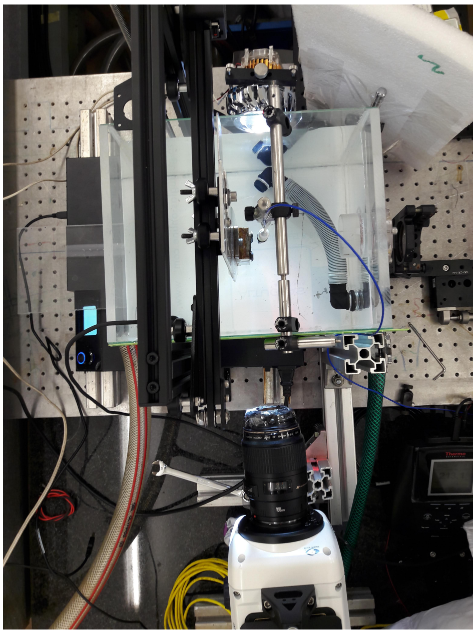

Figure 4.5: Photograph of the tank showing the 3D printer articulating an almen strip target, a submerged transducer, high speed camera and light source viewed from above.

4.8 Full Experimental Overview

The optical and data configuration is provided by the photograph and drawing in Figures 4.6 and 4.7. Mirrors were used to direct the beam to the location and height of the tank. All laser optics, mounts and optical tables are provided by the NLC at the CSIR.

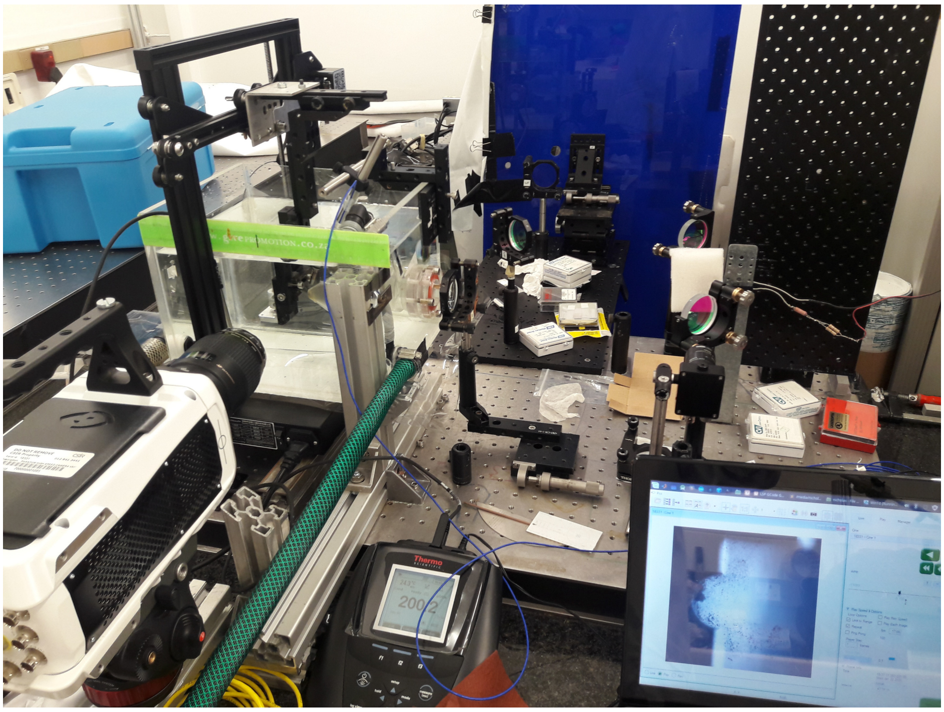

Figure 4.6: Image of filled tank showing inlet and outlet pipes, 3D printer articulating the target and a submerged transducer, high speed camera, beam path mirrors and lens on precision slide, conductivity meter, PC.

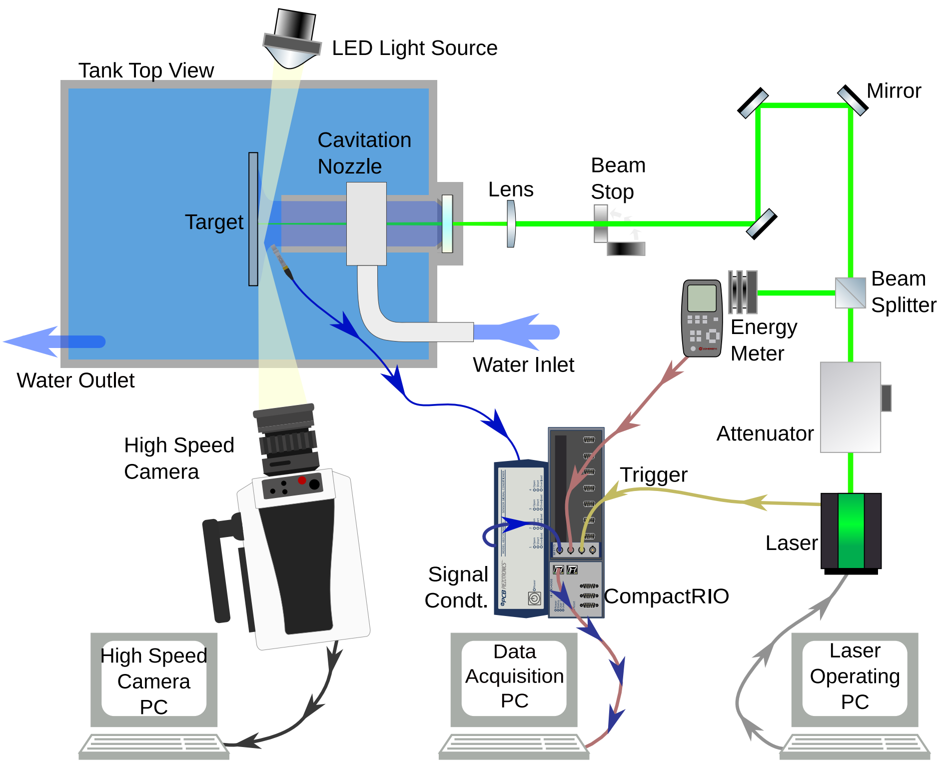

Figure 4.7: Layout of the complete experimental laser induced cavitation bubbles system.

5 Methodology

Section 4 covers the physical and experimental configuration. In order to achieve the primary objective to evaluate cavitation bubbles, a Design of Methods (supported by the chosen apparatus) is required. This Design shall;

1. Produce cavitation bubbles in an observable way. Bubbles cannot be hidden from view, or be too small for the instrumentation sensitivity.
2. Allow cavitation bubbles to be observed in a measurable or quantifiable way. This means numeric values are associated with the quantities that can be measured.
3. Allow for the detailed understanding of first bubble oscillation periods within the measurements.
4. Ensure that conditions similar to industry are tested.

5.1 Producing Observable Cavitation Bubbles

The first requirement for laser induced cavitation is a laser pulse. This is characterised by the output energy of the laser and spot size at a given energy level.

5.1.1 Operating the Laser

Prior to running experiments with a laser, a specific laser safety training course was done. Steps taken to start the laser were set out in a Standard Operating Procedure (SOP) found in Appendix A.5. Before the laser was switched on, the shutter was tested and placed in the closed position. The energy meter was always turned on before the laser itself. This was to ensure that the expected energy of the laser was understood at the first pulse.

5.1.2 Water Tank Preparation

Before the water tank was filled, it was wiped free of potential dust particles (which could lower the breakdown threshold of the water [41]) with damp tissue paper. The tank outlet flow rate (and therefore inlet as well) was limited by the drainage system within the facility.

After establishing this limit, it was set by timing how rapidly a $3\,l$ beaker was filled with tap water. After measuring three times, this flow rate was on average $3\ l/17\ s\ =\ 10.5\ l/min$.

The Orion Star™ A212 Conductivity Benchtop Meter with 013016MD 2-electrode conductivity probe from Thermo Fisher was used in this study [71]. Specific electrical conductivity is typically measured in the units of micro Siemens per cm [μS/cm] and is the inverse of resistivity $1/\Omega$ [72].
The conductivity probe was used to monitor both the temperature and dissolved ion concentration within the water. Care was taken to submerge and agitate the water inside the probe before readings. If a flowing test was done, the probe was placed at the the outlet of the tank such that the water flowed between the conductors of the probe.

Tap Water Tests
The drain valve was opened. The inlet valve was then opened to allow a low flow rate of water to enter the tank through the pipe. Care was taken to ensure no water splashed out of the tank. After filling to the mark ($11.6\,l$), the tank was drained again. It was then filled for experiments. For stagnant tests, a settling time of at least 20 seconds was enforced before commencing with the laser exposure. For flowing tests, the outlet flow rate was set to a fixed $10.5\,l/min$ using the level markers placed on the side of the tank and a stopwatch. The inlet flow rate was then adjusted to match the outlet flow rate, ensuring that the tank water level did not rise or fall significantly (within 5 mm) over a minute.
Deionised Water Tests
The tank and test surfaces were rinsed with two separate batches of older deionised water (around 50 μS/cm) and then with a litre of unused deionised water to wash away any residual tap water from previous tests. It was then filled by pouring water into the top of the tank with both inlet and outlet valves closed. After the test, the waste DI water was collected and recycled the next time the tank needed rinsing as this water still had a lower conductivity than tap water. At the end of the testing each day, the tank was drained and dried with a fabric cloth to ensure that minimal biofilm deposits were left in the tank. As a final step, the anti-reflective coating on the optical window was rinsed with a methanol alcohol stream.

5.1.3 Measuring the Spot Size

Most LSP output parameters (surface roughness changes, residual stress, maximum pressure experienced, etc.) are dependent on the power intensity (which is in turn heavily affected by spot size). This makes obtaining a consistently correct spot size essential within LSP experiments.

An equivalent diameter spot size of 1 mm was used for all tests. This was chosen to ensure that the upper power intensities could be achieved in the available energy range of the laser.

The procedure to obtain the laser spot is as follows:

1. Reduce laser output energy to 30 mJ at 1 Hz using a variable attenuator.
2. Tape down the edges of burn paper onto the target surface, fill the tank with water.
3. While the target is moving (manually or with a rapid feedrate) horizontally, briefly open then close the peening shutter.
4. Remove burn paper from sample and inspect it to ensure single, non-overlapping spots are visible.

The laser energy of 30 mJ was fixed for all burn paper tests, to ensure the spot size measurements correspond to the constant ablation threshold of the same paper rather than the various metal targets. The softening of the burn paper was insignificant after two minutes of being underwater.

The spot size was photographed at a fixed scale using a digital microscope.

1. After identifying the spots of interest, a photograph (see Figure 5.1) was obtained and saved onto a computer.
2. As the spots were not perfectly circular, the area of each spot was then traced using a polygon tracing tool to find the area within the traced region. At least three spots per test were measured this way to obtain an average area for that row.
3. Using this measured area, and the equation $d = \sqrt{\frac{4A}{\pi}}$, an equivalent sized circle diameter was found.
4. A spot size correction equation was found at the same magnification by measuring the scale on accurate callipers (see Figure 5.2a). A linear calibration function (Figure 5.2b) was fitted to the varying measurements to obtain the relationship between measured and actual lengths.
5. This equation was then applied to the equivalent diameters to obtain an accurate set of spot size readings.

.

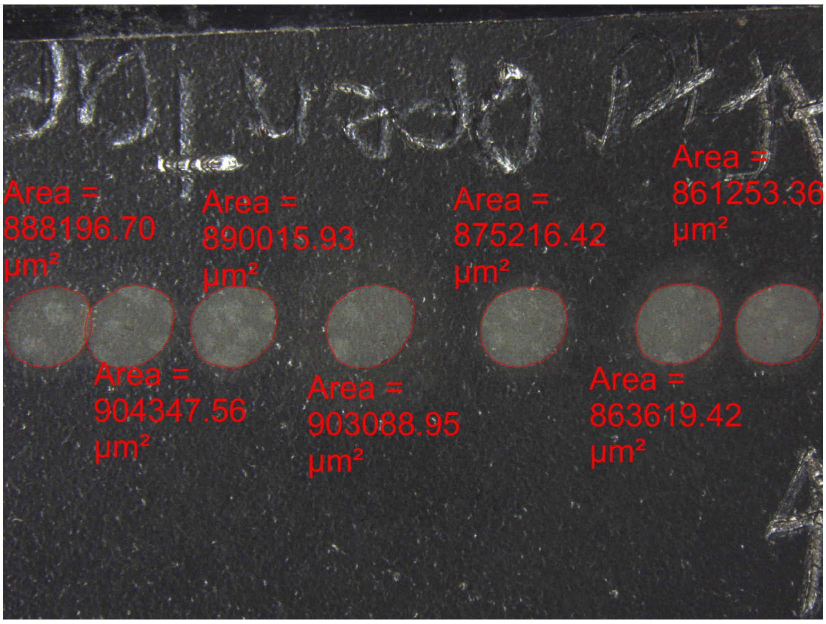

Figure 5.1: The spot size of a single test, measured from an average of seven spots.

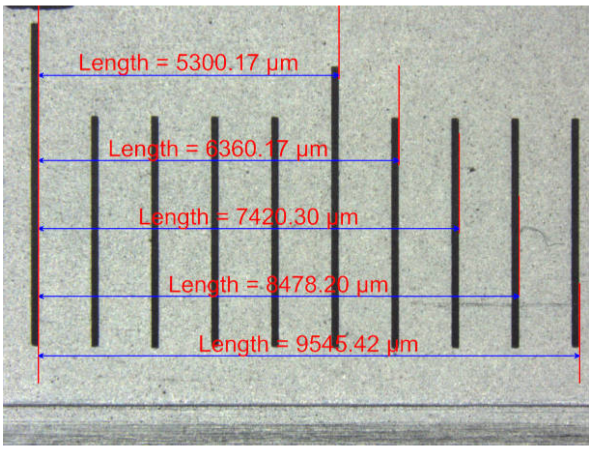

(a) The millimetre scale measurements taken.

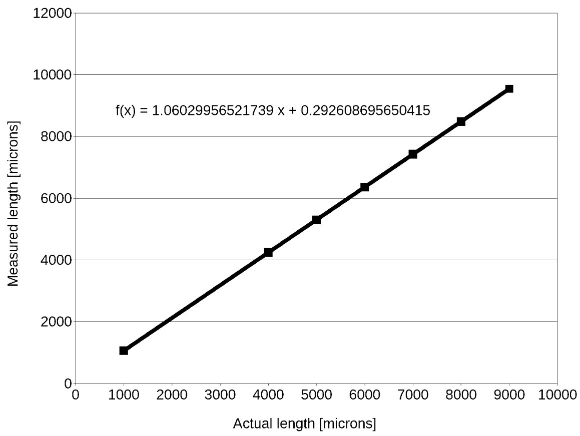

(b) The linear calibration function used.

Figure 5.2: Relationship between the measured lengths and actual lengths was calibrated

The measured spot sizes were then correlated to the laser lens focal length before the tank. By repeating this process to obtain at least two spot sizes at different focal distances along the beam path, a simple linear interpolation could be employed to find the focal length at which the desired spot size is obtained on the target. The focal distance wad adjusted with a precision vernier lens mount.

Since the burn paper was taped on top of the target, its own top surface was closer to the lens than the target surface. However, this extra thickness is a minuscule fraction over the focal length ($0.4\,\text{mm}/200\,\text{mm} = 0.2\%$) and is still an acceptable approximation for the metal surface. Thus, in all experiments, the thickness of the burn paper was not considered and remains constant for every spot size test.

5.2 Measure Cavitation Bubbles

There are many inputs and measurable outputs in LSP research. This study applies special attention to a limited set of inputs and outputs, outlined in Table 5.1 and accompanying Figure 5.3. The parameters that were assumed to be well controlled and constant are given in Table 5.2.

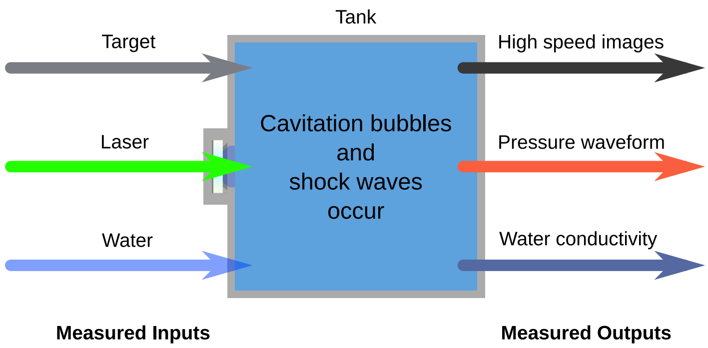

Figure 5.3: Illustration of the main measured experimental parameters.

5.2.1 Observing with High Speed Images

The Phantom Camera Controller software, installed on a separate Microsoft Windows computer, was exclusively used for capturing the high speed footage of the bubble events.

To set the camera trigger, a window was selected on part of the unilluminated test section (a dark edge of the target) such that only when the bright exposure of the plasma event sufficiently lightens the pixels within that window, the camera shutter will trigger. At least three frames prior to the triggered frame were saved so to identify the laser pulse.

Table 5.1: Measured input and output instruments.

Measured Inputs	**Instrument**
Laser energy output	Energy Meter with DAQ
Laser spot size	Burn Paper & Microscope
Initial Water quality	Conductivity probe
Water movement	Flow rate test
Target geometry/location	Callipers/3D printer
Measured Outputs	
Pressure waveform	Transducer & DAQ
High speed images	High speed camera
Final Water quality	Conductivity probe

Table 5.2: Assumed values of constant inputs and outputs.

Unmeasured Inputs	**Assumed to be**
Laser pulse repetition rate	Software controlled 1-10 Hz
Laser output wavelength	532 nm
Laser FWHM pulse width	6 ns
Laser beam profile	Constant Top Hat
Efficiency of the optics	Factory Value
Accuracy of the laser energy meter	Within $< 2\%$
Local atmospheric pressure	87.00 KPa
Water conductivity within the entire tank	Constant throughout
Target surface composition homogeneity	Constant
Laser material interaction for a given target	Constant
Unmeasured Outputs	
Shock wave shape and speed	Spherical, near Mach 1
Camera stability or position	Stably mounted

On average, around 100 frames were saved per laser pulse. The camera and lens were configured to obtain images as outlined in Table 5.3. The exposure time (most often 47 μs) was chosen to produce the best image at the lighting conditions available.

Table 5.3: High speed camera settings used.

Camera:	Phantom v611
Frame Rate:	21005.251313 fps
Resolution:	512 $\times$ 512 px
Exposure:	47 μs
Lens Aperture:	2.8

A focal plane, as demonstrated in Figure 5.4, was created with clear cellophane tape placed perpendicular to the target surface. This was adjusted in increments until the laser beam fell on the edge of the tape. The camera lens was then readjusted to focus on the tape, thus bringing the centre line of the laser beam (and laser induced bubbles) into sharp focus.

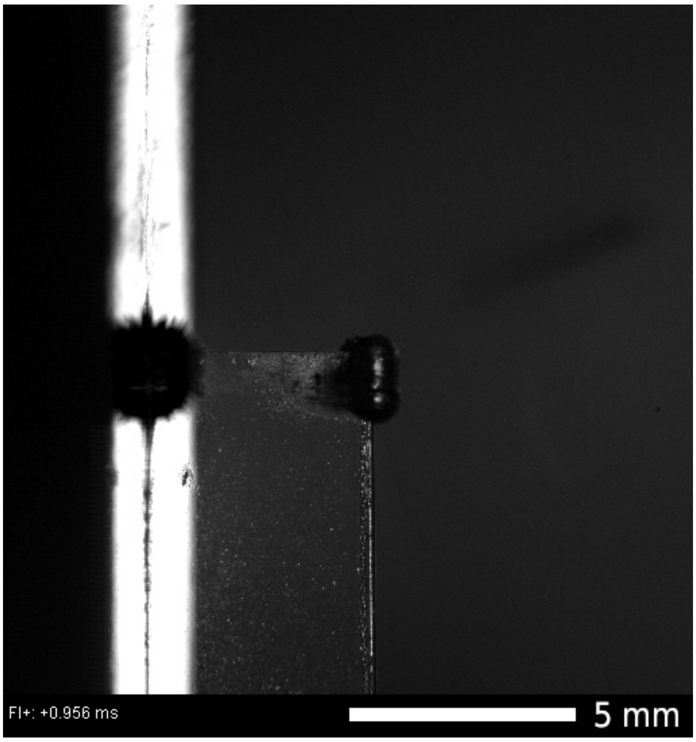

Figure 5.4: Clear tape focal plane, being exposed to the laser. This tape was the reference centre plane of the laser beam path.

5.2.2 Observing Pressure Data

Once the system was initialised and running, the details of each test were filled in on the computer software. These included the estimated laser energy, the water purity and the spot size. A file location was then selected for writing data and a test was run by starting the acquisition, then opening the manual shutter at the same time or shortly afterwards. The shutter was closed when the test was completed and the acquisition was then halted, saving the data file automatically.

The LabVIEW VI used to record the pressure and laser energy information, shown in Figure 5.5, has minimal data processing functionality. All ten thousand data points making up each laser pulse were recorded for post processing with a more reliable tool.

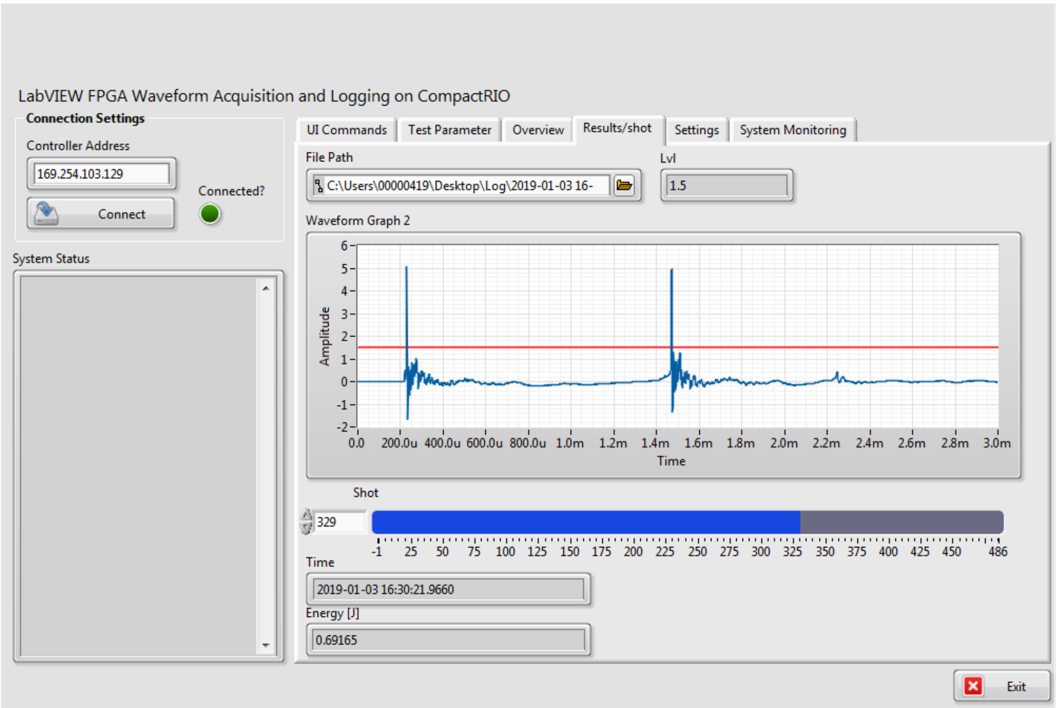

Figure 5.5: Screen shot of the LabVIEW VI application window.

5.3 Measure First Bubble Oscillation

The first bubble oscillation period or bubble lifetime was determined in two ways; 1) by counting the number of frames within the high speed footage between the flash of the laser pulse and smallest measurable radius of the collapsing bubble and 2) by measuring the time between the largest peaks (see Section 6.1) within the pressure waveform. Both these methods, as illustrated in Figure 5.6, have been extensively used in literature [7, 61].
With this bubble lifetime, the associated energy of the cavitation bubble could be calculated for a given laser energy input. The reason for obtaining high speed imagery in this study was to validate the existence and behaviour of cavitation bubbles and so correlate features within the pressure waveform to reality.

The pressure waveform could provide information other than the bubble lifetime, such as shock wave pressure, but to a less reliable extent. This was firstly because the transducer has a response that is too slow (discussed in Section 6.4) to resolve intricate shock features, and secondly because any high pressure signals were limited by the clipper circuit (Figure 4.4) used to protect the DAQ. For these reasons, the information other than cavitation bubble lifetime was not prioritised within this study.

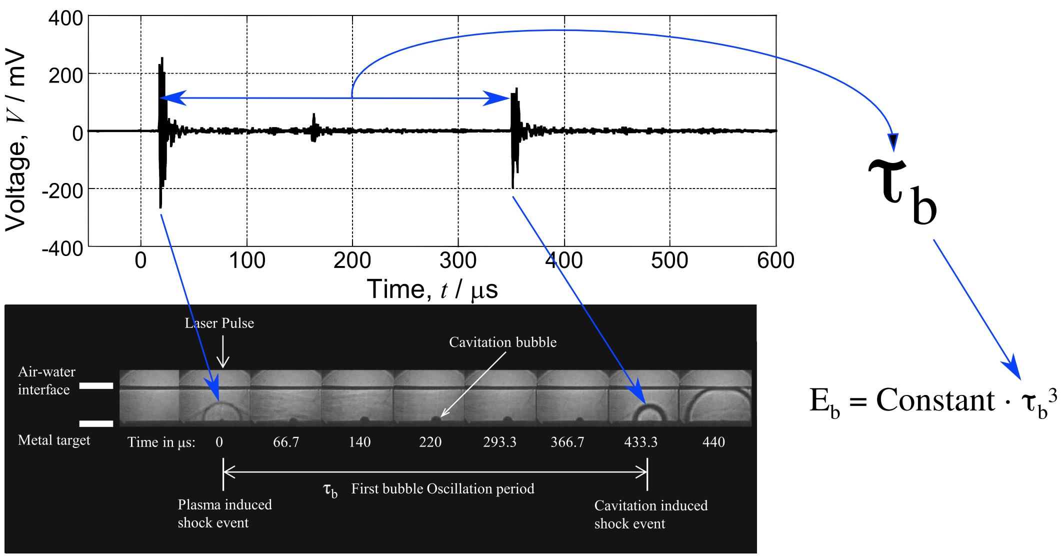

Figure 5.6: The pressure information can be shown to represent the reality seen in pictures [7, 61]. The bubble energy is dependent on the time between the two pressure spikes raised to the third power, in Equation 2.6.

5.4 Testing Industry Conditions

There are three main differences between LSP research in a lab facility and production facility for a given application. These account for an increased cost efficiency and treatment output within industry:

- A higher coverage rate: increased laser pulse rate, or larger laser spot size with same power intensity.
- Changing geometry and sample movement to treat different parts.
- Increased water layer replenishment to meet the containment demands of high laser pulse rates.

Based on this understanding, the preliminary stagnant experiments were modified to closer resemble an industrial setting before measuring bubble lifetimes. The laser repetition rate was increased, the sample was moved, and flowing water was introduced. The effect of each input was quantified before another aspect in industry was introduced.

5.5 Experimental Outline

The procedure to be followed is illustrated in Table 5.4. The expectations of the system were first established with a number of baseline experiments. Following these, the effects of a tube was introduced. With this, flowing experiments were done to inform expectations under these conditions. Finally, the geometry of the target was altered to explore the sensitivity of bubbles in this regard.

Table 5.4: Summary of experimental flow.

<table>
<tr>
<td>

- Stagnant tests with both Tap and DI water.
- Changing the Repetition Rate.
- Lengthy Test Duration.
- Energy change test.

</td>
<td>Stagnant Conditions</td>
<td>
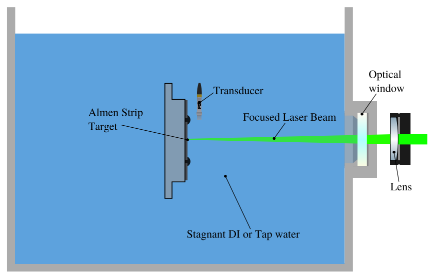

</td>
</tr>
<tr>
<td>

- Effect of tube, stagnant and low velocity flow.
- Effect of larger 304 stainless steel plate.
- Saturation of laser energy transfer.

</td>
<td>Flowing Conditions</td>
<td>
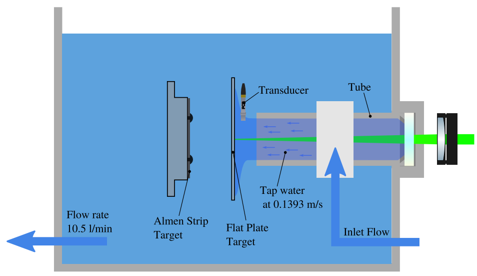

</td>
</tr>
<tr>
<td>

- Near edge effect with low flow velocity.
- Effect of the geometry and turbine material with a higher flow velocity and increased repetition rate.

</td>
<td>Geometry Conditions</td>
<td>
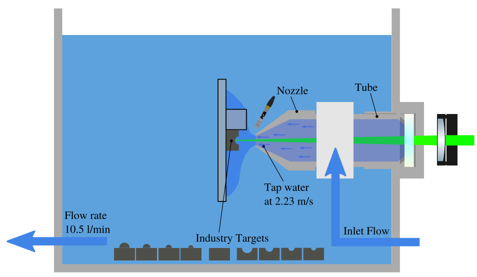

</td>
</tr>
</table>

The reasoning behind the experiments and their anticipated results are outlined below:

- Stagnant high speed images
  - As a validation of the apparatus, this experiment allowed the camera parameters and position to be adjusted if necessary. The water was kept stagnant.
  - Anticipated results include the shape and size of the laser induced cavitation bubbles, potential breakdown within the water and a first estimate for bubble lifetime for both DI and tap water.
- Effect of laser repetition rate in stagnant water
  - In anticipation of the increased repetition rate in an industrial setting, a baseline understanding was sought of increased laser repetition rate, at different power intensities, in stagnant water. All apparatus should be fully functional at this point.
  - Results include pressure derived bubble times for four different repetition rates.
- Effect of test duration within a fixed volume of water
  - A longer, higher energy test than any other was run to produce the highest LSP by-product concentration within the same tank, thought to reduce the dielectric strength of the water. To ensure no immediate beam blockage occurred, a small submersible aquarium pump was used to agitate and circulate the water near the target.
  - Results include bubble lifetime and conductivity change over a course of at least 10 minutes.
- Relationship between laser energy and bubble energy in stagnant tap water
  - To achieve the second objective of this study, the laser energy was varied with a fixed spot size to understand the relationship to cavitation bubble energy. Tests were done with a long wait (twenty seconds) between shots to allow for stagnant conditions.
  - Results include a correlation between laser input and bubble time or bubble energy as well as the measurement uncertainty as a measure of dispersion. These tests were repeated to ensure consistency with the results.

- Effect of a tube in stagnant water
  - To guide flowing water along the beam path, enabling one more industry-like condition (and as designed in Section 4.4), a 40 mm internal diameter acrylic tube was introduced to the tank.
  - Results include a comparison between tube and no tube at similar water conditions.
- Effect of flowing water at slow repetition rates
  - To understand if replenishing the confinement water had any effect on the bubble lifetime and variation, the set flow rate of 10.5 l/min was allowed to flow through the tube collinear to and surrounding the laser beam path. The water was given surplus time to be renewed between shots at the low pulse rates of 0.05 Hz and 1 Hz.
  - Results include the effect of flow on the bubble life time and stability.
- Effect of different flat target
  - A new target material (304 stainless steel) was introduced to allow for a larger, flat plate to be studied. This was most like any large panel on vehicles or vessels.
  - Results include the effect that the change in material and larger geometry has on the cavitation bubble lifetime.
- Saturation of multiple results
  - From prior tests, the relationship between bubble lifetime and laser input tended to saturate, or become less sensitive to changes in input.
  - Results show the estimated point at which this occurred for varying tests.
- Effect of edge at fixed power intensity
  - The effect on cavitation bubble lifetimes when a LSP beam nears an edge, was tested at a fixed power intensity. This scenario is likely if the full dimensions of a plate were to be processed.
  - Results include bubble shapes, behaviour and lifetimes when positioned between off the edge to the middle of a 304 stainless steel plate.
- Effect of geometry radii at single power intensity, with higher flow velocity
  - In order to understand how cavitation bubbles behave within niche industrial applications of LSP a range of targets with varying radii of curvature was tested. Targets used were made of 12Cr martensitic steel, closely resembling that which is used in turbine blade construction.

- Results include cavitation bubble behaviour and lifetimes at a fixed power intensity, for targets ranging between -5 mm to +5 mm in curvature. The effect of a nearby inside corner and increased laser repetition rate was also considered.

5.6 Broad Test Procedure

Repeatability in the measurements (both inputs and outputs) were improved by ensuring a minimal drift over multiple measurements of the same condition (laser energy, spot sizes, bubble times) and allowing for settling time of laser operation and water conditions. A full test is outlined as follows:

- Switch on the laser in order to warm up (using SOP in Section A.5)
- Set the spot equivalent diameter to 1 mm.
- Load GCODE with the desired scan pattern and feed rate onto 3D printer (such as that in Section A.3).
- Mount target firmly.
- Begin test
  1. The details of the test and saving path are entered into the acquisition software.
  2. The laser output energy is verified to be correct and at the desired repetition rate.
  3. The required water flow rate is obtained without overflowing/draining the tank. If stagnant, the water is perfectly still and free of bubbles.
  4. The GCODE is run on the 3D printer articulation (see Appendix A.3).
  5. If used, the high speed camera trigger is armed.
  6. The "Record" button in the acquisition software is pressed to begin logging data.
  7. The manual shutter is opened to allow the laser light to reach the target.
- End test
  1. After sufficient time (number of shots or seconds) had passed, the manual shutter is closed.
  2. The data acquisition is halted (clicking Record button again) and saved automatically in the selected path.
  3. If used and successfully triggered, the high speed camera raw cine is then saved for further processing later.

6 | Data Processing

The raw, unprocessed data files that were obtained from the LabVIEW acquisition system are stored as Technical Data Management Streaming file format (TDMS) files. These raw files consist of data points that have X and Y values (sample number and voltage) as well as the associated parameters that are saved from the user interface.

Post processing was done on these using MATLAB, a comprehensive matrix based programming environment. The peak detection, uncertainty analysis, energy meter calibration and graphing were all executed using this tool.

6.1 Peak Detection

The flow of data processing is as follows;

1. Import TDMS file into MATLAB environment.
    - The data file from the DAQ system is saved as a TDMS file.
    - Using a library written by Hokanson [73], the components of the data file are extracted. This is the most time consuming part of the process and is lengthened exponentially by file size.
2. Select only the data that has waveforms recorded from the DAQ.
3. Detect the peaks, their locations and determine the distance between the most prominent peaks as a time.
    - The `findpeaks` function (Figure 6.1) within the MATLAB environment is employed [74]. It finds the local maximum points above a specified height and within a specified distance apart. In doing so, it allows the time between the peaks to be reliably and accurately calculated.
4. Record this distance as bubble time, and convert all data to useful units of pressure, time and laser energy or power intensity.
5. Write this data to a file.
6. Plot the data and statistics (see Appendix A.4).

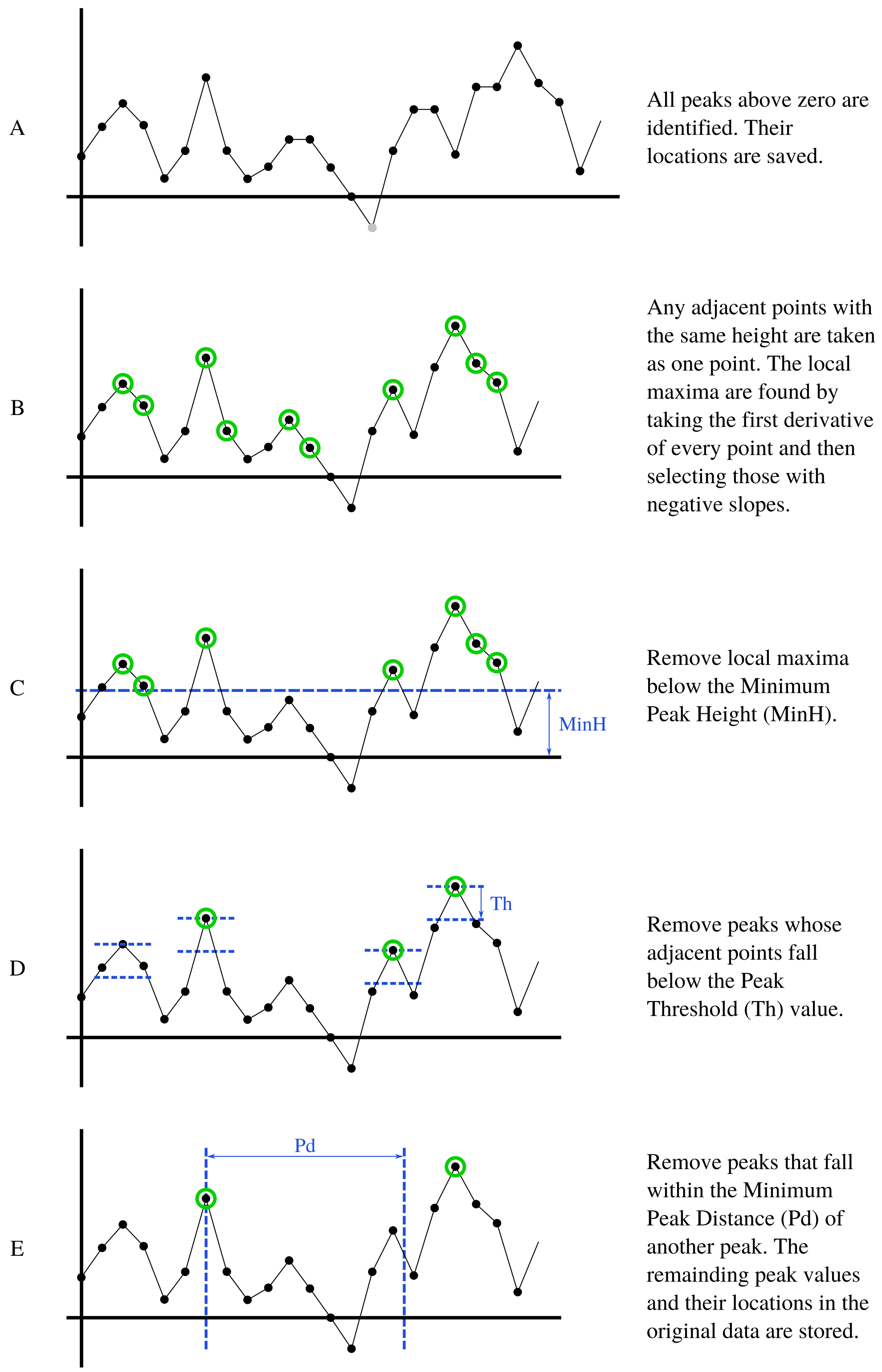

Figure 6.1: The general method by which peaks are found using the `findpeaks` function in MATLAB. Other features of this function such as peak width are not used [74].

6.2 Flow Velocity

In this study, two flow cross sections were used, making use of exits with internal diameters of 40.0 mm (in Figure 4.7) and 10.0 mm. Thus, for the areas of the exits A_1 and A_2:

$$A_1 = \frac{\pi D^2}{4} = \frac{\pi(40.0)^2}{4} = 1257\,mm^2$$

$$A_2 = \frac{\pi D^2}{4} = \frac{\pi(10.0)^2}{4} = 78.54\,mm^2$$

The volumetric flow rate $\dot{V}$ of a fluid through a tube is defined as

$$\dot{V} = A \cdot v \tag{6.1}$$

and for a constant flow rate of

$$\dot{V} = 10.5\,l/min = 175 \times 10^3\,mm^3/s$$

the velocity of the water coming out of the 40 mm tube v_1 is:

$$v_1 = \frac{\dot{V}}{A_1} = \frac{175 \times 10^3\,mm^3/s}{1257\,mm^2} = 0.139\,m/s$$

and the velocity of the water coming out of the 10 mm conical nozzle v_2 is:

$$v_2 = \frac{\dot{V}}{A_2} = \frac{175 \times 10^3\,mm^3/s}{78.54\,mm^2} = 2.23\,m/s$$

6.3 Uncertainty Analysis

In experimental measurements, the value of the measurement will almost never be exactly the true value in reality. Each device that measures the physical world has a degree to which the accuracy of the measurement is unknown. This degree is called uncertainty [75]. The analysis of this uncertainty is the process by which researchers identify, quantify and combine the random and systematic errors of a measurement.

6.3.1 Design Stage Uncertainty Analysis

Design stage uncertainty analysis is based on the resolution of the device and assumes the other sources of error are negligible. U_d is calculated using interpolation U_0 and instrument U_c errors [75]:

$$U_d = \sqrt{(U_0)^2 + (U_c)^2} \tag{6.2}$$

Details of this analysis can be found in Appendix A.1.

Table 6.1: Design uncertainties of the pressure and laser energy measurements.

Design Uncertainty (U_d)	**Value**
Pressure	$\pm$ 21.148 kPa
Laser Energy	$\pm$ 0.0204 J

6.3.2 Uncertainty of Multiple Data Points

Figure 6.2 outlines the process of estimating the uncertainty associated with multiple measurements, as is the case in the experiments undertaken in this study. This procedure is taken from Figliola and Beasley [75].

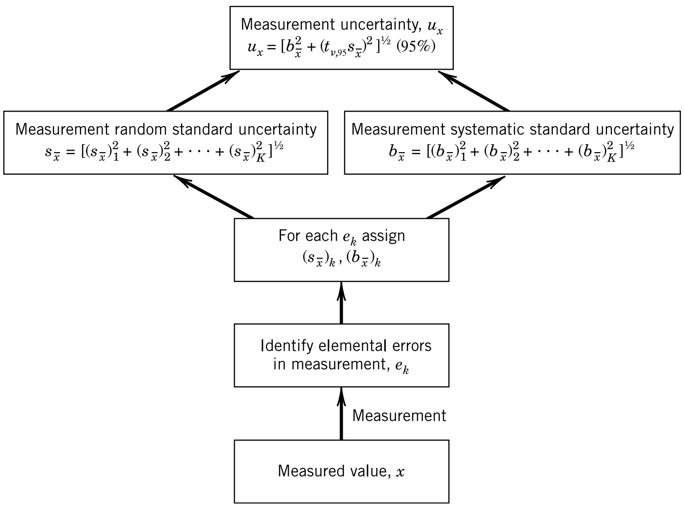

Figure 6.2: Procedure for combining multiple measurements [75].

The systematic errors are first calculated and summed.

$$b_{\bar{x}} = \left[(b_{\bar{x}})_1^2 + (b_{\bar{x}})_2^2 + \cdots + (b_{\bar{x}})_k^2\right]^{1/2} \tag{6.3}$$

These are equivalent to the calculated design uncertainties.

$$b_{\bar{x}} = (U_d)$$

The standard random uncertainty $s_{\bar{x}}$ is then estimated. Each measurement contribution $(s_{\bar{x}})_k$ is found by taking the standard deviation for that data set and dividing it by the root of the number of data points.

$$(s_{\bar{x}})_k = s_{x_k}/\sqrt{N_k} \tag{6.4}$$

$$s_{\bar{x}} = \left[(s_{\bar{x}})_1^2 + (s_{\bar{x}})_2^2 + \cdots + (s_{\bar{x}})_k^2\right]^{1/2} \qquad (95\%) \tag{6.5}$$

In order to look up a $t_{\nu,95}$ estimator, the degrees of freedom in the result ν are found from each degree of freedom ν_k from every dataset and asscociated standard random uncertainty $(s_{\bar{x}})_k$. Equation 6.7 is called the Welch-Satterthwaite formula [75].

$$\nu_k = N_k - 1 \tag{6.6}$$

$$\nu = \frac{\left(\sum_{k=1}^{K} (s_{\bar{x}})_k^2\right)^2}{\left(\sum_{k=1}^{K} (s_{\bar{x}})_k^4 / \nu_k\right)} \tag{6.7}$$

The $t_{\nu,95}$ estimator is found on a t-distribution table with the degrees of freedom at a confidence interval of 95% [75]. This is then used to find the expanded uncertainty in the result, given as

$$u_R = \left[b_{\bar{x}}^2 + (t_{\nu,95}s_{\bar{x}})^2\right]^{1/2} \qquad (95\%) \tag{6.8}$$

Finally, the best estimate of a value R to a confidence interval of 95% is

$$R' = \bar{R} \pm u_R \qquad (95\%) \tag{6.9}$$

where $\bar{R}$ is the mean value of R.

This analysis is carried out with every dataset and is displayed on plots in subsequent sections in the form of horizontal and vertical measurement uncertainty error bars.

6.3.3 Uncertainty of Terms within Bubble Energy

Perturbation uncertainty was used to determine the design uncertainty $b_{\bar{x}}$ associated with the bubble energy for a given operating point. The individual uncertainties of each term within Equation 2.6 (rewritten below) is given in Table 6.2. Three time based uncertainties were identified to contribute that the bubble lifetime uncertainty τ_b.

$$R_0 = \frac{\left(P_{0_{day}} - Pv_{temp}\right)^{\frac{5}{2}}}{\left(1.43031(\rho_{temp})^{\frac{1}{2}}\right)^3} \tau_b^3$$

Table 6.2: Each individual uncertainty u_i for perturbation of the bubble energy.

Term	u_i
$\tau_{b_{velocity}}$	$\pm\, 1.35 \cdot 10^{-5}$ s
$\tau_{b_{peak}}$	$\pm\, 1.20 \cdot 10^{-6}$ s
$\tau_{b_{movement}}$	$\pm\, 1.35 \cdot 10^{-5}$ s
ρ_{temp}	$\pm\, 2.56\,\mathrm{kg/m^3}$
Pv_{temp}	$\pm\, 1.91 \cdot 10^{3}$ Pa
$P_{0_{day}}$	$\pm\, 2.06 \cdot 10^{3}$ Pa

Accounting for these uncertainties by perturbation and combining them together is shown in Appendix A.1.3. The uncertainty of the bubble lifetime measurement is insensitive to the lifetimes when cavitation bubbles are very small, and most sensitive when these bubbles are large. This is seen as a cubic response when the uncertainty of multiple operating points (0 to 1.5 ms) are plotted in Figure 6.3a.

A linear increase in uncertainty occurs with increasing bubble energy, as Figure 6.3b illustrates, which means the uncertainty of the bubble energy is linearly dependent on the magnitude of the bubble energy. This relationship is only altered with tiny (microscopic) bubbles, when the uncertainty of the other terms in the bubble energy equation become comparable to the bubble lifetime term. This is further explained in Appendix A.1.3.

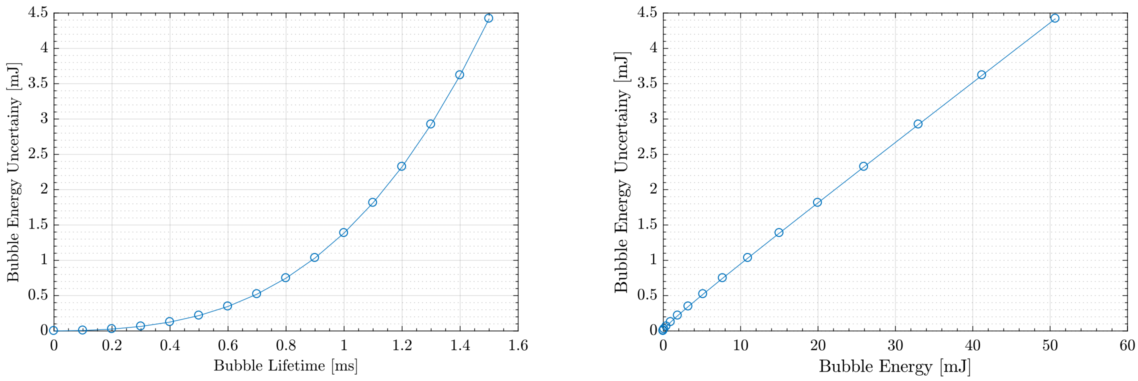

(a) Uncertainty of calculated bubble energy associated with varying bubble lifetimes.

(b) Uncertainty of calculated bubble energy associated with varying bubble energies.

Figure 6.3: Uncertainty of calculated bubble energy associated with varying bubble lifetimes and bubble energy. This study produced bubble lifetimes not larger than 1.6 ms.

6.4 Sampling

The signal that was recorded by the data acquisition system was one that was from an analogue, continuous real event. This means to adequately represent this continuous signal in a digital form, an understanding of sampling is required.

To adequately reconstruct a continuous signal with discrete samples, the sampling frequency must be larger than two times the highest frequency component in the signal. This condition is known as the Nyquist Criterion [76]:

$$F_{sample} \geq 2F_{signal}$$

The minimum frequency that satisfies this condition is known as the Nyquist rate. If the sampling frequency does not satisfy the Nyquist criterion, or it is lower than twice the maximum frequency component, then an effect called aliasing occurs. Aliasing is when a sampled waveform is misrepresented as a slower waveform signal. The fastest signal F_{signal} that is produced by the transducer can be taken as the inverse of the rise time specified 1 μs;

$$F_{sample} \geq 2\frac{1}{1\,\mu s}$$

$$F_{sample} \geq 2\,MHz$$

In this study, F_{sample} will be 5 MHz, a sampling frequency that is convincingly above the response of the transducer, satisfying the Nyquist Criterion.

The ability of the transducer to represent the pressure information within a shock wave is now considered. In order for the transducer to resolve the peak pressure of a passing shock wave (see Figure 6.4) in water, its rise time has to be correspondingly faster than the wave passing time. If the shock wave is travelling at near the speed of sound in water which is around 1481 m/s (Mach 1 in water) it will transverse the diameter of the transducer (6.22 mm) in 4.2 μs. Since the rise time is less than 1 μs, the transducer will respond quickly enough to resolve an event that lasts 4.2 μs.

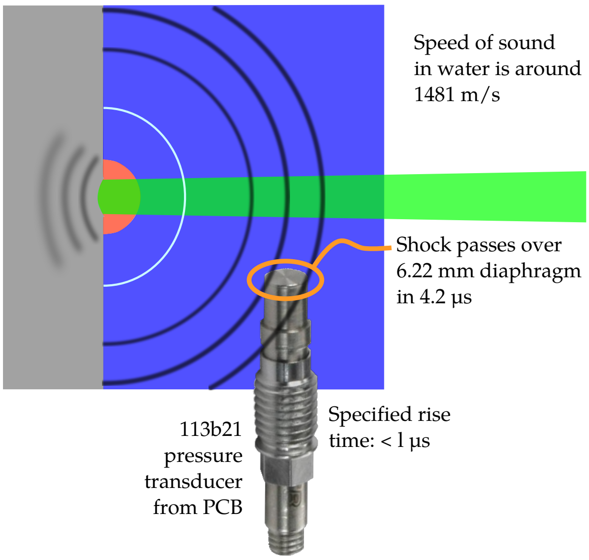

Figure 6.4: Shock wave passing transducer.

This initial analysis does not take the transducer fundamental resonant frequency into account. In a white paper by Walter, from PCB Piezotronics, Inc. [77], it is recommended that to prevent excited transducer resonant frequency from being superposed on the recorded data, the rise time should follow this general rule of thumb:

$$\tau f_n = 2.5 \tag{6.10}$$

where τ is the 10-90 percent rise time and f_n is the resonant frequency of the transducer. From Table 4.4, the 113B21 sensor has a fundamental resonant frequency of 500 kHz. Thus the transducer's fastest response is;

$$\tau f_n = 2.5$$
$$\therefore \tau = 5\,\mu s \tag{6.11}$$

By this analysis, the shock passing event that lasts 4.2 μs is not resolved by the transducer to an convincing margin. While this is not ideal, and likely means the resonances from the transducer are superimposed on the waveform, for the purposes of this study the exact shape of the waveform is not essential to extract a resonable result. This is discussed further in Section 7.1.4. Instead, the repeatability and reliability of the transducer response between shock waves is of greater concern.

6.5 DAQ Voltage Calibration for Energy

The energy meter is calibrated and considered accurate (documented in Table A.2), but there is an undocumented relationship between the meter's output measured by the DAQ and the recorded energy, in this particular instrumentation arrangement, outlined in Figure 6.5.
In order to convert the voltage from the energy meter to an energy, the conversion function, Equation 4.1 is suggested by the manufacturer. This linear function was found to poorly represent the unknown voltage-DAQ-energy relationship. Table 6.3 was drawn up based on set energy points observed on the display of the energy meter device. It is used as a lookup table in order to adjust the analogue output voltage values (V_{out}) from the DAQ within an energy range. The constant multiplier at each energy level was adjusted by hand until the calculated energy was within 1% of the display value for at least 100 laser pulses. This table is used with Equation 6.12 with the output voltage range V_{scale} fixed at 2 V.

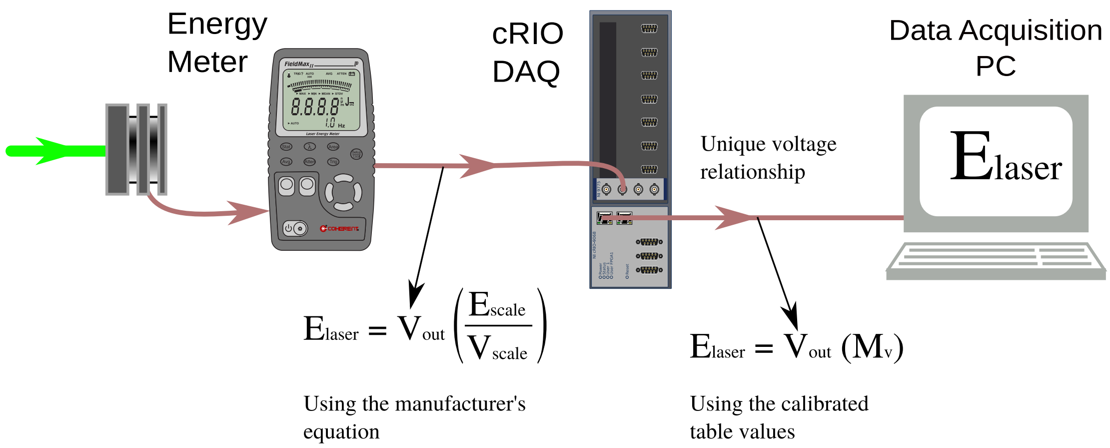

Figure 6.5: Diagram of voltage energy relationship within the data acquisition system.

$$E_{laser} = V_{out} \left(M_v \right) \tag{6.12}$$

Table 6.3: Calibration values for the energy meter output.

Display	Voltage multiplier M_v [J/V]	
$\bar{E}_{laser}$ [mJ]	$E_{scale} = 3$ J	$E_{scale} = 300\,\text{mJ}$
50	1.191	0.1403
100	1.191	0.1441
150	1.288	0.1456
200	1.341	0.1483
250	1.357	0.1482
300	1.350	N/A
350	1.37	N/A
400	1.39	N/A
450	1.405	N/A
500	1.41	N/A
550	1.391	N/A
600	1.388	N/A
650	1.388	N/A
700	1.4	N/A
750	1.41	N/A
800	1.391	N/A
850	1.391	N/A
900	1.391	N/A

7 | Results and Discussion

The effect that each disturbance made to the system was found by starting the experiments in a simple, baseline scenario and noting the effect of a disturbance, one at a time. Experiments in this chapter, presented in Figure 7.1, progress from the very simplest submerged target with stagnant water to more complex targets with flow along the beam path, eventually recreating an industrial application.

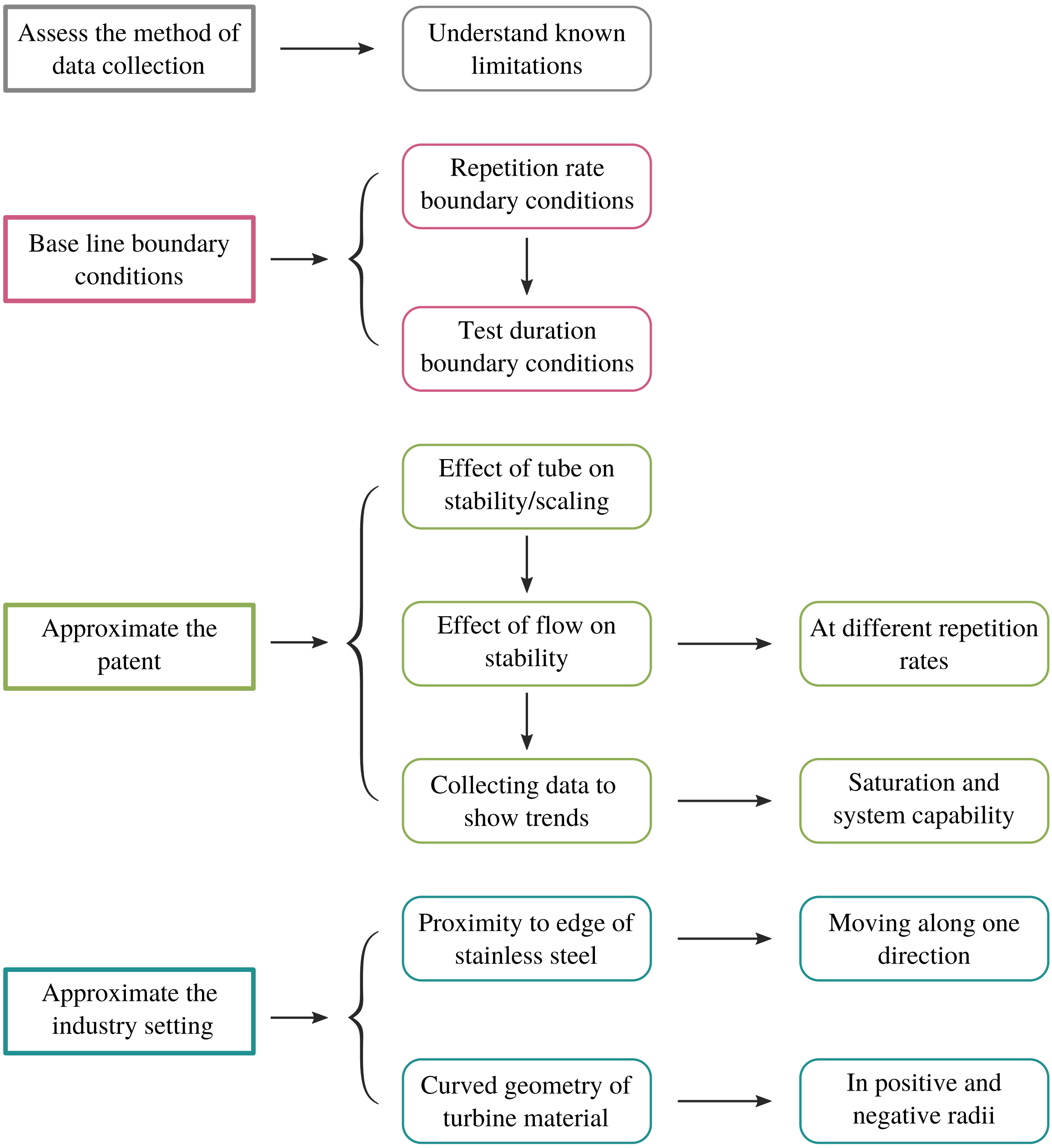

Figure 7.1: Summary of the experiments undertaken.

7.1 Data Collection Assessment

7.1.1 Spot Size Variation

The variation of actual spot sizes was recorded and is plotted in Figure 7.2. With a laser pulse frequency change from 10 Hz to 1 Hz within the same day, the spot size reduced. It should also be noted that on the two days multiple spot checks were done, the spot size reduced as the day progressed.

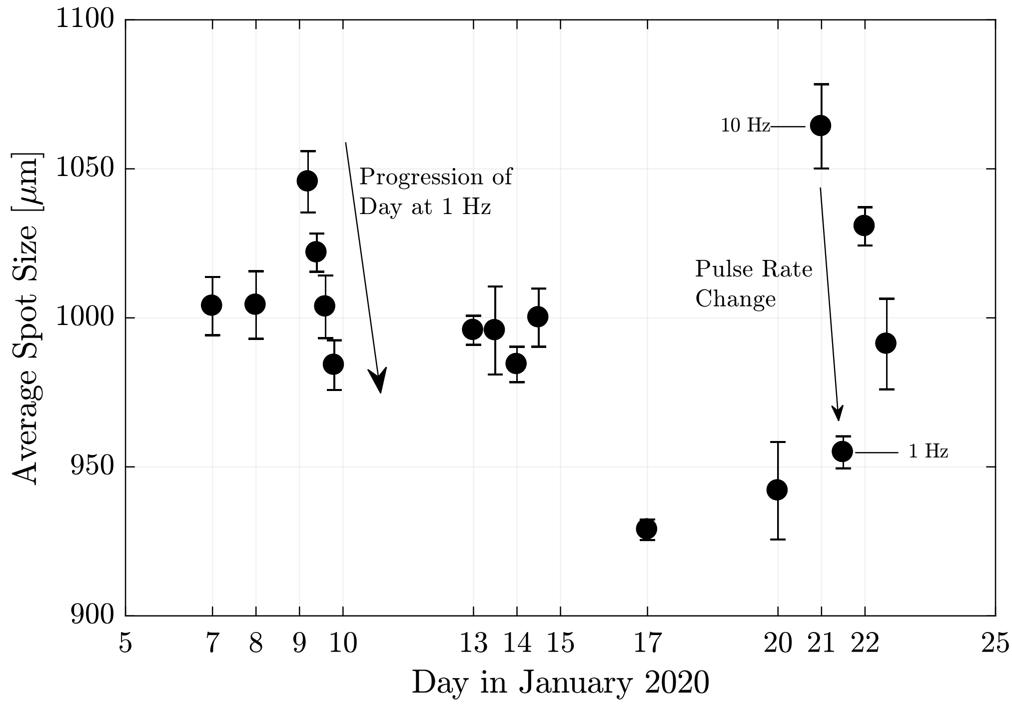

Figure 7.2: Spot sizes over the course of the testing period. Each point represents an average of at least four spots, error bars are the measurement uncertainty of that average.

The progressive reduction of spot size over the course of a day in Figure 7.2 is currently unexplained as both the room housing the laser unit and the laser cooler unit itself were temperature regulated near 20°C. Meticulous temperature measurements could validate this in future work.

However, in the same figure, the immediate change in spot size shown with different laser repetition rates could be explained by a form of thermal lensing, with a diverging lens effect on the laser or any optical components along the beam path. The increased pulse rate translates to an increased heat input into imperfect components. For the same heat loss, an increased temperature difference would occur. By increasing the thermal load on the lasing medium and optics in the beam path, a larger spot size was produced. This result, however, is contrary to the findings in literature, that thermal lensing would reduce the overall focal length thereby reducing the spot size [64].

The difference between laser pulse rates of 1 Hz and 10 Hz translates to a power intensity change of 1.8150 GW/cm^2. The maximum range of spot size change over the course of a day corresponds to a power intensity change of 1.0012 GW/cm^2.

7.1.2 Pressure Measurement

A detailed understanding of the pressure information is important to ascertain the extent to which the data acquisition system can resolve shock events. This section aims to understand the output waveform of the pressure transducer.

Observations

The waveform obtained from the DAQ is shown in two plots in Figure 7.3. The peaks of the shock events showed good prominence with a large signal to noise ratio. This waveform looks similar to that in Figures 2.20b and 2.19a. One notable difference is the comparatively lower negative peak pressure after the initial shock front pressure.

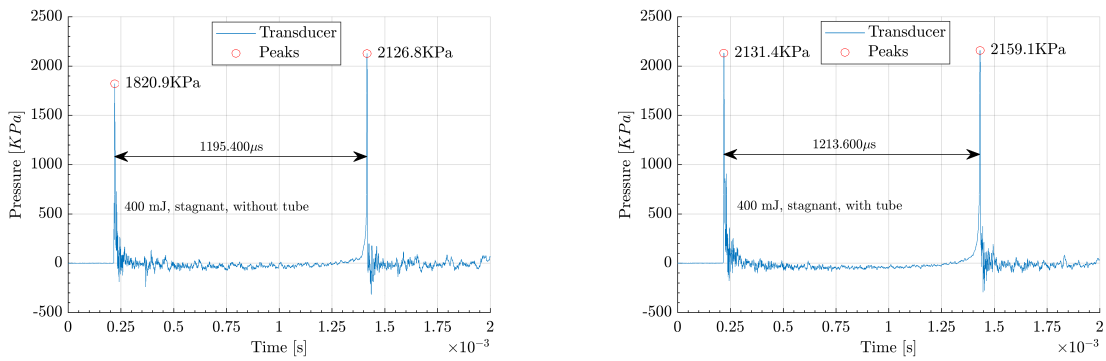

(a) First and second shocks without tube.

(b) First and second shocks with tube.

Figure 7.3: Comparison of different shock waves defining a single bubble's first oscillation period or lifetime.

Figure 7.4 shows the pressure information of the two separate shock events in greater detail. The shock wave from the laser event was resolved as a rapid rise in pressure from zero. There is a distinct zig zag pattern that is present on the rising edge of the open water test. This feature, present in multiple shots without the tube, was not found when a rigid tube was placed in the beam path underwater. Instead, a clear, smooth rise to maximum pressure was recorded on the shots fired in stagnant water accompanied with a tube. This strongly suggests that it is a shock wave feature dependent on surroundings, potentially the manner in which the shock front meets the transducer diaphragm or body. The DAQ appeared capable of recording these subtle differences.

Following the peak pressure and rapid drop, oscillations around zero are shown consistently in both plots, with and without a tube. This is likely a combination of both turbulent flow in the wake following the shock wave and the response of the transducer to the sharp pressure changes. Oscillations of the same nature are seen in Figure 2.14.

Regarding the bubble collapse shock, there was a gradual increase in pressure to around 250 kPa before a steep and rapid rise in pressure to the second peak in the waveform. This gradual rise before the pressure spike was present in all cases of successful cavitation collapse, attributed to the inrush of water, flowing to fill a bubble cavity. The shape of both laser induced shock and cavitation bubble collapse shock waveforms in Figure 7.4 compare favourably to that in Figure 2.15, displaying the same sharp and gradual rises of the two events respectively. Frequently, the magnitude of the laser induced shock and the cavitation induced shock wave were within 3% of each other.

The cavitation collapse was not always pronounced. This was the case with the non-flat geometry shown in Figure 7.5. This waveform shows the laser shock wave at 400 mJ, and the reduced pressure spike of a cavitation collapse. This is likely due to the asymmetric collapse regime of the bubble, seen in the 6 mm convex test in Figure 7.48.

7.1.3 Transducer Characteristics

During the tube tests, abnormally large bubble times were registered with the peak detection algorithm. The waveform of this result, shown in Figure 7.6, clearly shows the reason for the erroneous bubble time. Here it can be seen that the peak detection function found the abnormal peaks which where occasionally larger than the true shock wave peaks.

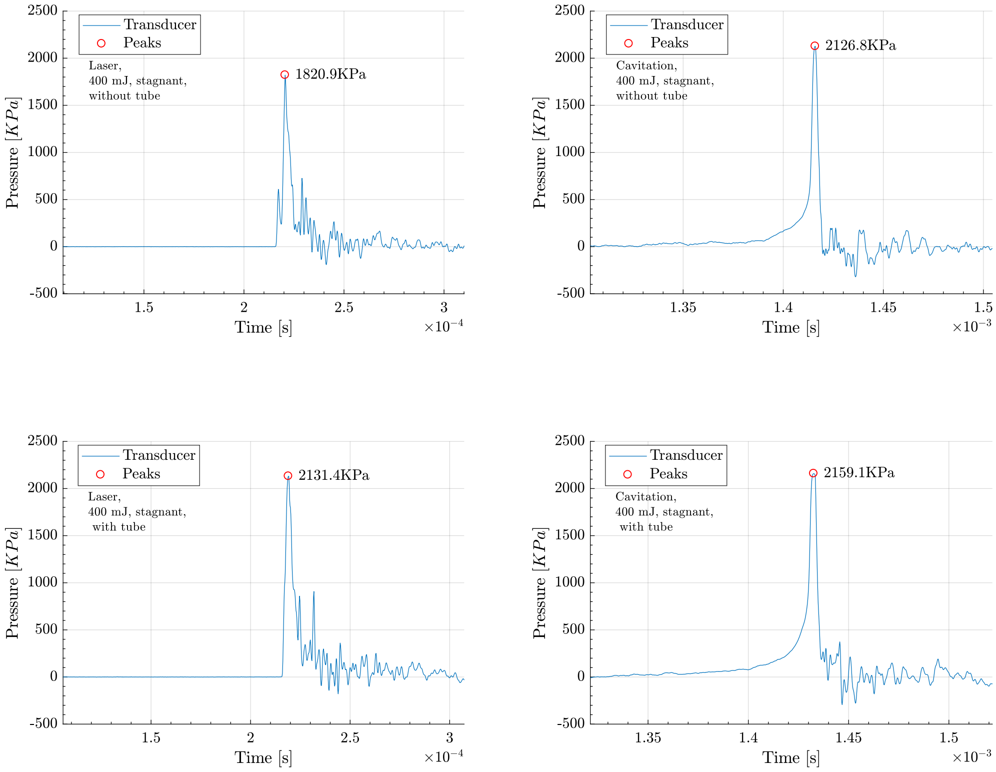

Figure 7.4: Shape of laser induced (left) and cavitation collapse (right) shock waves.

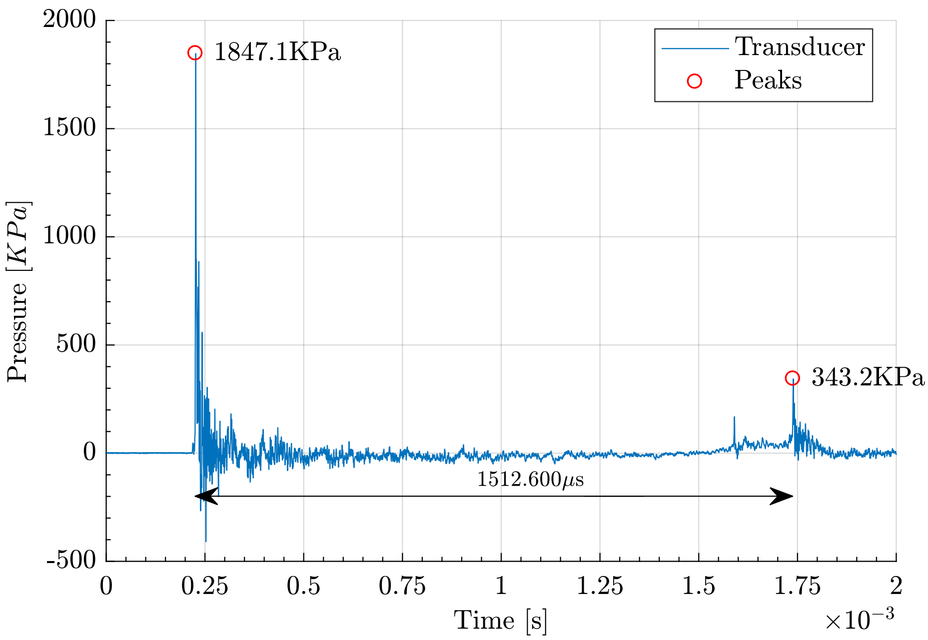

Figure 7.5: Waveform of the 6 mm convex shape near an internal corner clamp.

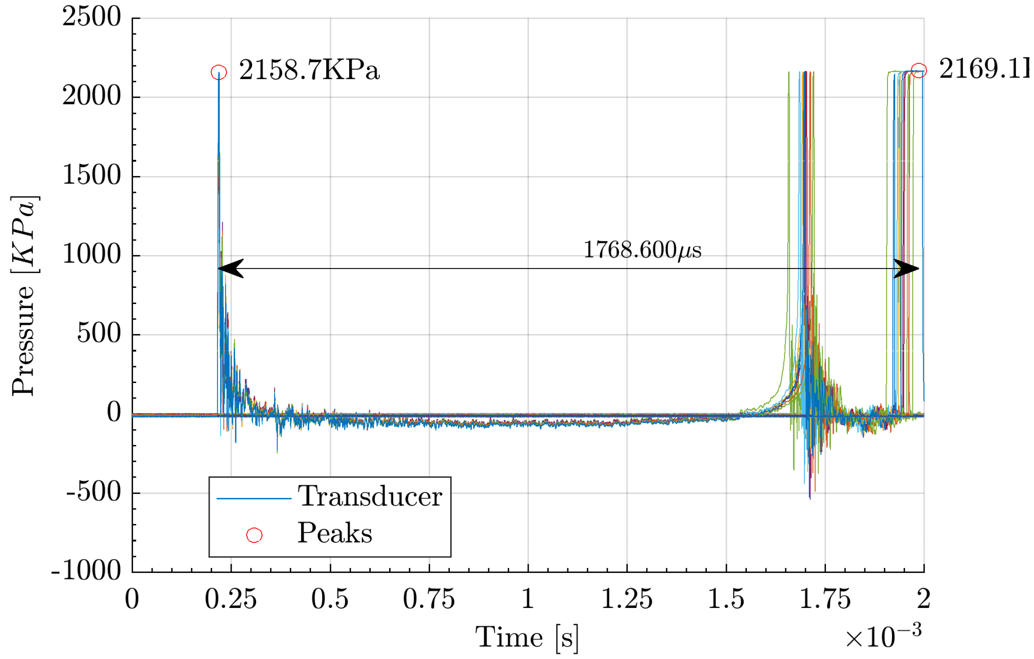

Figure 7.6: Erroneous transducer output.

It is suspected that the transducer was sending erroneous signals. There are three potential reasons for this;

- Water entering the signal conductor cable is most likely as it had been submerged for many hours at a time;
- A failing transducer due to fatigue is possible as the period of service for this particular transducer was more than 20 years;
- Or the transducer was broken due to being excited at its resonant frequency. This is possible as the impulse from the shock wave could have very high frequency components that were not resolved with this transducer.

The first two causes of failure were remedied by replacing the old transducer with a new one and resealing the connection to the signal cable. These erroneous signals were never observed following this intervention.

7.1.4 Transducer Pressure Uncertainty

The response of the transducer was attenuated with a series clipper circuit to around 2130 kPa. This is apparent in all waveforms (including that of the erroneous signal in Figure 7.6 and in Figures 7.6, 7.3). The pressure of 2130 kPa corresponds to a voltage of 7.668 V, which means the voltage was limited prior to the 10 V design limit. Indeed, the selection of these particular Zener diodes in this circuit was too conservative, as they began limiting the voltage early. The result is a waveform that has a flat top, in which its peaks are 'clipped' prematurely. The shape of the clipped waveform is plotted in blue in Figure 7.7. With a flat top, the uncertainty associated with the peak detection is increased due to more points along the flattened waveform falling within the pressure transducer uncertainty of 21.148 kPa (see Table 6.1), any one which could be a suitable peak.

This means that the peak location uncertainty would vary depending on the peak pressure; typically ± 1 data point (200 ns) at pressures below the clipped (near 2000 kPa) value and ± 2 data points (400 ns) at pressures that exceed the clipped value - where the truncation includes more of points. Plotted in Figure 7.7, above an actual waveform, is one potential peak that could have existed if no clipping were present.

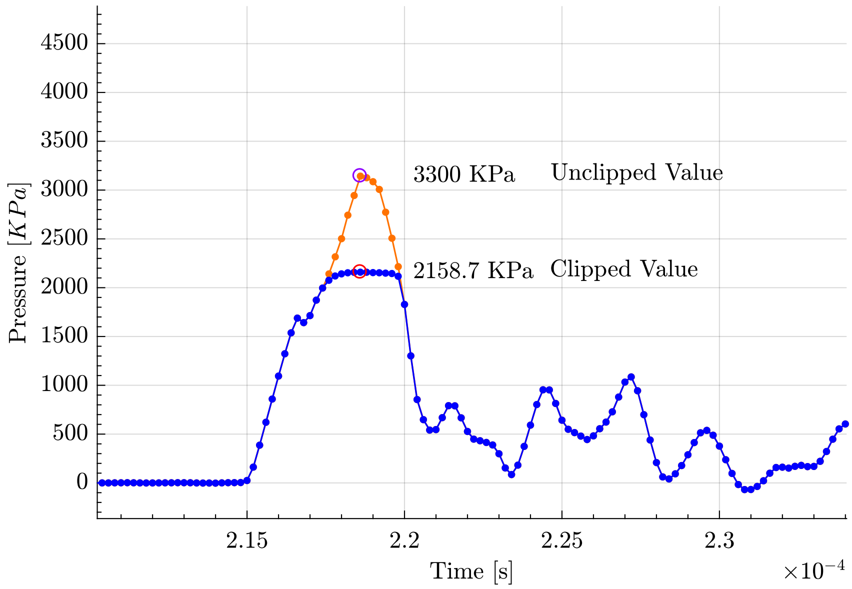

Figure 7.7: Clipped transducer signal with a hypothetical unclipped signal.

In practise, the flattened waveform still showed a diminished but raised hump near the middle of the plateau. Within the peak detection (see Section 6.1), the peak threshold value, that would remove these points, was kept at zero. This means that the peak detection was still successful on such mildly prominent peaks and had a smaller true uncertainty than the full width of the truncated portion. The range of selected shock wave peak locations in Figure 7.8 is 600 ns between the points 219.8 μs and 220.4 μs. It was assumed (but cannot be immediately proven due to bubble variability) that the same error is present on the cavitation bubble collapse shock wave. Therefore transducer-clipper circuit conservatively contributes 1.2 μs to the total uncertainty peak detection measurement.

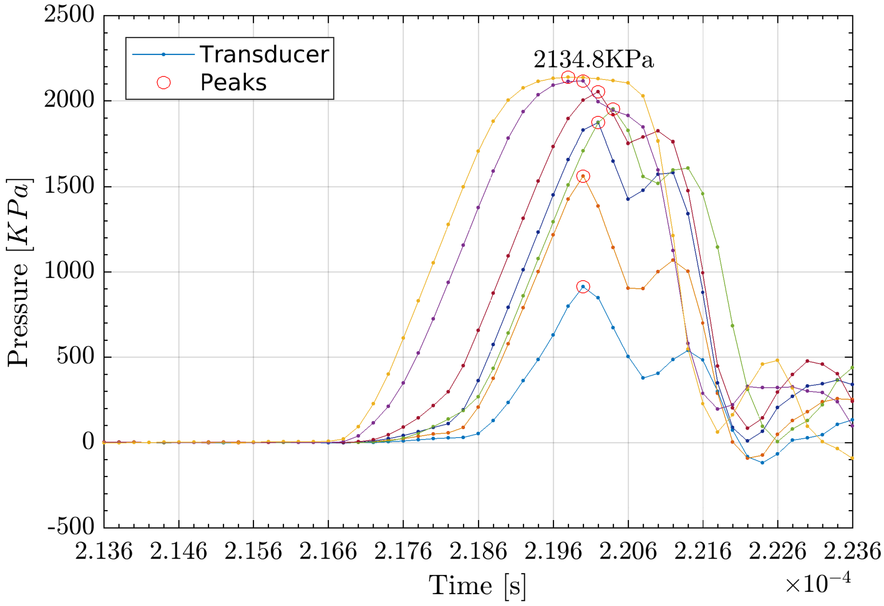

Figure 7.8: Different shock wave peak locations for varying power intensities 2.5 GW/cm^2 to 17 GW/cm^2.

Summary:

- The transducer displayed peaks with high signal to noise ratio making peak detection possible and reliable.
- The rise in pressure for the laser shock wave was much steeper (more rapid) than the cavitation shock wave.
- The design of the clipper limiting circuit was conservative, limiting the volage output to around 7.668 V or corresponding pressure of 2130 kPa.
- The peak values of both laser and cavitation induced shock waves were similar due to the waveform being clipped above 2130 kPa.
- Above an amplitude of 2130 kPa, the uncertainty associated with the peak locations and corresponding bubble time was 400 ns. The conservative peak detection uncertainty is 1.2 μs.
- An erroneous waveform was remedied by replacing the transducer.

7.2 Stagnant Water Tests

Explanation of Experiment

Single laser pulses were fired one by one into a stagnant tank of DI water at least 20 seconds apart to allow for the water to resume stagnant conditions. A laser power intensity of around 13 GW/cm^2 was chosen as it represented the midway point of the system capability. The test section and carbon steel almen strip target is illustrated in Figure 7.9. Test parameters are summarised in Table 7.1.

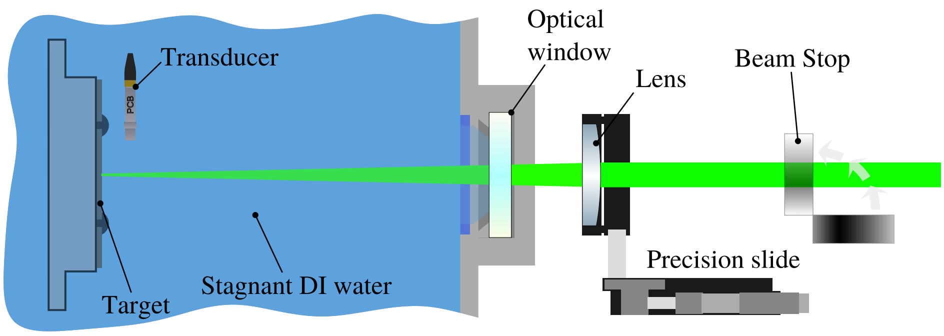

Figure 7.9: Experimental set up of the edge test.

Table 7.1: Stagnant DI water test conditions.

Parameter	Value
PI	13 GW/cm^2
Average Spot Diameter	1.0042 mm
Rep Rate	0.05 Hz
Water conductivity	DI 1.54 μS/cm @ 19.7°C
Water velocity	0 m/s
Target curvature	0 mm (flat almen)

Observations

High speed photography was employed to understand the size and shape of cavitation bubbles with time. Nine frames were chosen to represent the lifetime of the cavitation bubble in Figure 7.10.

A detailed description of each frame is as follows;

Frame 1: The remnants of the laser pulse can be seen in a trail of small bubbles where the beam filled the water. The almost hemispherical cavity is brightly lit from within. The speed of the cavity expansion is shown by the heavily blurred outer edge.

Frame 2: The cavity has convincingly become a bubble, now at least twice as large as the previous frame. There is a ring at the interface of the hemispherical bubble and the metal plate. Motion blur of the bubble wall is present but less pronounced than on frame before. The top of the bubble is covered with tiny bubbles and suspended particles that seem to be carried along as the cavitation below them expands.

Frame 3: The bubble has grown further, but as a slower rate. The ring at the interface of the bubble and the metal has developed into a thicker fillet shape that surrounds the bubble. The small bubbles/particles on the top of the larger cavitation bubble remained near to the surface interface of cavity and water though unattached.

Frame 4: The bubble is even larger now, the expansion has slowed given how much sharper the edges of the bubble appear. The fillet has now become an interface that meets the metal surface perpendicularly. Some of the residual small bubbles have disappeared, others remain close to the cavitation bubble top surface.

Frame 5: This is the maximum size of the cavitation bubble. The walls are in good focus and clearly distinct from the surrounding water. The interface of the bubble and metal is perpendicular. Nearest to the interface, the wall of the bubble appears to be more cylindrical than spherical.

Frame 6: The bubble has shrunk slightly. The rate at which the bubble is shrinking is not yet fast enough to cause significant motion blur of the bubble edge. The bubble-metal interface is now slightly bowed toward the centre, now more conical. The height of this cone is around 25% of the bubble height.

Frame 7: The bubble is rapidly shrinking, shown by the obvious motion blur of the bubble wall and small particles. The visible streaks of the suspended particles are directed towards the centre of the bubble indicating the motion of the water around the bubble. A curved shadow appears to lag behind the now rapidly moving outer edge of the bubble.

Frame 8: The speed at which the bubble is collapsing is shown in the highly blurred edges of the bubble and particle streaks that are directed to the centre. The lagging shadow remains apparent though less pronounced than in previous frames.

Frame 9: The bubble shape is no longer apparent. In its place, a dense cloud on the surface of the metal is obvious. Small bubbles have reappeared in the beam path and surrounding water, representing the passing of a second shock wave.

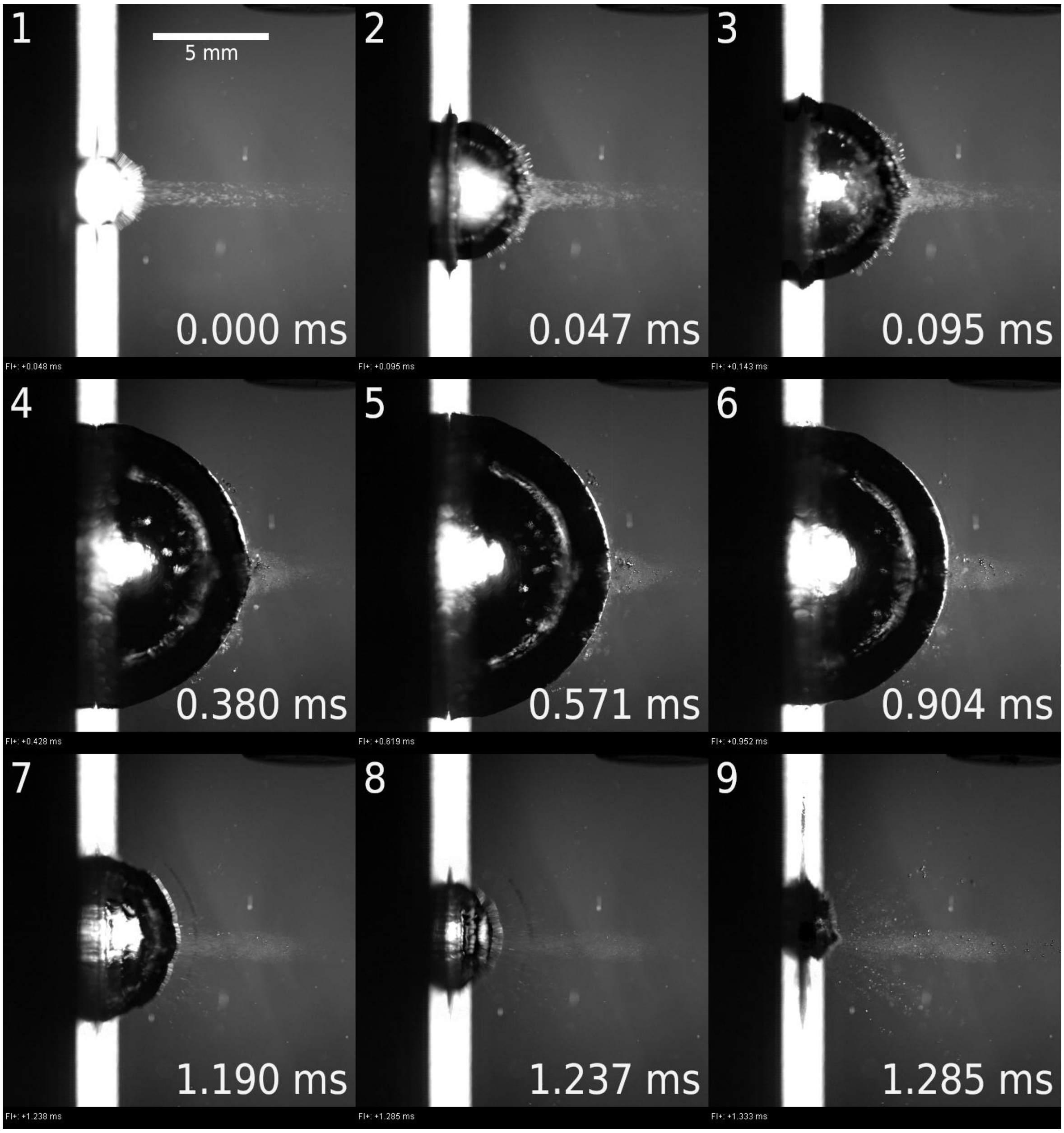

Figure 7.10: Life time of a cavitation bubble produced by a $13\,\mathrm{GW/cm^2}$ laser pulse in DI water.

The life time of a cavitation bubble in tap water is shown in Figure 7.11. Many features are similar to that in Figure 7.10; the bubble displayed rapid growth slowing toward maximum radius and then rapid collapse, there is a ring at the interface of the metal and bubble which tended to change shape between expansion and contraction of the bubble and a faint shadow band also appeared here that followed the top edge of the bubble in a curved shape.

In comparison to the bubble shape illustrated in Figure 2.11, the bubble seen in Figures 7.11 and 7.10 displayed a greater attachment to the surface of the target material with the 'bottom diameter' being equal to the 'maximum diameter'. While there may be a toroidal flow and jet that was directed to the surface, these features were not apparent due to the limited frame rate in this study.

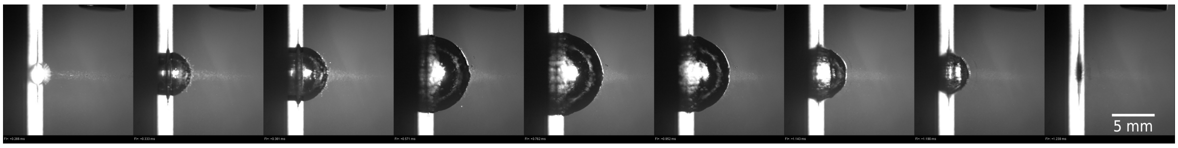

Figure 7.11: 13 GW/cm^2 bubble in tap water.

The size of the cavitation bubbles is shown in Figure 7.12. The 'zero' size of the cavitation bubbles were never observed, but inferred here at the frame when the bubble edge was no longer perceivable. The diameter of the bubble in the vicinity of a tube, shown in Figure 7.13, was marginally larger than without a tube nearby. Both tap water tests produced significantly smaller bubbles than those in the deionised water.

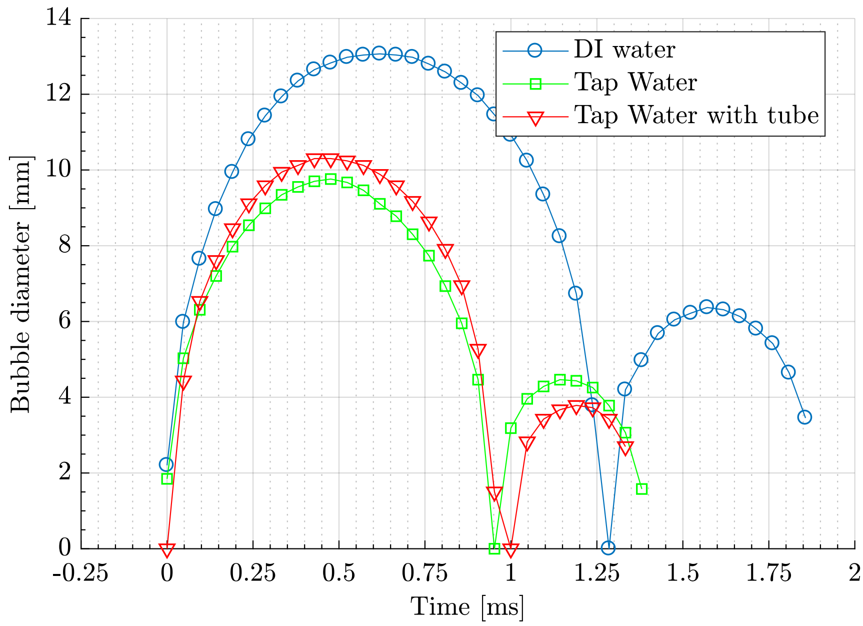

Figure 7.12: Bubble size for a 13 GW/cm^2 laser pulse in DI and tap water.

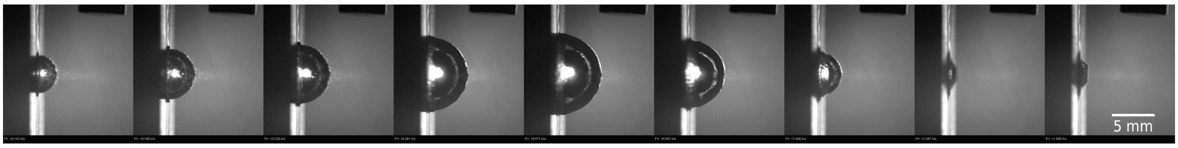

Figure 7.13: 13 GW/cm^2 bubble in tap water with 40 mm tube surrounding the beam.

Discussion

The bubble growth and collapse in Figure 7.10 is clearly visible with good optical clarity, confirming that conditions and methods used are photographically suitable. The exposure time of 47 μs allows for motion within that time to be seen albeit as a blurred image. This exposure time also allows for subtle features to be seen such what is suspected to be an expansion rarefaction in Figure 7.14.

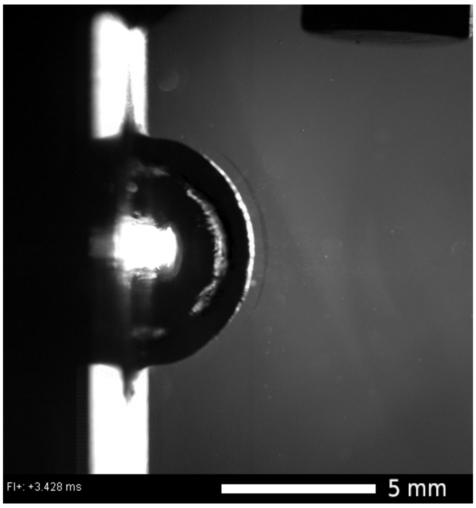

Figure 7.14: Suspected expansion wave upon bubble collapse. 13 GW/cm^2 laser pulse.

Bubble time

The difference between tap and deionised water is apparent in Figure 7.12. The bubble size obtained with high speed imagery clearly indicates the rate of growth as well as the maximum bubble diameter. The beginning and bubble diameter and the end bubble diameter are known to be zero and near zero respectively. Given the fixed and comparatively slow frame rate of the high speed camera however, these points were very seldom captured in the footage. As an initial analysis, the minimum bubble diameter was assumed to be within the exposure of the frame that shows no measurable bubble diameter.

The difference in maximum diameters of the tap water tests with a tube and without is small but apparent. While the presence of the tube was thought to have made a noticeable difference, in this case the change could be attributed to the tests being done on different days.

Breakdown

When timed correctly, the first frame of the high speed footage in Figures 7.15 to 7.16 allows break down nucleation sites to be illuminated. The breakdown in the laser path observed in deionised water had noticeably fewer vapour bubbles that remained after the laser pulse than that of the tap water.

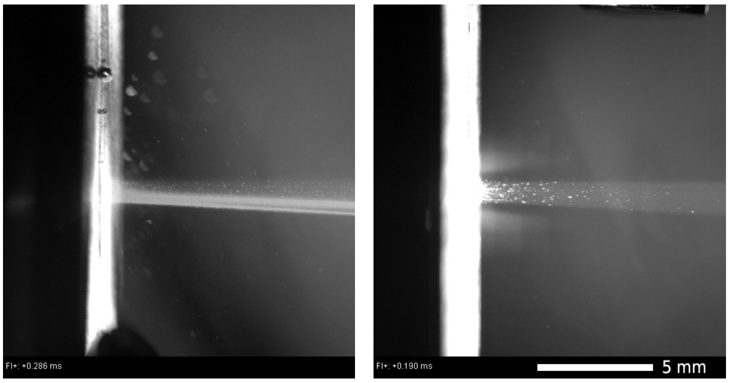

Figure 7.15: Laser irradiation in deionised water 19 GW/cm^2 and 1.9 GW/cm^2.

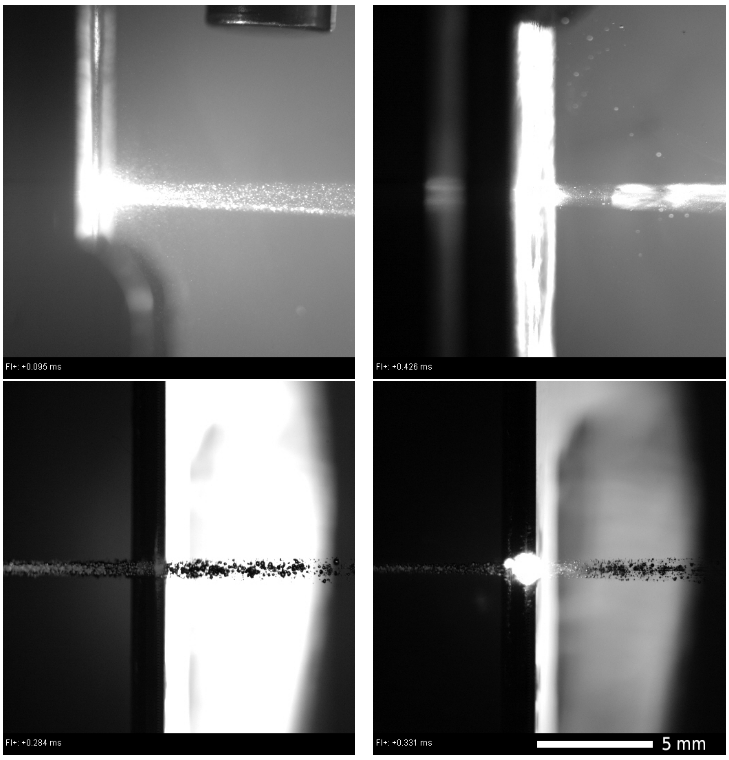

Figure 7.16: Laser irradiation in tap water Top: 12 GW/cm^2 and 4.0 GW/cm^2. Bottom: beam off a plate edge 0.047 ms after pulse at 8.3 GW/cm^2.

Ablation Residue

Within these submerged water tests, the residual cloud that remains in proximity to the target after the bubble has dissipated is of unknown composition. It is likely to be a mixture of metal particulates that were liberated from the target during ablation as well as gaseous micro bubbles. Figure 7.17 shows that this cloud from a previous shot is a hindrance to subsequent laser energy delivery because it (1) is optically blocking the beam path and (2) is a nucleation site for direct ionisation (2.2), promoting dielectric breakdown, which results in highly absorbent plasma.

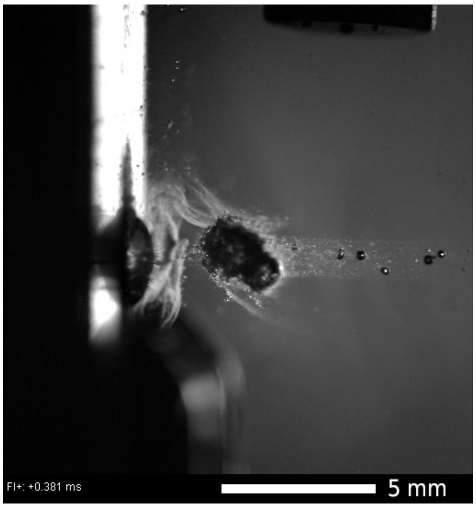

Figure 7.17: Water breakdown at 13 GW/cm^2 0.047 ms after laser irradiation.

Summary:

- Laser exposure on the target surface under stagnant conditions produced a hemispherical bubble that remains attached to the surface during growth and collapse.
- The maximum bubble size in deionised water was significantly larger than that of tap water for the same laser output energy.
- Dielectric breakdown of the water left more bubbles in the beam path in tap water than in deionised water.
- Residual products of ablation hindered the next laser pulse in a stagnant tank.

7.3 Effect of Repetition Rate and Laser Energy on Cavitation Bubbles

Explanation of Experiment

In the first part of this experiment, a carbon steel almen strip target was submerged in a full tank of DI water (11 litres) and received laser pulses fired at 1 Hz with varying energies. The pressure information was recorded for every shot and the bubble period was then obtained. In the second part, energy was varied and the repetition rate of the laser was varied in intervals of 1 Hz, 2 Hz, 5 Hz and 10 Hz. In both tests, the very first shot fired was done so in completely stagnant conditions, that is with no movement of water or any disturbances in the beam path. A summary of the experimental test parameters is found in Table 7.2.

Table 7.2: Repetition rate test parameters.

Parameter	Value
PI	8.3 GW/cm^2
Average Spot Diameter	1.0138 mm
Rep Rate	1-10 Hz
Water conductivity	DI 2.59 μS/cm @ 19°C
Water velocity	0 m/s
Target curvature	0 mm (flat almen)

Observations

As can be observed from the sequential plot in Figure 7.18, the first shot was always greater than the second shot, regardless of power intensity. This was interpreted as difference with a positive value. In order to simply account for all the subsequent shots, an average value was used, expressed in Equation 7.1.

$$\% \; difference \; from \; first = \frac{\left(T_1 - \frac{\sum_{i=2}^{n} T_i}{n-1}\right)}{T_1} \times 100 \tag{7.1}$$

To understand this difference between the first shot and an average of the subsequent shots, the magnitude of difference is plotted in Figure 7.19.

The drop in bubble lifetime from the first bubble to the average value of the rest appeared to be directly proportional to laser power intensity until a peak at 13 GW/cm^2.
Thereafter, the trend dipped at 17 GW/cm^2.

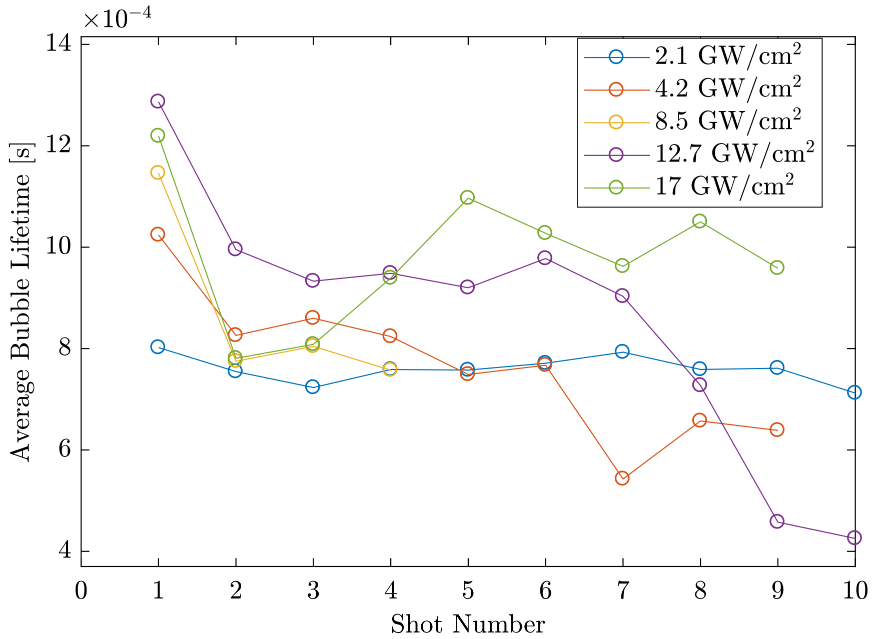

Figure 7.18: Line graph showing bubble lifetime per shot number for various energy levels in stagnant DI water at 1 Hz.

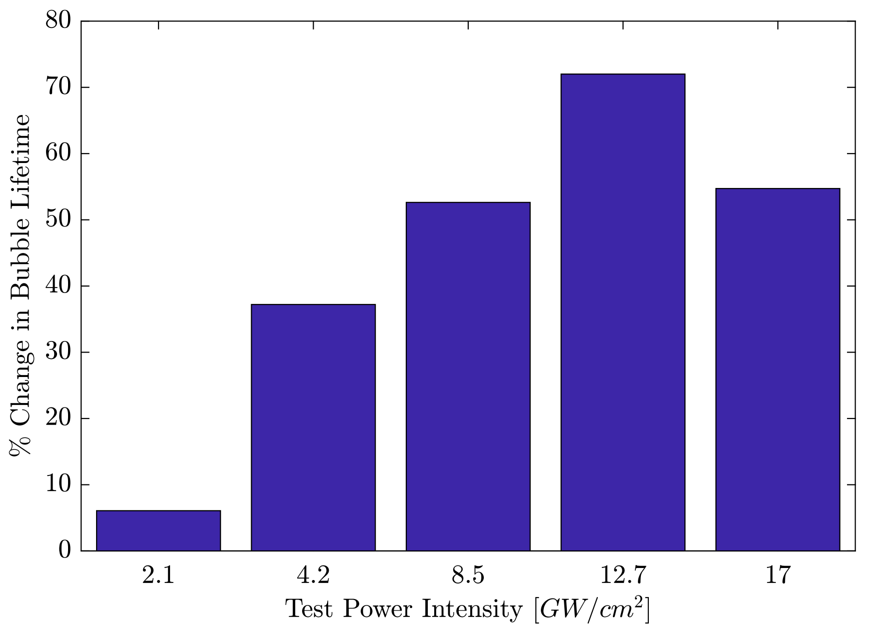

Figure 7.19: Bar graph showing percentage difference in bubble lifetime between the first shot and the average of all subsequent shots at laser energies at 1 Hz.

Figure 7.20 shows a summary of the difference between the first and subsequent average bubble lifetimes at four different repetition rates: 1, 2, 5 and 10 Hz. At each repetition rate, power intensities were set to 2.2 GW/cm^2, 4.5 GW/cm^2, 9.3 GW/cm^2, 13 GW/cm^2, 17 GW/cm^2. These are with a 1 mm spot size at approximate energy levels of 100 mJ, 200 mJ, 400 mJ and 800 mJ respectively.

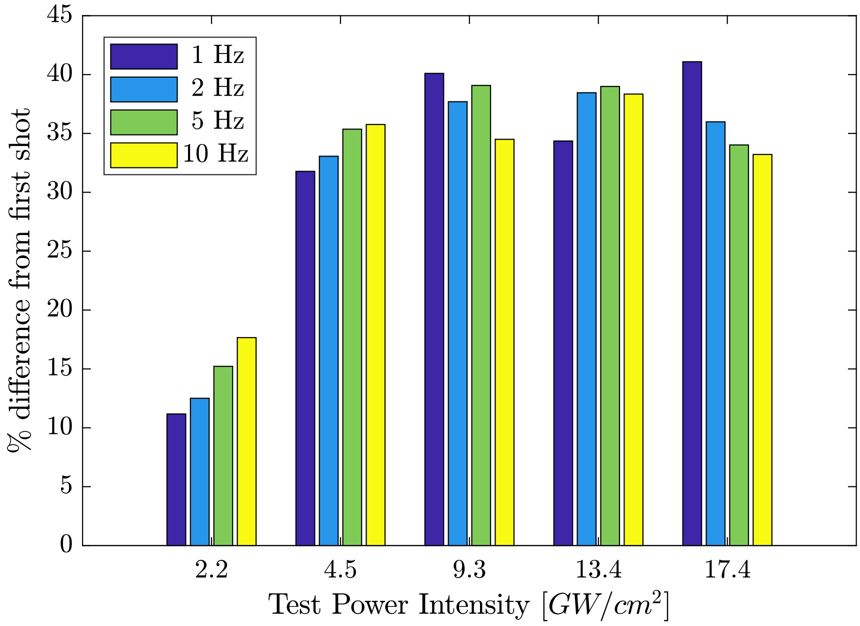

Figure 7.20: Bar graph showing difference in bubble lifetime between the first shot and the average of all subsequent shots for varying repetition rates.

Discussion

Energy variation test at 1 Hz

A drop in bubble lifetime as a result of less laser energy reaching the target in newly-disturbed water conditions is to be expected. In the case of submerged laser peening, the beam loss is associated with breakdown and blockages (such as bubbles) along the laser beam path. If this loss factor is dependent on the energy of the beam, then it is logical to assume an increase in beam energy will lead to an increase in beam loss. By this, it is reasonable to say that the increase in bubble lifetime difference could be attributed to the break down losses rather than any constant (or even spurious) beam blockages. It should be noted however, that breakdown was significantly enhanced both by any parameters that change the dielectric strength of the water as well as particulates (observed to be suspended in the water) and air inclusions (tiny bubbles) that act as nucleation sites within the water.

From the results in Figure 7.19, after the local maximum of 13 GW/cm^2, the difference in bubble lifetimes showed a possibility of saturation.

Energy variation test at 1 to 10 Hz

The second test was a follow up of the first, making use of different laser repetition rates. It was expected that the increase in repetition rate would result in a reduction of bubble lifetime because the LSP process inherently disturbs the clear stagnant water conditions.

All stagnant water tests had a positive difference in bubble time between the first and subsequent shots, shown in values above the X-axis in Figures 7.20, 7.19. This means the conditions that demonstrate the greatest laser energy transfer were those of the first shot i.e. clear stagnant conditions. The longer the time duration between the first and second (or subsequent) shots, the clearer and more stagnant the conditions within the tank became by diffusion or particles settling. This was apparent at 2.2 GW/cm^2, with an increasing trend that shows the higher the repetition rate, the greater the difference in bubble lifetime from the first shot. Within higher power intensities in Figure 7.20, the trend was less clear, but followed an increase until signs of saturation occurred at either 9.3 GW/cm^2 or 13 GW/cm^2. Interestingly within the 17 GW/cm^2 test the trend appeared to invert, that is for higher repetition rates, the difference in bubble time diminished.

Summary:

- The first laser shot fired in stagnant conditions always produced the largest cavitation bubble.
- On average, the bubble time difference and corresponding laser energy loss increased after first shot with higher power intensities. The increasing trend appeared to saturate at a power intensity of around 9.3 GW/cm^2.

7.4 Effect of Test Duration

Explanation of Experiment

In this experiment, a carbon steel almen strip target was submerged in tap water with an aquarium pump clearing the beam path and recirculating the water within the same tank. This is illustrated by the arrows in Figure 7.21. The laser was fired at an average power intensity of 18 GW/cm^2 at 10 Hz at the target for 11 minutes. The target mount was moved with a high coverage pattern covering 5 mm × 60 mm on the almen strip. The parameters in this test are summarised in Table 7.3.

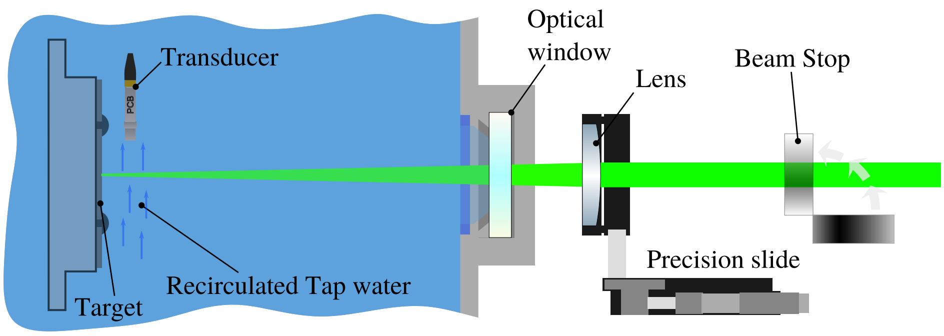

Figure 7.21: Experimental set up of the edge test.

Table 7.3: Paramaters for the duration test.

Parameter	Value
PI	18 GW/cm^2
Average Spot Diameter	1.004 mm
Rep Rate	10 Hz
Water conductivity	211.4 μS/cm @ 26.1°C to 211.6 μS/cm @ 25.6 °C
Water velocity	$>$ 0 m/s (unknown, but rapidly moving)
Target curvature	0 mm (flat almen)

Observations

After every minute, 20 shots were recorded. The average bubble lifetime and measurement uncertainty bars for eleven of these minutes are plotted in Figure 7.22, both of which reduce with time. It should be noted that although only a sample of 20 measurements were obtained at each passing minute mark, the laser was firing continuously, peening the surface of the almen strip at 10 Hz. This means that cumulatively 6600 shots were fired into the metal surface in the same tank of water. The bubble lifetime diminished by 0.17590 ms or 23.57% over the eleven minutes. Water conductivity was recorded before and after the full test. The dashed line represents the change in water conductivity, a 0.0946% increase.

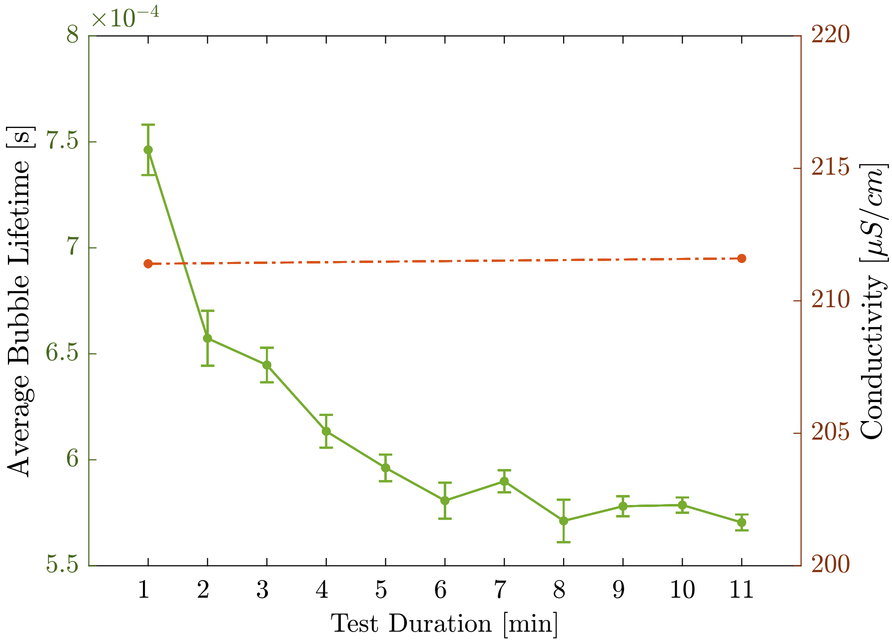

Figure 7.22: Average bubble life time and water conductivity over the long duration test, error bars represent the measurement uncertainty for an average of 20 pulses.

Discussion

Since all previous tests that make use of a laser repetition rate of 10 Hz showed a drop in bubble time, the perceivable drop that occurred in the first two minutes was expected. The larger measurement uncertainty of the first and second minutes is unsurprising, since the average bubble time diminished so rapidly from the first shot as observed in Figure 7.18.
The magnitude of standard uncertainties tended to reduce overall as the test progressed. This reduction in dispersion, along with a nearly unchanging average, indicates a rough stability was present after 8 minutes.

It was initially thought that the metal vapour liberated from the high intensity peening would increase the concentration of particulates in the tap water. Impurities in the water may lower the dielectric breakdown threshold of water [41], which would lead to a reduction in delivered energy and thus observable bubble time.

While the average bubble lifetime did reduce significantly, the average water conductivity in this test did not change significantly (211.4 μS/cm to 211.6 μS/cm), and could be easily fall in the range of the device uncertainty of 1.0570 μS/cm for this range, which means essentially constant conductivity [71]. Yet, the bubble lifetime and inferred laser delivery clearly underwent a reduction over time. This suggests that, within this tank, the average conductivity alone did not represent the efficacy of laser energy delivery in water.

As is shown in the high speed photography (such as in Figure 7.10), it can be seen that small bubbles were present on the surface of the large cavitation bubble. These tiny gas bubbles may not have affected the conductivity of the water at large, yet could still have acted as a nucleation site for breakdown, and as such could have changed the dielectric strength of the water, if present in the beam path. The same may be true for the metal particulates, in low enough concentration.

With this understanding, the gas within the tap water (either whole bubbles or dissolved air that comes out of solution) and metal particulates could both be the dominant reasons for the reduction in delivered laser energy within this experiment, rather than conductive ions in solution.

Summary:

- After eleven minutes of LSP at a high power intensity and high repetition rate, the average bubble lifetime diminished by 23.57%, indicating a diminishing beam delivery to the target surface.
- The water conductivity within the tank increased by 0.0946% over the duration of the test, which was within the uncertainty of the conductivity measurement. This means conductivity was essentially constant.
- Small gaseous vapour bubbles within the water surrounding the cavitation event were present in every test, and were thought to be the primary contributors to the reduction in delivered beam energy.
- It is currently unclear whether the conductivity was an insensitive indicator of likely dielectric breakdown in this experiment or if a poor measurement of conductivity was recorded altogether.

7.5 Tests in Tap Water

Explanation of Experiment

In order to better understand the response of a LSP system in stagnant tap water, three tests were conducted. All three tests used a carbon steel almen strip target, seen in Figure 7.23, in open water. Each shot was fired at least 20 seconds after the previous shot, allowing for stagnant conditions to return between. The first test, "Test 1" was a control test, filled from a dry tank. DI water was used to rinse the tank before "Test 2" and "Test 3" tests to ensure no residual solutes were present in the tank. The water conductivity did not vary beyond 1.2% of the average value shown here. A summary of the test parameters is found in Table 7.4.

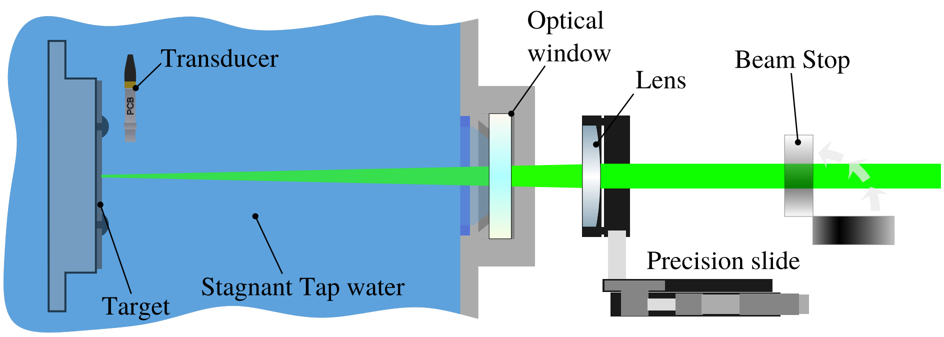

Figure 7.23: Experimental set up of the stagnant tap water tests.

Table 7.4: Stagnant tap water test parameters.

Parameter	Value
PI	2.1 - 17 GW/cm^2
Average Spot Diameter	0.996 mm
Rep Rate	0.05 Hz
Water conductivity	Tap 202.1 μS/cm @ 24°C
Water velocity	0 m/s
Target curvature	0 mm (flat almen)

Observations

Three stagnant tests were performed in tap water and is plotted in Figure 7.24.

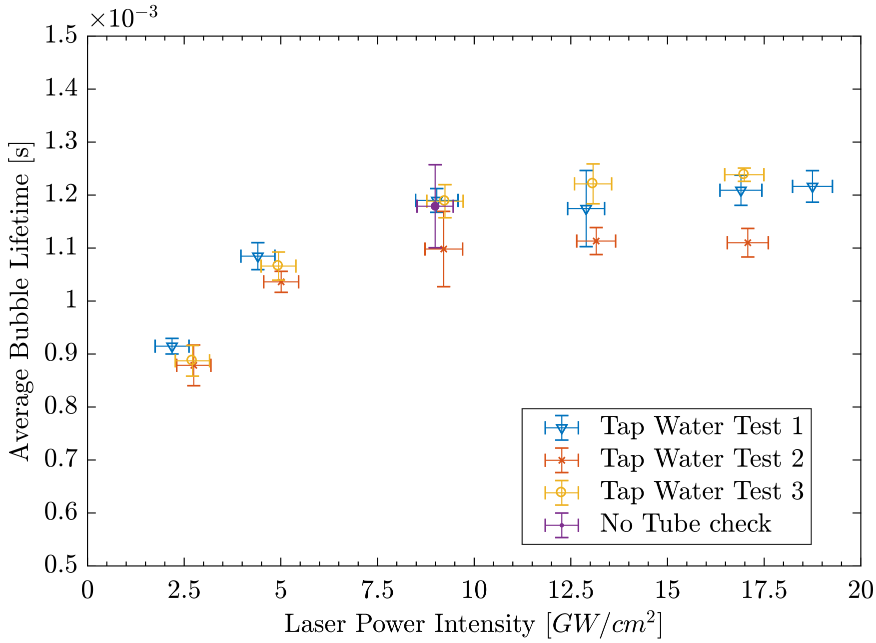

Figure 7.24: Each point represents the average bubble lifetime of at least six shots with measurement uncertainty bars for stagnant tap water conditions. No Tube check is plotted for comparison with the following section.

Each of the three tests displayed an increasing bubble lifetime with an increase in laser energy. It is characterised by a steep and seemingly proportional increase from 2.5 $\mathrm{GW/cm^2}$ to 10 $\mathrm{GW/cm^2}$ after which the increase is either shallow or unreliable. This compares well to the plots seen in Figures 2.19b where the predictability of the data diminishes at a certain laser power intensity.

The apparent saturation of the bubble lifetime in Figure 7.24 is also at a similar point to that seen in Figure 7.19 - at a laser power intensity of between 8.5 $\mathrm{GW/cm^2}$ and 13 $\mathrm{GW/cm^2}$. This is distinguishable in two ways. The first is the flattening average bubble lifetime with increasing laser energy, that is a shallow or negative gradient between two average points. The second is by observing the measurement uncertainty, plotted on each point with vertical error bars. The unstable plasma breakdown events introduce a greater overall stochastic variation in the results. In each test there is a point or power intensity at which the magnitude of the measurement uncertainty appeared to increase more rapidly than before. This point may be taken as the beginning of the system saturation. This means that the 'knee' or saturation point is an important indicator to the stability of the process. Points that have a lower laser input than this point exhibited greater stability than points with a higher laser energy input.

Since the conditions for this test are within stagnant water, the assumptions of constant static pressure are applicable and could be used to estimate the bubble energies for each power intensity. The bubble energy estimates for this test is given in Figure 7.25.

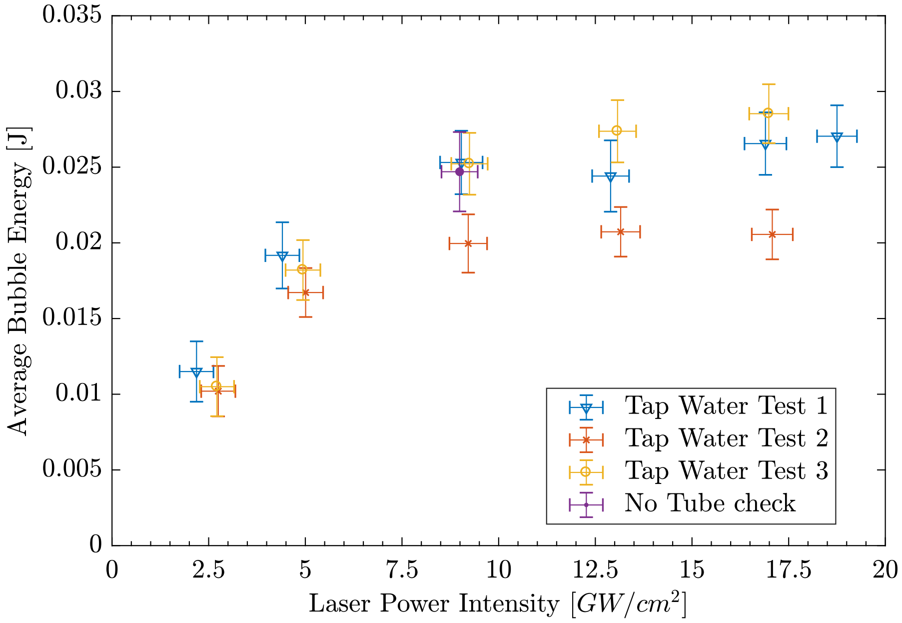

Figure 7.25: The average bubble energy of at least six shots per point for stagnant tap water conditions. Error bars denote the uncertainty associated with each average.

Summary:

- The point at which the system began to saturate appeared to be associated with the point with greatest variance in stagnant water.
- The saturation point appeared to be an important indicator of the laser cavitation bubble system predictability.

7.6 Tests in a Tube of Water

A test to quantify the effect of a 50 mm (40 mm bore), 145 mm long, acrylic tube in stagnant water was performed. This tube, in Figure 7.26, was fully filled with stagnant water ensuring no air bubbles. The power intensity was increased from 2.2 GW/cm^2 to around 17 GW/cm^2. A benchmark test without the tube was performed at 8.6 GW/cm^2. The test summary is found in Table 7.5.

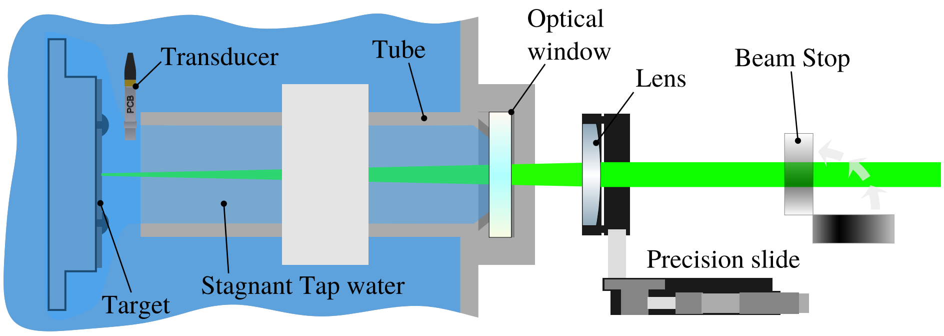

Figure 7.26: Experimental set up of the stagnant tap water tests within a tube.

The effect of the tube on the same day is illustrated in Figure 7.27. The point measured without the tube (in open water) is plotted here with a • marker. The comparable point ▽ within the tube, had a slightly higher average bubble lifetime, closely falling within the measurement uncertainty of the open water bubble lifetime, if extrapolated to the exact same laser energy. Thus, the effect of a 40 mm diameter tube was found to increase the bubble time, though not beyond the measurement uncertainty of the test without the tube.

Table 7.5: Initial tube test parameters

Parameter	Value
PI	2.2 - 17 GW/cm^2
Average Spot Diameter	0.992 mm
Rep Rate	0.05 Hz
Water conductivity	Tap 201.6 μS/cm @ 23.9°C
Water velocity	0 m/s
Target curvature	0 mm (flat almen)

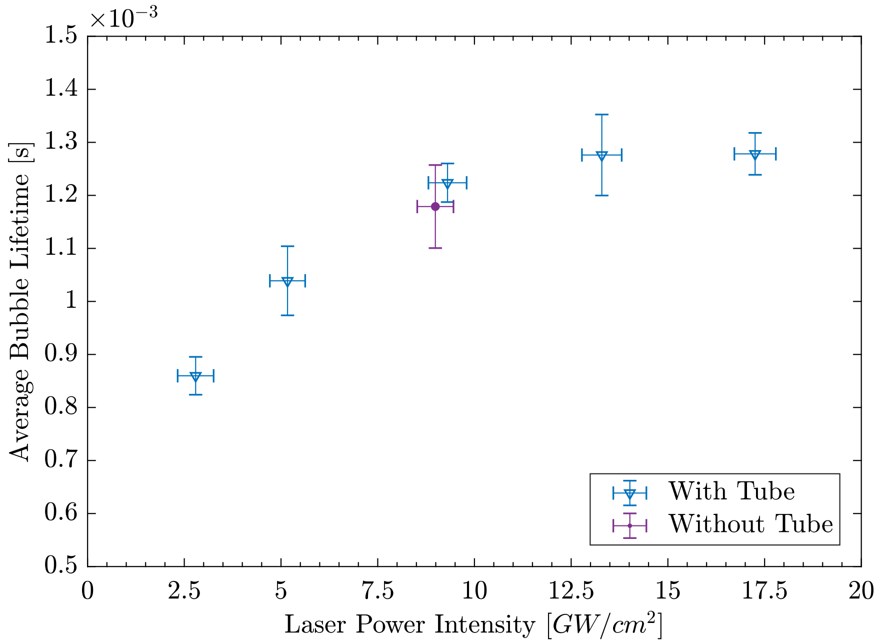

Figure 7.27: Stagnant tap water tests, each point showing an average and measurement uncertainty bars of 10 single shots.

Observing the standard uncertainties, this measure of dispersion displays no apparent sudden increase in this plot. The point of saturation appeared to be around 14 GW/cm^2, where the average bubble lifetime does not increase significantly.

7.6.1 Flow at Low Repetition Rates

With the tube in the same position as before, water was then allowed to flow through the tube to impinge on the target surface, all submerged underwater. The direction of the flow is shown with arrows in Figure 7.28 with test parameters outlined in Table 7.6.

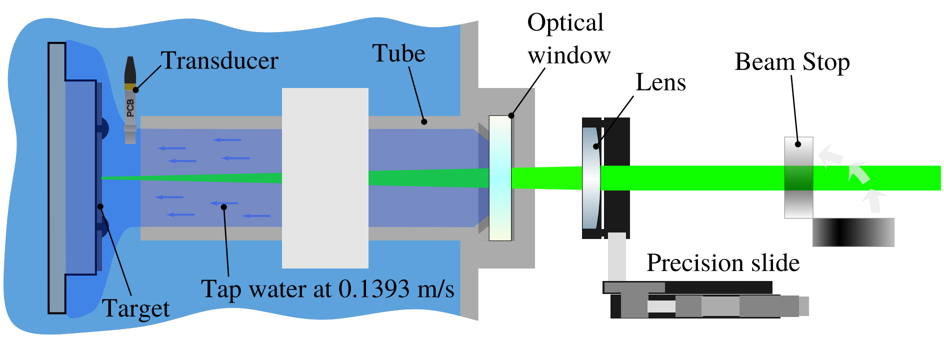

Figure 7.28: Experimental set up of the flowing tap water tests.

Table 7.6: Flowing water test conditions.

Parameter	Value
PI	2.3 - 18 GW/cm^2
Average Spot Diameter	0.971 mm
Rep Rate	0.05 Hz, 1 Hz
Water conductivity	Tap 200 $\mu S/cm$ @ 24.8°C
Water velocity	0.139 m/s
Target curvature	0 mm (flat almen)

To illustrate the data distribution, a scatter plot of the single bubble lifetimes and laser shock magnitudes is shown in Figure 7.29. The shock magnitudes are the highest points on the first peak found within the peak detection stage.

A good sanity check may be to compare the saturation behaviour of the laser induced shock wave strength and that of the cavitation bubble lifetime, both being indicative of the energy arriving at the metal surface. As the shock wave pressures in Figure 7.29 indicate however, the comparison is no longer useful above 7 GW/cm^2, as the pressure values appear tied to a maximum, while the bubble lifetime values continue to rise. The pressure limit was likely enforced by the clipper attenuation circuit, successfully limiting the voltage recorded by the DAQ input card.

Figure 7.30 shows the average bubble lifetime for varying laser energies at two repetition rates. The data points $*$ display laser exposures done once every 20 seconds (0.05 Hz) with the • points showing that which was fired once per second (1 Hz). It is clear that the flowing tests at 1 Hz produced on average a slightly larger (3.49% bigger) bubble than flowing tests at 0.05 Hz. This occurred at all energy levels.

The stability of the data points in this flow test is noteworthy. At both 1 Hz and 0.05 Hz, each average data point had consistently smaller (31.79% less in the 0.05 Hz an 74.74% less in the 1 Hz) measurement uncertainty magnitudes than the stagnant water tests, see prior in Figure 7.27. The average bubble time in the flowing tests compared to the stagnant test increased by 4.58% and 8.22% for 0.05 Hz and 1 Hz respectively.

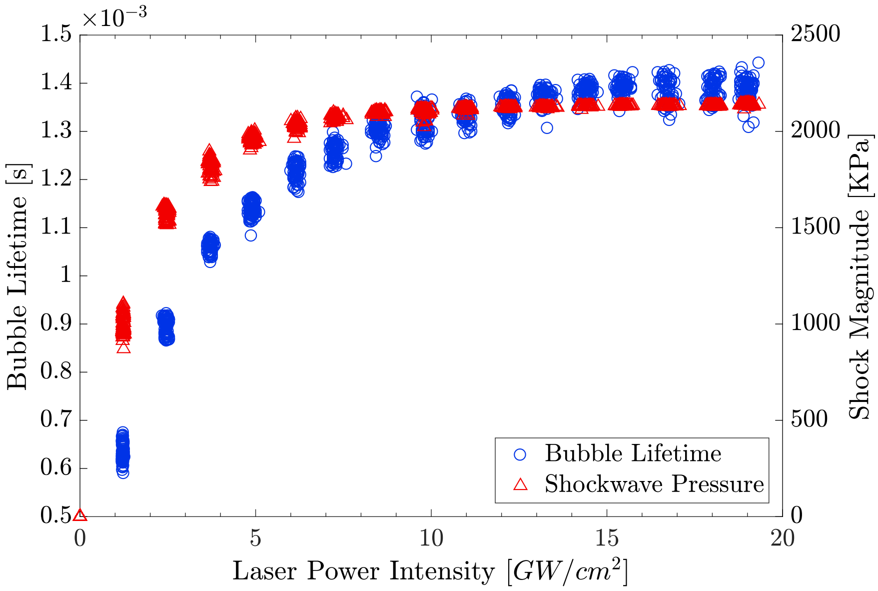

Figure 7.29: Raw data scatter plot of the bubble times in blue and first shock magnitudes in red. Each laser pulse is fired at 1 Hz.

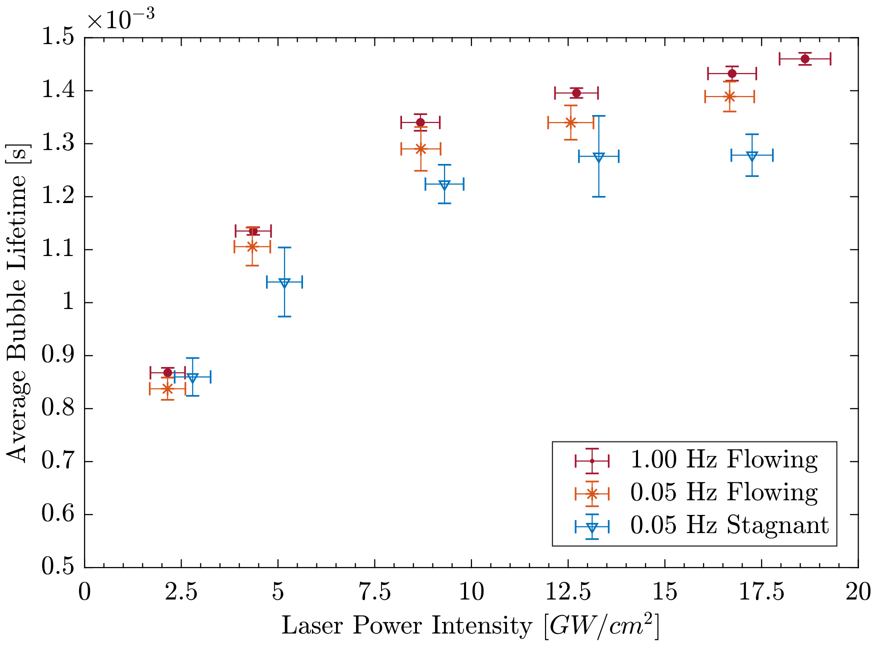

Figure 7.30: Flowing tap water tests at two repetition rates and the previous stagnant water test. Each point showing an average of 10 shots at 0.05 Hz and 29 shots at 1 Hz plot along with their measurement uncertainty bars.

7.6.2 Further Flow Tests

Further tests presented here were conducted to confirm the relationship between delivered laser energy and bubble lifetime in a flowing water stream. The target in Figure 7.31 was a large, flat 304 stainless steel plate 1.5 mm thick submerged in the stream of flowing water.

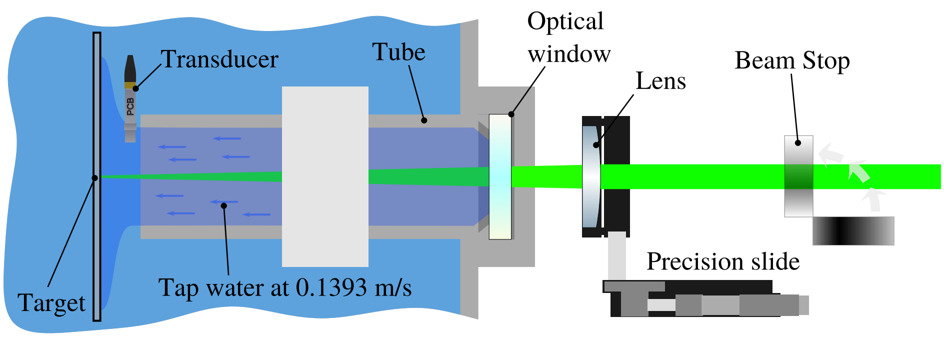

Figure 7.31: Experimental set up of the flowing tap water tests on a large flat plate target.

These results are summarised in Figure 7.32 where each data point is an average of a minimum of 10 and maximum of 110 shots. The uncertainties are omitted for clarity. These were done at 1 Hz (◇,○) and 2 Hz (□) with a large 40 mm internal diameter tube delivering 10.5 l/min of tap water along the beam path. A stagnant test (+) within a tube (from Figure 7.27) is included to illustrate the effect of the flow. Also included are the points ∗ from aforementioned 0.05 Hz test (Figure 7.30) on a carbon steel almen strip, which is a different material.

Table 7.7: Details of multiple tests done in water flow and increasing power intensity.

Parameter	○ & □	◇
PI	1.2 - 19 GW/cm^2	1.2 -18 GW/cm^2
Average Spot Diameter	0.928 mm	0.942 mm
Rep Rate	1 & 2 Hz	1 Hz
Water conductivity	Tap 200.52 μS/cm @ 25 °C	Tap 200.6 μS/cm @ 24.3 °C
Water velocity	0.139 m/s	0.139 m/s
Target curvature	0 mm (flat plate)	0 mm (flat plate)

The effect of a different material (spring steel almen strip and stainless steel plate) produced comparable bubble times in Figure 7.32. A fitted two term exponential curve is plotted alongside the data points. The equation for this curve and constants used are shown below the curve.

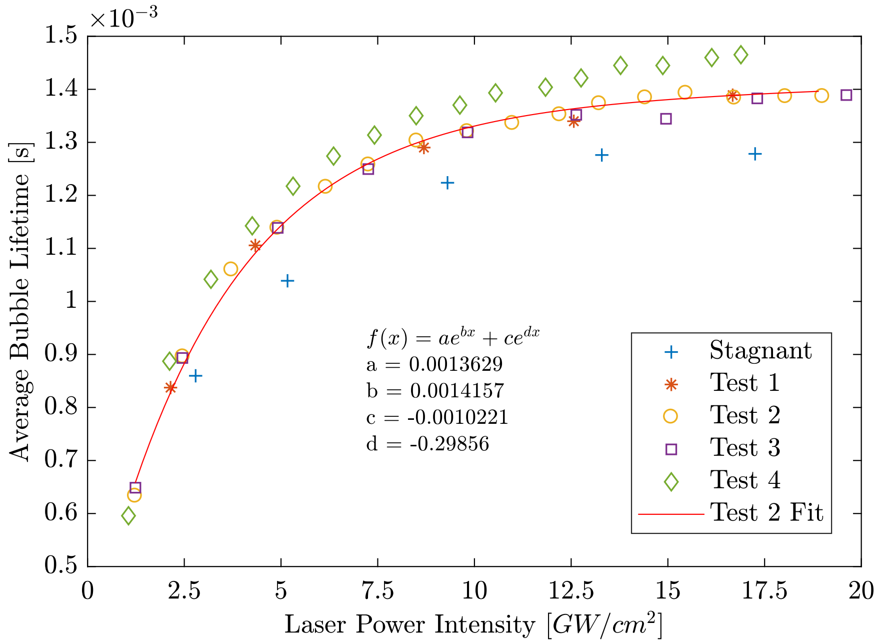

Figure 7.32: Summary of various tests done with water flowing along the beam path.

The averaged test results from Test 2 were used in the least squares interpolation of the curve as it had the greatest number of data points. This type of equation was chosen as it adequately represents the near-asymptotic behaviour of the data, that is tending to a saturated value.

There are three potential causes for the apparent upward shift in bubble lifetime from stagnant to flowing tests; (a) the target geometry in the flowing test was different to that in the stagnant test, (b) the flow might have been clearing the beam path effectively, allowing for greater laser energy transmission through the water, (c) the flowing fluid may have caused a non uniform pressure field, potentially lowering the local static pressure around the bubble.

7.6.3 Process Control Chart

An important tool for assessing whether or not a process is considered in or out of control is a process control chart, illustrated in Figure 7.33. In addition, this chart will show the stability of the measurements over time giving rise to an important understanding of process capability [78].

Such a chart can be used to assist the operation of a LSP process. Each process would need to have the Control Line (CL), Upper Control Limit (UCL) and Lower Control Limit (LCL) firmly established beforehand. Experimental research is required to obtain stable operating parameters and the boundary conditions that can support stability.

A starting control limit may be inspired from the AMS2546A standard, section 3.3.4.1 which places a ±10% limit on the beam energy [67]. If ten consecutive shots exceed or fall below this limit, the control condition is violated. As a more flexible control limit, the CL of a bubble lifetime diagnostic may be established with an averaged value at a given laser operating point. The UCL and LCL may then be calculated either as ±10% from the average or as a multiple of the standard deviation of the average bubble lifetime.

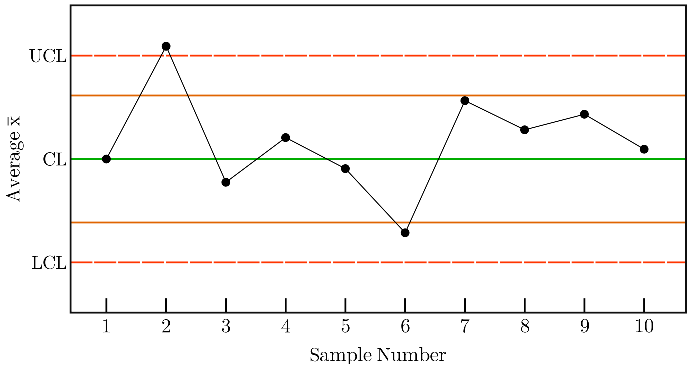

Figure 7.33: An example of a process control chart showing the variability and limits.

Figure 7.34 illustrates a control chart that has UCL and LCL lines plotted by shifting the fitted curve (refer to Figure 7.32) vertically up and down. The Test 2 data set was used to set control lines at ±3 standard deviations from the centre. For illustration, data points outside of these boundaries (here the stagnant points) are considered out of control. This demonstrates the diagnostic potential of laser induced cavitation bubbles in identifying stagnant water conditions over a range of laser power intensities.

7.6.4 Bubble Lifetime Saturation

In previous experiments, a form of saturation of the bubble time with power intensity has been identified based solely upon visual inspection of the slope or the variance of the averages, but no exact point has been identified. In order to more reliably ascertain a realistic point of saturation, a curve is fitted to each data set, shown in Figure 7.35. After fitting a rational function curve, the analytical point of saturation is found by iteratively assessing for a doubling in power intensity, the earliest point at which the bubble lifetime increases just below a threshold. In Figure 7.35, the power intesity of five different tests are shown for a saturation threshold of 10%.

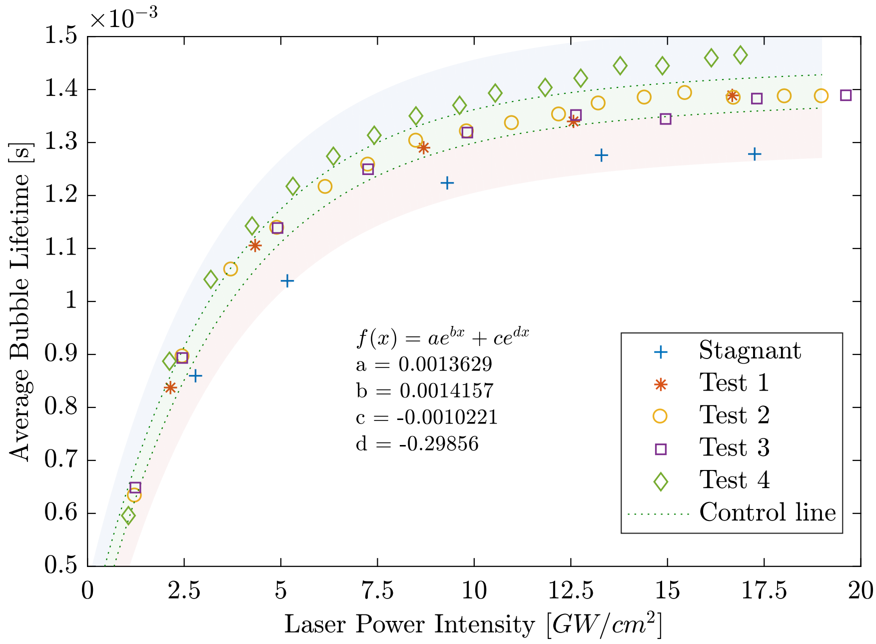

Figure 7.34: Control boundaries based on the fitted curve in Figure 7.32.

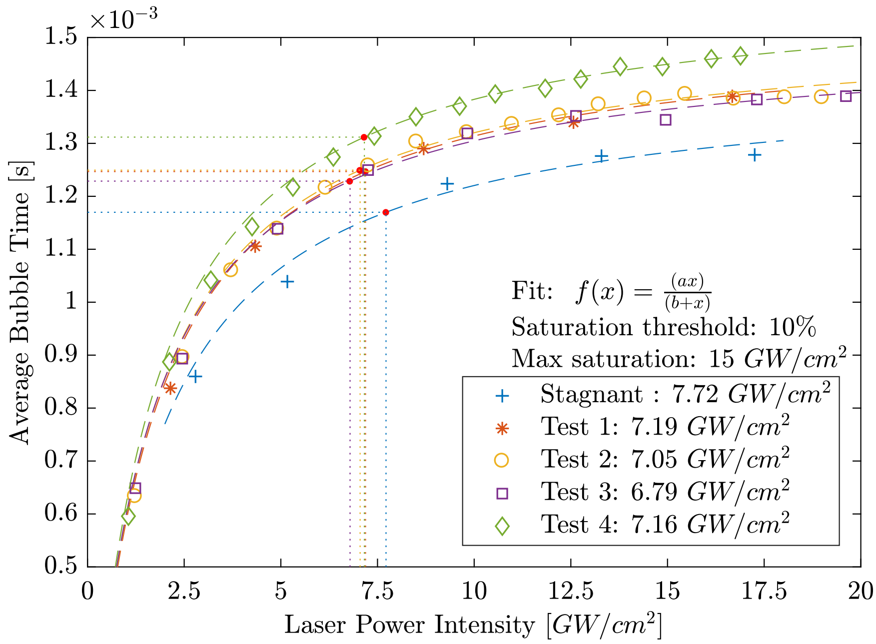

Figure 7.35: Analytical points of saturation for different tests.

Systematically, the point of saturation represents the capability of the diagnostic in this particular operating condition; beyond this point it becomes difficult to determine the laser input from a given bubble time.

Experimentally, this point represents the highest effective energy transfer from laser to bubble energy within the system. This limitation is enforced by the narrowing laser beam reaching the breakdown strength of the water, where the power intensity is close to the maximum but before the target. After breakdown becomes present, any more laser energy is readily absorbed in this premature plasma.
Monitoring the laser beam prior to the target will not reveal this, yet the limits of this experiment are readily observed with the cavitation bubble period.

Summary:

- The presence of the tube caused a minor increase in bubble lifetime compared to an open water tank.
- Flowing water increased the cavitation bubble lifetime by up to 8.22% due to clearing the beam path more effectively or by reducing the local static pressure around the bubble or a combination of these two reasons.
- Flowing water also reduced the variability in bubble lifetime by 31.79% at a 0.05 Hz pulse repetition rate of the laser. A the greatest stability was seen at a 1 Hz repetition rate.
- A two-term exponential curve and a rational function could both be closely fitted to the data points, approximating the relationship between bubble lifetime and laser energy in this system.
- A control chart with control limits based on ±3 standard deviations of the fitted curve demonstrated the diagnostic potential of laser induced cavitation bubbles.
- A range of systematic saturation was identified at power intensities between 6.5 GW/cm^2 and 7.5 GW/cm^2.

7.7 Near Edge Effect

When panel sections are processed with LSP in industry, it may well be required to treat the metal from edge to edge. As a diagnostic system needs to accommodate this feasible scenario, the shape and bubble size of laser induced cavitation bubbles within proximity to a plate edge was explored in this experiment.

Explanation of Experiment

The front face refers to the laser irradiated side of a 304 stainless steel plate, the rear face refers to the opposite side of this plate. In Figure 7.36, the entire plate was submerged and both sides were in contact with water.

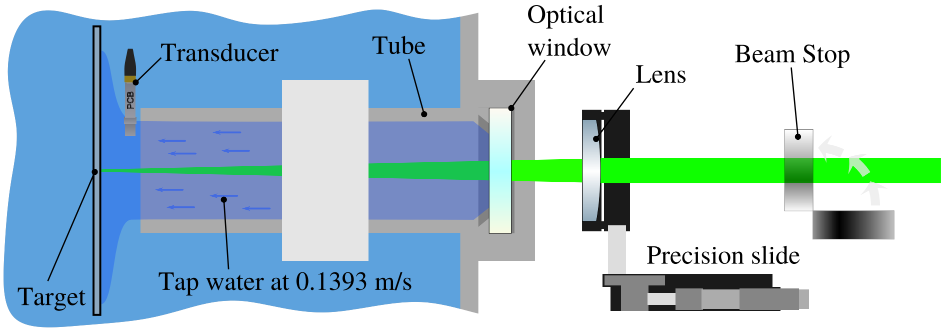

Figure 7.36: Experimental set up of the flowing tap water tests on a large flat plate target.

Table 7.8: Edge test parameters.

Parameter	Value
PI	8.3 GW/cm^2
Average Spot Diameter	1.01 mm
Rep Rate	1 Hz
Water conductivity	Tap 200.6 μS/cm @ 24.3 °C
Water velocity	0.139 m/s
Target curvature	0 mm (plate edge)

The laser was positioned on the plate as now described:
At 0.0 mm: After the initial spot size was fixed at a diameter of 1 mm, the target was moved along a plane by incrementally on the edge of the beam, such that the laser beam narrowly missed the plate, and ablation of the metal was no longer observed.

At 0.5 mm: The 3D printer X-axis was then manually incremented 0.5 mm into the beam path. This meant half the beam bypassed the target while the other was blocked by the target.

At 1 mm: The 3D printer X-axis was then manually incremented 0.5 mm further into the beam path which means the beam was fully blocked by the plate.

At 2 mm - 20 mm: The target was then manually incremented further. The beam was fully blocked by the plate at this distance from the edge and all distances further. Figure 7.37 summarises these relative positions of the laser spots on the edge of the plate.

Observations

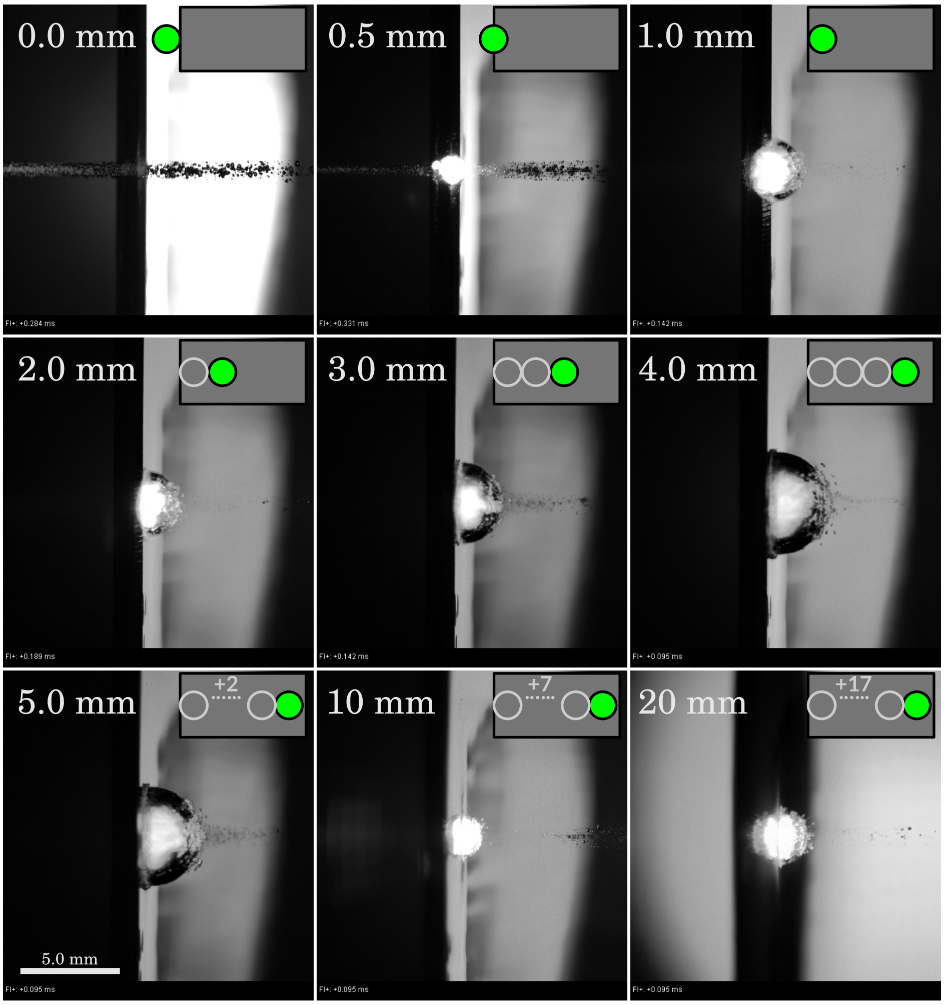

Figure 7.37: Collection of first frames from the edge tests, each being 0.047 ms after a 8.3 GW/cm^2 laser pulse. The green dot shows the relative position of the 1 mm laser spot to the edge of the plate.

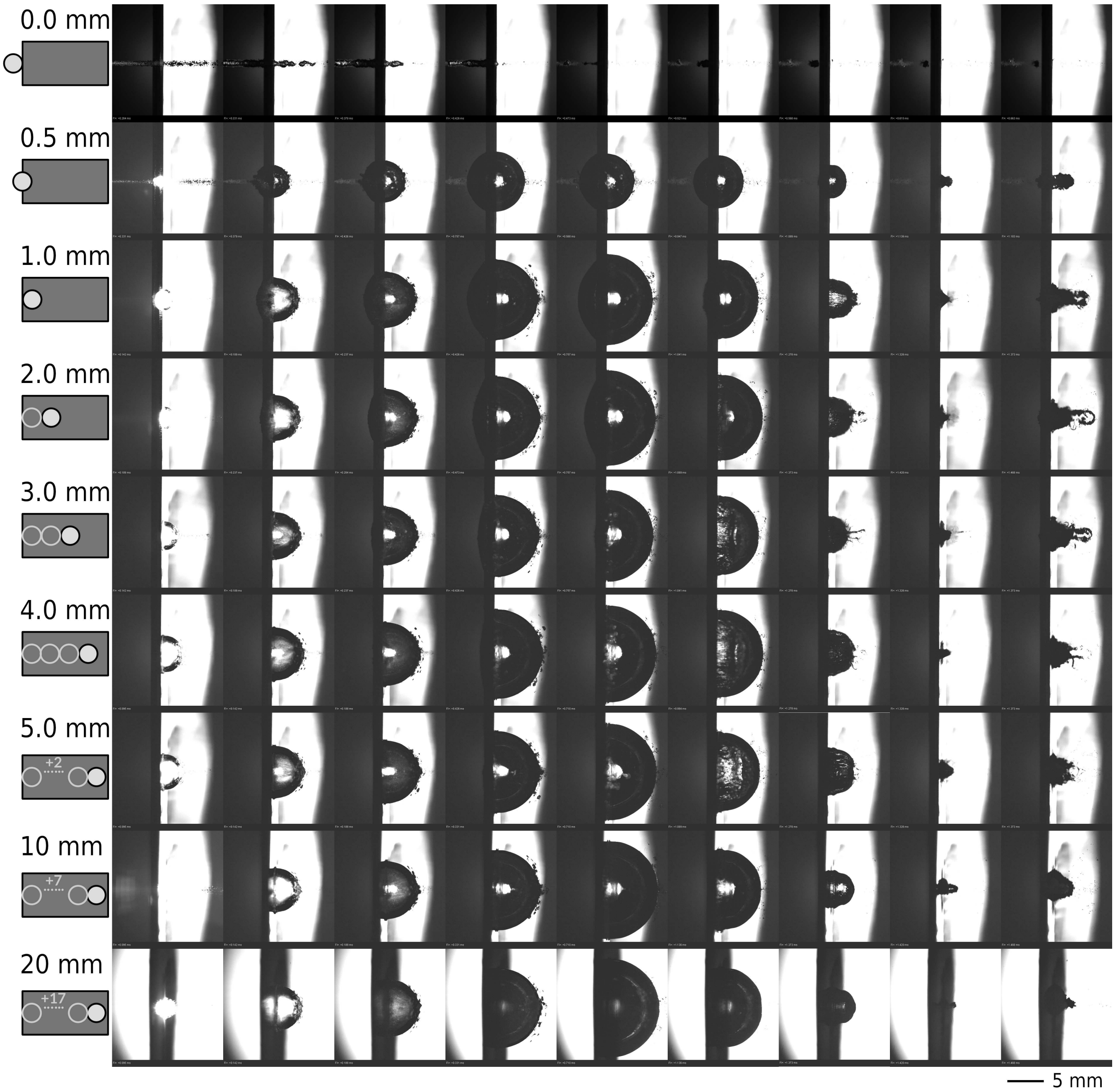

Figure 7.38: High speed imagery of edge tests at varying distances (0 mm - 20 mm) from the edge. Maximum bubble radius along beam path was 7.06 mm. All tests at 8.3 GW/cm^2.

Description of high speed images

At 0 mm: A cylindrical cloud of cavitation bubbles was observed along the beam path as the laser energy was absorbed by the water; it completely missed the metal target surface.

At 0.5 mm: The bubble was formed almost immediately on the edge and grew to wrap asymmetrically around the back of the plate. The total size of this bubble was considerably smaller than that of the subsequent bubbles. The collapse was also asymmetric; the bubble on rear face was diminished sooner than the front.

At 1 mm: The growth of this bubble was highly asymmetric over the plane of the plate. Like with the 0.5 mm case, the bubble grew larger on the front face. The bubble appeared to grow beyond the edge to wrap around the rear of the plate. The rear side of the bubble was flatter and less spherical than the front. It also had a turbulent or textured surface. After the final bubble volume was reached, the rear part of the bubble appeared to rush around the the edge to meet the front part in one single collapse. A rebounding cavitation cloud was observed on the front face after collapse. A similar cloud occurred to a lesser extent on the rear.

At 2 mm: Similarly to the 1 mm distance, the growth of this bubble was highly asymmetric over the plane of the plate, with more of the bubble volume found on the front face. The growth of the front bubble continued 3 frames beyond the point where the rear began to collapse. Similar rebounding cavitation clouds were observed upon collapse.

At 3 mm to 4 mm: Similarly to the 2 mm distance, the growth of these bubbles was once again asymmetric over the plane of the plate. One notable change was the reduction of the maximum rear side bubble volume, and the reduction of the cavitation cloud on the rear side upon bubble collapse, in the final frame.

At 5 mm: The bubble was reaching over the edge, but no longer convincingly wrapped around to the rear face of the plate. Collapse was still asymmetric where the edge portion of the bubble rushed to collapse nearly on the laser spot.

At 10 mm to 20 mm: The bubble grew to a maximum radius of roughly 7 mm and collapsed symmetrically about the laser axis. The maximum size of the cavitation bubble was within the edge of the plate. A rebound bubble was observed after the initial bubble collapsed at the location of the laser spot.

On the near-edge tests (0.5 mm to 4 mm), it appeared that two separate bubbles are formed; behind and on the front side of the plate. This was however not validated as this second bubble was reduced with the target movement and was entirely not present in those tests further (5 mm to 20 mm) into the plate.

Instead, it may be that the rear bubble was an extension of the front bubble and followed the edge of the plate as it collapsed into the front bubble. This means that near to the edge of the plate, in addition to growth on the front and rear, part of the bubble grew along the camera axis.

Bubble time

Figure 7.39 shows the variation of bubble lifetime time compared to the distance from the edge. Each point was an average of 3 shots, and measurement uncertainty was shown in error bars. Between 0.5 mm and 1 mm distances was a rapid increase in bubble lifetime. Thereafter an upward or growing trend was seen from 1 mm to 2 mm offset distances. In the subsequent points, the bubble lifetime increased, though not at a rapid rate. The last point, fired at 40 mm from the edge, was included on this plot from a prior test to understand how the bubble behaved beyond 20 mm from an edge.

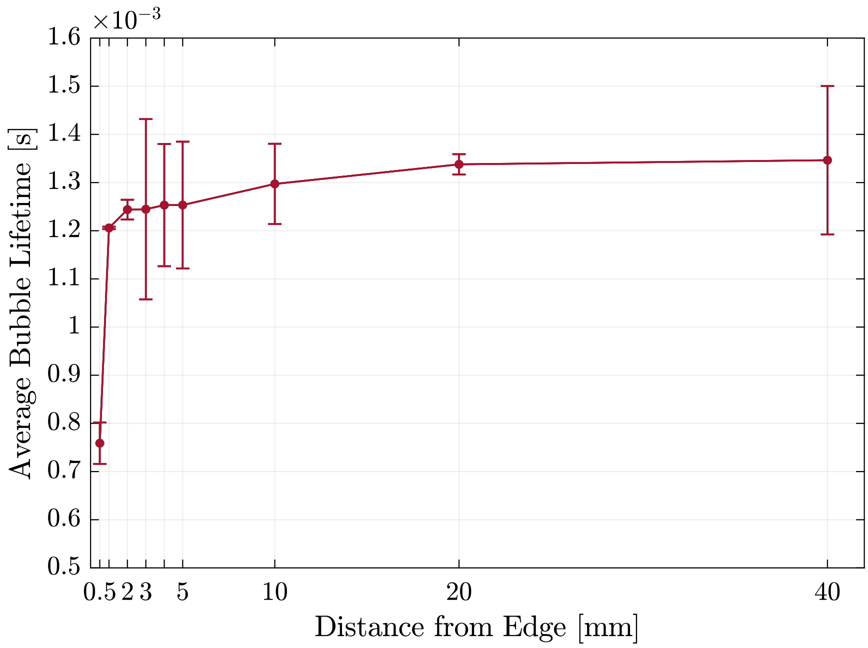

Figure 7.39: Bubble lifetime at varying distances from the edge of a plate. Each point shows an average of three bubbles and each error bar represents the measurement uncertainty.

The reason for the sudden spike in bubble time from 0.5 mm to 1 mm was due to the sudden two fold increase in area that could absorb the laser radiation, from effectively a 0.5 mm diameter to 1 mm.

The second steepest increase in bubble lifetime occurred from 1 mm to 2 mm from the edge of the plate. In this case, both spots were fully on the target surface which implies that all the available laser energy was absorbed in both positions. Studying the high speed imagery, it can be seen that the proportion of the total bubble volume which was behind (and on the side of) the plate was lessened between the 1 mm to 2 mm points. This means that less of the bubble energy was spent creating an unstable void that detaches rapidly, and the stable bubble time increases.

Between the 3 mm and 5 mm points, the gradually decreasing volume of the void behind the plate could be attributed to the increasing distance from the edge. At 5 mm there was no longer a discernible bubble that appeared behind the plate as it was roughly one bubble radius length from the edge. All three of these bubbles collapsed asymmetrically, initiated from the edge of the plate.
At 10 mm to 40 mm points the bubble growth and collapse was symmetrical, unaffected by the edge as it only made contact with the flat plate surface. The bubble lifetime was comparable to that of the previous tests.

For all spots that fell fully on a flat stainless steel plate, the proximity to the edge reduced the bubble lifetime by a maximum of 9.8% compared to those far (20 mm) from the edge. The variances of the bubble life times positioned at 1 mm and 2 mm from the edge were smaller than that of 3 mm, 4 mm and 5 mm from the edge. It is postulated that at points nearest to the edge, the bubble had sufficient energy to remain attached to the side and rear surfaces of the plate in the early stages of bubble expansion. This attachment then provided repeatability of bubble behaviour. Once the centre of the bubble moved beyond 3 mm, it met the edge of the plate later on in its expansion and with correspondingly less sustaining energy than earlier. This means the edge, once separated from the bubble wall, behaved as a discontinuous pressure boundary, and initiated collapse with greater uncertainty.

Summary:

- If the laser spot did not fully fall on the surface of the target, less of the available laser energy was absorbed and the resulting cavitation bubble was substantially reduced.
- If the spot was fully on the surface of the target metal, but within one maximum bubble radius of an edge, the cavitation bubble growth was destabilised and its life time was reduced proportional to the proximity to the edge.
- If the spot was further than the maximum bubble radius from an edge, it produced a stable bubble within 5% of the maximum bubble size.

7.8 Geometrical Boundary Effects

As mentioned in Section 2.4.1, Godwin et al. postulated that both toroidal flow towards the centre of the bubble during collapse, and the presence of a solid boundary are a hindrance to cavitation collapse [39]. This implies that if there is any geometrical boundary supporting this effect by hindering the flow, or inducing similar toroidal flow, it will do likewise and extend the collapse time for the cavitation bubble.
This experiment was performed to understand how different geometry - concave and convex surfaces in a material and pulse rate typically found in industry - affect cavitation bubble oscillation periods and to what extent.

7.8.1 Explanation of Experiment

The average spot size, recorded here, was measured both before and after the experiment on a flat plane. A fixed offset distance from the tube exit was used to ensure the same beam length (and spot size) was present to the middle surface of each target. A summary of the experimental parameters was found in Table 7.9. Figure 7.40 shows the position of the tube, targets and transducer in the water.

Table 7.9: Geometery test parameters.

Parameter	Value
PI	$8.3\,\mathrm{GW/cm^2}$
Average Spot Diameter	1.011 mm
Rep Rate	1 Hz and 10 Hz
Water conductivity	Tap 200.2 μS/cm @ 24.3 °C
Water velocity	2.23 m/s
Target curvature	channel or semi-cylinder -5 mm to 5 mm radius

This experiment made use of various test targets cut from a martensitic chromium steel turbine blade. These, shown in Figure 7.41, were convex and concave semi-cylindrical shapes each on the surface of a 20 mm × 20 mm block. These blocks were clamped on a jig for easy alignment and removal. Each shot was focused on the surface to have approximately 1 mm spot size at a 400 mJ laser energy for a power intensity of approximately $8.3\,\mathrm{GW/cm^2}$.

Figure 7.42 illustrates that convexity was taken as a positive radius (protruding out of the surface) and concavity was taken as a negative radius (dipping into the surface).

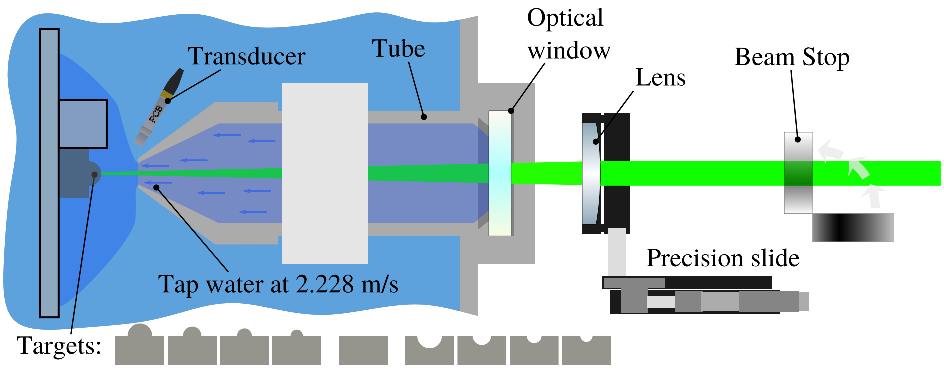

Figure 7.40: Experimental set up of the flowing tap water tests on varying chromium steel target geometries.

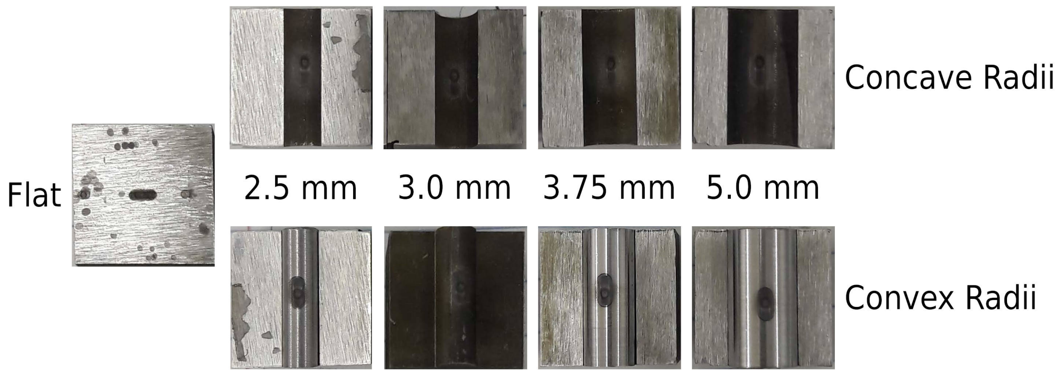

Figure 7.41: Various curvature shapes tested.

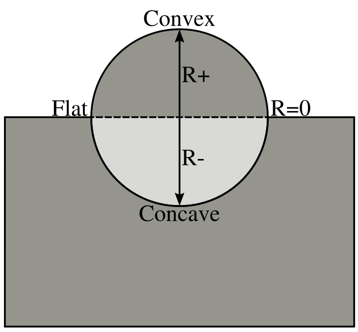

Figure 7.42: Convex radii were assigned positive values, concave radii were assigned negative values. Flat targets had no curvature, or zero radii.

7.8.2 Bubble Lifetime Observations

As the concave geometry in Figure 7.43 became shallower, that is the concave radius decreases in depth towards zero, so too did the first bubble oscillation period or bubble lifetime. For a −5 mm to −2.5 mm concave channel change, the first bubble oscillation period reduced by 0.088 ms or 5.61%. As the convex geometry in Figure 7.44 became prouder, that is it increases in convex radius 3 mm to 5 mm, so the first bubble oscillation period reduced overall by 0.108 ms or 7.51%. Figure 7.45 shows that a flat target near the corner clamp displayed 8.28% larger bubble time (or 0.112 ms longer) than the same target surface further from the clamp. The stagnant and flowing tests near the clamp produced nearly identical average results, within 0.0684%.

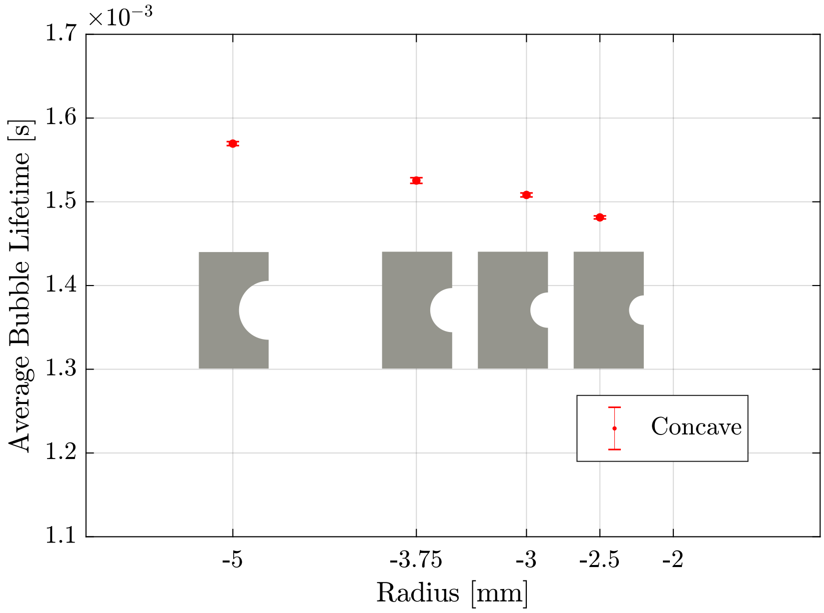

Figure 7.43: Plot showing average bubble lifetime (of at least 9 points) of concave geometry plotted against target radius at 1 Hz at 8.3 GW/cm^2, with flowing water at 2.23 m/s.

Figure 7.46 shows the effect of curvature in general (with one exception at 2.5 mm in both flowing and stagnant water); the bubble period increased with larger concave radius, and decreased with larger convex radius. Flat targets produced bubble periods between these. The largest (−5 mm) concave target showed a 7.17% longer bubble lifetime than the flat target and the largest (+5 mm) convex target showed a 9.08% smaller bubble lifetime than the flat target.

In Figure 7.46, it is clear that a similar result was present at a industry laser pulse rate of 10 Hz as at the experimental 1 Hz. The 10 Hz pulse rate was distinguished by an overall vertical shift upward regardless of the geometry.

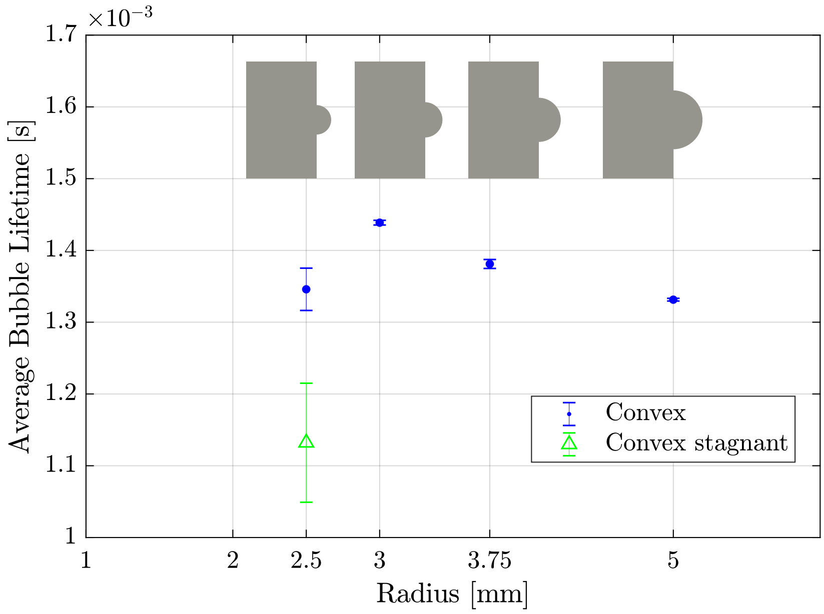

Figure 7.44: Plot showing average bubble lifetime (of at least 3 points) of convex geometry plotted against target radius at 1 Hz at 8.3 GW/cm^2, in stagnant and flowing water at 2.23 m/s.

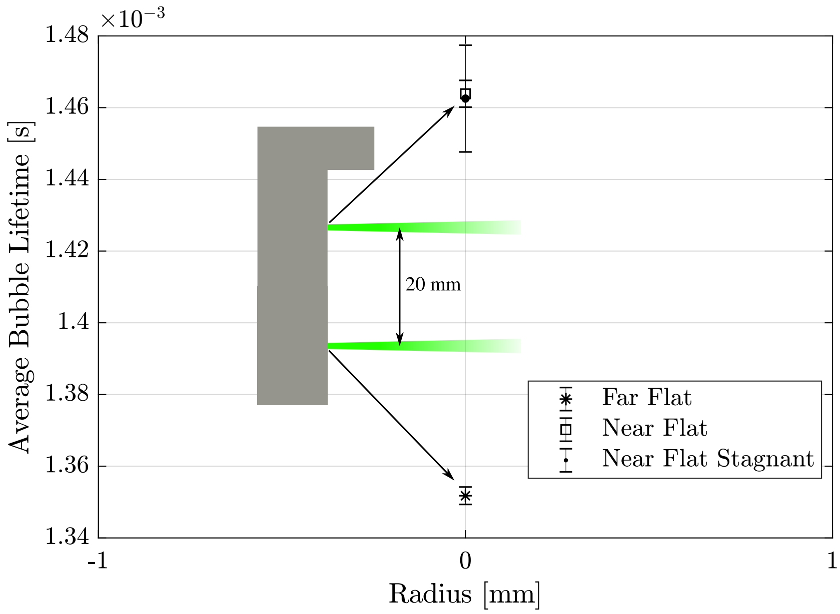

Figure 7.45: Plot showing average bubble lifetime (of at least 3 points) of flat geometry irradiated at 1 Hz, 8.3 GW/cm^2, in stagnant and flowing water at 2.23 m/s.

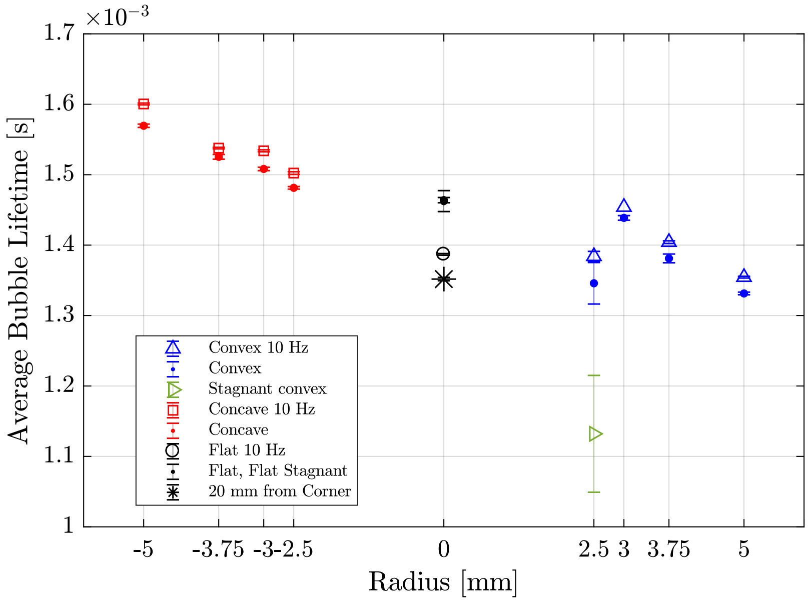

Figure 7.46: Average of at least 10 bubble lifetime points plotted against target radius with 8.3 GW/cm^2 laser pulses at 1 Hz and 10 Hz, in stagnant and flowing water at 2.23 m/s.

The energy received by the energy meter during these tests is shown in Figure 7.47. It is evident that all tests at 1 Hz were performed at near 0.4 J.

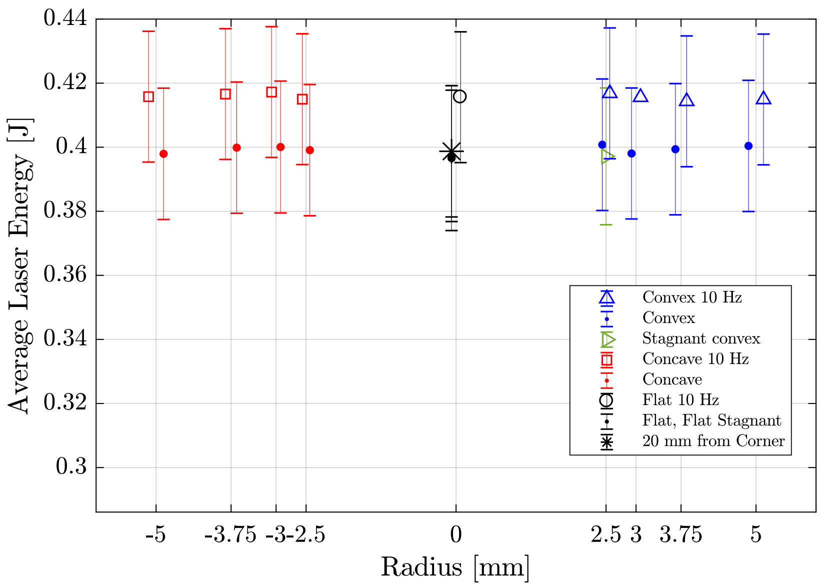

Figure 7.47: Average of at least 10 Laser Energy points plotted against target radius at 1 Hz and 10 Hz. Points were slightly displaced horizontally for clarity.

7.8.3 Discussion

A similar trend to that in Figure 7.46 was found by Tomita et al. in Section 2.4.1. Their results and those seen here, however, are not directly comparable since this experiment made use of target boundaries that are smaller than the bubble maximum diameter, and used hemispherical bubbles that were attached to the target surface, whereas Tomita et al. did experiments on spherical bubbles in proximity but not touching the nearby and with much larger surrounding geometries [40].

As with the previous flowing experiments, the bubble lifetimes were stable, with one exception at the flowing and stagnant test on the +2.5 mm radius target in Figure 7.46.

The effect of geometry on the life time of cavitation bubbles was significant. Since the comparable case (far from the clamp, in flowing conditions in Figure 7.45) produced similar results to that of the flat plate experiment in Figure 7.32 prior, the change due to the target and other nearby geometry is apparent. Each case was affected in three ways: proximity to the clamp, whether its surface was flat/concave/convex and the radius of that geometry. The proximity to the clamp increased the flat bubble life time by 8.28%, which is a significant change. This increase was assumed to be present in all other concave/convex cases, though this was not verified.
A larger concave radius displayed a longer cavitation bubble life time, the increase was 5.61% between a 2.5 mm to 5 mm radius channel. In general, a larger convex semi-cylinder displayed a shorter bubble life time, the largest decrease was 7.51% between 3 mm and 5 mm radius semi-cylinders. From the largest concave radius to the largest convex radius, the bubble lifetime reduced by 15.17%.

The increase in bubble lifetime between the 1 Hz and 10 Hz pulse rates can be explained in two ways; a slight increase in the energy of the laser or a slight increase in spot size as that in Figure 7.2 (around +11%). Figure 7.47 demonstrates that there was an increase in laser energy (around +4.3% from the data) for all geometry tests with the increase from 1 Hz to 10 Hz. The difference was consistent and stable; when the laser energy was set at 1 Hz, an increase would be present if the laser was switched to a 10 Hz pulse rate. The energy remained at this level with comparable variance as at 1 Hz, given by the similar length of measurement uncertainty bars in Figure 7.47. Since spot sizes were not measured in during these pulse rate changes, this increase in laser energy is the most plausible explanation for the increase in bubble lifetime. Interestingly, this statement cannot be applied to the flat geometry at 1 Hz, which when at 10 Hz displayed a reduced bubble lifetime despite the increased laser energy.

7.8.4 High Speed Image Observations

High speed footage of the cavitation bubbles with different target geometries and flow fields is shown in Figure 7.48.

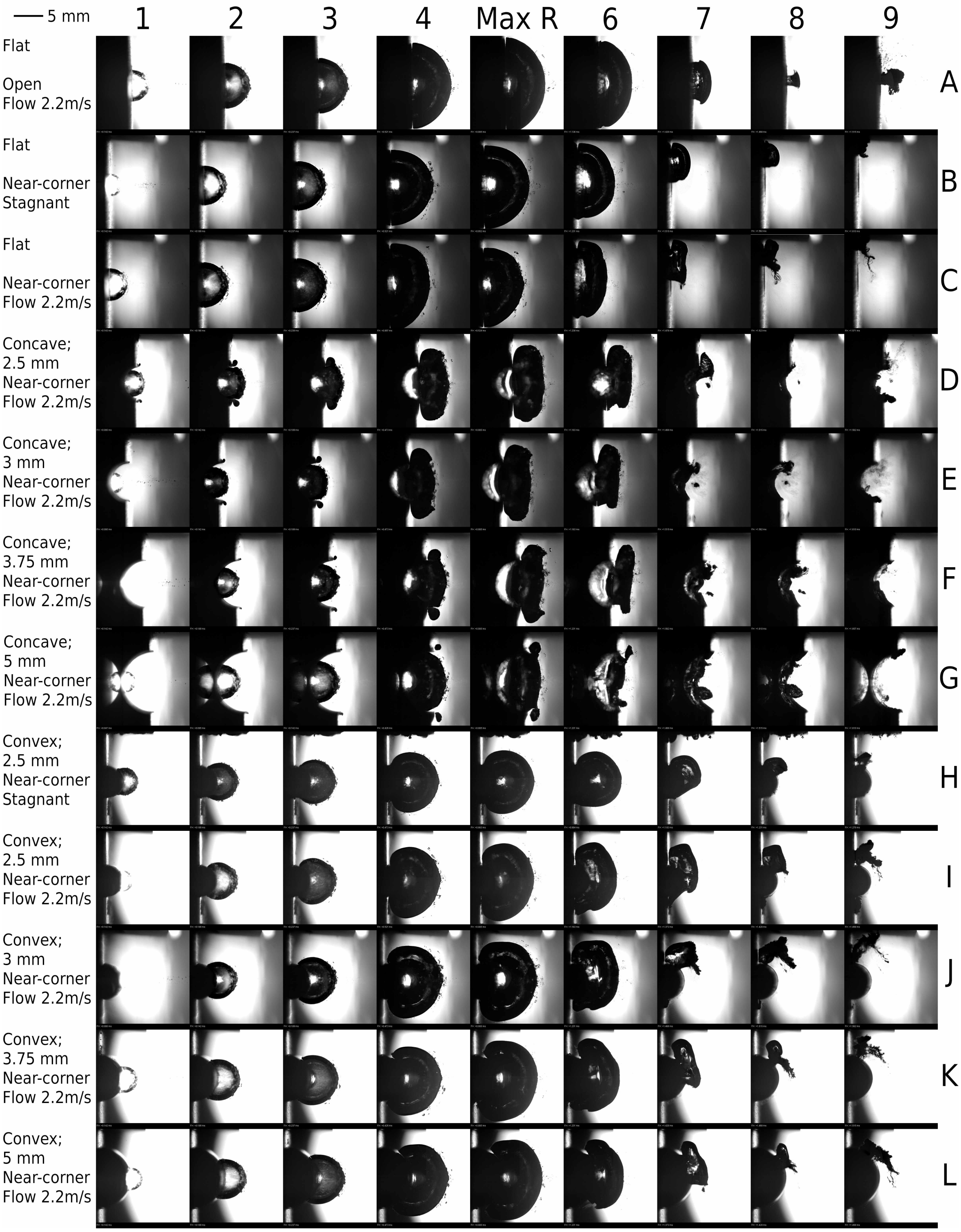

Figure 7.48: Summary of high speed images for flat, concave and convex geometry changes.

Figure 7.48 demonstrates the similarities and differences between each test. Row A was the only test not done near the internal corner made by the mounting clamp. It demonstrated a good baseline behaviour of a hemispherical bubble in flowing water with minimal geometry boundary effects. The subsequent images (Row B to L) were all near the clamp holding the sample.

Within these high speed images, a particularly obvious feature is the shape of expanding cavitation bubbles attached to concave radii.
In general, the expansion phases (in results row D to G in Figure 7.48) produced nearly hemispherical bubbles until the bubble boundaries met with the concave surface. During this time, the outward flow of liquid displaced by the cavitation created a region of separated flow on the outer edges of the concave recess. This region is thought to be a flow separation bubble. The potential maximum bubble size for the same laser exposure was seen in the flat test, row A. This means that the size of the cavity was significantly larger than the concave geometry features tested here and that the expansion occurred beyond the boundary into the open water. As the cavitation bubble was constrained either side, it was directed out of the geometric cavity and met with the separation bubbles on the sharp corners. These coalesced and the resultant largest volume took on the form of a mushroom top. It is also postulated that the expansion of the bubble occupies the length of the concave channel (along the axis of the camera) but the shape was not confirmed by these results.

The cavitation bubbles attached to convex radii look and behave more like the bubbles on a flat surface than those on concave radii. A closer-to-spherical shape was flattened by the flow of water impinging on its top shape along the laser axis. The presence of the nearby boundary wall flattened the one side of the bubble to some extent as well. During the collapsing phases, the bubble reduced in size asymmetrically, leaning towards the corner. In Row I, in Figure 7.48, the progression towards the corner appeared to split the collapsing cavity, leaving a smaller bubble separated by the 2.5 mm radius geometry in frames 8 and 9.

7.8.5 Discussion

The presence of the inside corner due to the clamp affected the manner in which bubbles grew and collapsed. The shape of the bubble during expansion was slightly affected in the flat tests (rows A to C) and the convex tests (rows H to L). Figure 7.49 illustrates the progression of the bubble towards the inside corner during collapse. The corner appeared to affect all tests done nearby in this way.

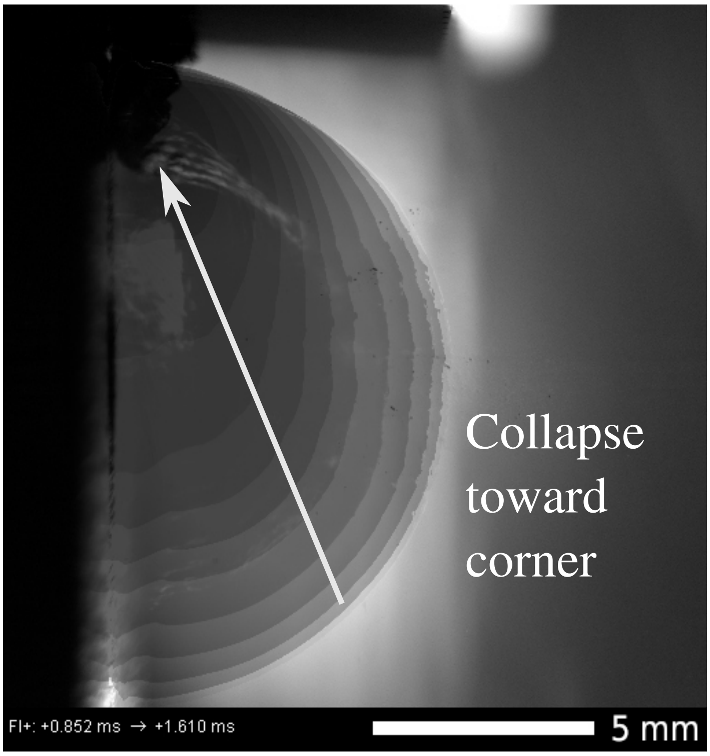

Figure 7.49: Progression of bubble collapse from maximum radius for flat target near corner (Row B in image above). Produced by laser pulse at 8.3 GW/cm^2, in stagnant tap water.

The important attribute of bubbles, particularly those that collapse toward a corner, is the nature of the shock wave emitted. In a symmetrical collapse, the shock wave was produced from a focussed bubble volume on the surface of the target. The resultant shocks, shown in Figure 7.50a, were uniform and intense. In a corner affected collapse, the bubble location migrated, introducing further non-uniformity and the final shape was more of a cloud, such that the energy of the collapse was both dispersed and disordered. The received shock wave, shown in Figure 7.50b, was of a lower pressure and less pronounced than that of a symmetrical case. This may however be due to the transducer placement no longer being in an optimal position (due to the bubble migration towards the corner) to record the shock wave passing. Schlieren flow visualisations can be used to understand this result in future work.

This affirms the important role of geometry in the behaviour of cavitation bubbles. This is of great importance if the diagnostic tool is applied to LSP of continually changing geometry such as gear teeth, shafts or the fir tree roots of turbine blades. If the geometry is not easily predictable, this is anticipated to severely limit the applicability of the diagnostic tool.

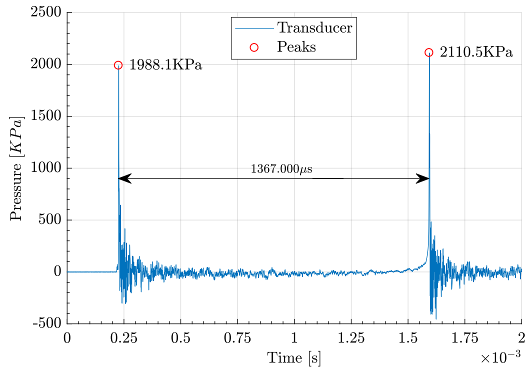

(a) Pressure waveform for a symmetrical bubble collapse on a flat surface 20 mm from an internal corner.

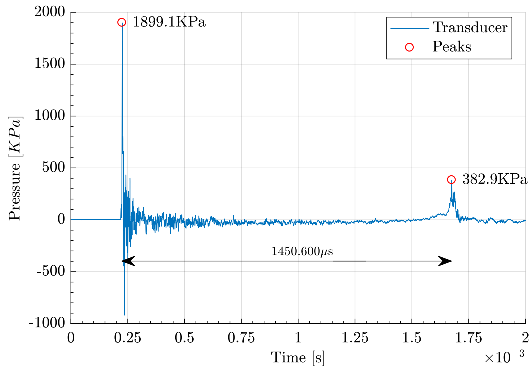

(b) Pressure waveform for an asymmetrical bubble collapse on a flat surface near an internal corner.

Figure 7.50: Cavitation bubbles in flowing water at 2.23 m/s at an average power intensity of 8.3 GW/cm^2.

Summary:

- The control case of a flat geometry, flowing (and stagnant) water with no nearby corner produced comparable results to those points near 8.3 GW/cm^2 in a previous experiment, Figure 7.32.
- Any cavitation bubble near an internal corner collapsed asymmetrically towards the corner. This occurred regardless of the presence of flow or not.
- The presence of a nearby internal corner geometry extended the lifespan of the cavitation bubble on a flat surface and potentially other surfaces.
- As the target geometry changed from the largest concave radius to the largest convex radius, the bubble lifetime reduced by at most 15.17%.
- The increase in frequency increased bubble lifetimes by 4.3%, attributed to a laser characteristic which increased the pulse energy when the pulse repetition rate changed from 1 Hz to 10 Hz.
- The bubble lifetimes of flat targets in flowing and stagnant water were comparable within 0.0684%.
- The geometry or shape of the target had greatest effect on bubble lifetime, the water flow field had the next greatest effect.

7.9 Experimental Summaries

- Pressure measurement system
  - The transducer displayed peaks with high signal to noise ratio making peak detection possible and reliable.
  - The rise in pressure for the laser shock wave was much steeper (more rapid) than the cavitation shock wave.
  - The design of the clipper limiting circuit was conservative, limiting the volage output to around 7.668 V or corresponding pressure of 2130 kPa.
  - The peak values of both laser and cavitation induced shock waves were similar due to the waveform being clipped above 2130 kPa.
  - Above an amplitude of 2130 kPa, the uncertainty associated with the peak locations and corresponding bubble time was 400 ns. The conservative peak detection uncertainty is 1.2 μs.
  - An erroneous waveform was remedied by replacing the transducer.
- Difference between deionised and tap water
  - Laser exposure on the target surface under stagnant conditions produced a hemispherical bubble that remains attached to the surface during growth and collapse.
  - The maximum bubble size in deionised water was significantly larger than that of tap water for the same laser output energy.
  - Dielectric breakdown of the water left more bubbles in the beam path in tap water than in deionised water.
  - Residual products of ablation hindered the next laser pulse in a stagnant tank.
- Effect of laser repetition rate
  - The first laser shot fired in stagnant conditions always produced the largest cavitation bubble.
  - On average, the bubble time difference and corresponding laser energy loss increased after first shot with higher power intensities. The increasing trend appeared to saturate at a power intensity of around 9.3 GW/cm^2.
- Effect of test duration
  - After eleven minutes of LSP at a high power intensity and high repetition rate, the average bubble lifetime diminished by 23.57%, indicating a diminishing beam delivery to the target surface.

  - The water conductivity within the tank increased by 0.0946% over the duration of the test, which was within the uncertainty of the conductivity measurement. This means conductivity was essentially constant.
  - Small gaseous vapour bubbles within the water surrounding the cavitation event were present in every test, and were thought to be the primary contributors to the reduction in delivered beam energy.
  - It is currently unclear whether the conductivity was an insensitive indicator of likely dielectric breakdown in this experiment or if a poor measurement of conductivity was recorded altogether.

- Effect of power intensity in tap water
  - The point at which the system began to saturate appeared to be associated with the point with greatest variance in stagnant water.
  - The saturation point appeared to be an important indicator of the laser cavitation bubble system predictability.

- Flow within a tube
  - The presence of the tube caused a minor increase in bubble lifetime compared to an open water tank.
  - Flowing water increased the cavitation bubble lifetime by up to 8.22% due to clearing the beam path more effectively or by reducing the local static pressure around the bubble or a combination of these two reasons.
  - Flowing water also reduced the variability in bubble lifetime by 31.79% at a 0.05 Hz pulse repetition rate of the laser. A the greatest stability was seen at a 1 Hz repetition rate.
  - A two-term exponential curve and a rational function could both be closely fitted to the data points, approximating the relationship between bubble lifetime and laser energy in this system.
  - A control chart with control limits based on ± 3 standard deviations of the fitted curve demonstrated the diagnostic potential of laser induced cavitation bubbles.
  - A range of systematic saturation was identified at power intensities between $6.5\,\mathrm{GW/cm^2}$ and $7.5\,\mathrm{GW/cm^2}$.

- Effect of edge
  - If the laser spot did not fully fall on the surface of the target, less of the available laser energy was absorbed and the resulting cavitation bubble was substantially reduced.

  - If the spot was fully on the surface of the target metal, but within one maximum bubble radius of an edge, the cavitation bubble growth was destabilised and its life time was reduced proportional to the proximity to the edge.
  - If the spot was further than the maximum bubble radius from an edge, it produced a stable bubble within 5% of the maximum bubble size.

- Effect of boundary geometry
  - The control case of a flat geometry, flowing (and stagnant) water with no nearby corner produced comparable results to those points near 8.3 GW/cm^2 in a previous experiment, Figure 7.32.
  - Any cavitation bubble near an internal corner collapsed asymmetrically towards the corner. This occurred regardless of the presence of flow or not.
  - The presence of a nearby internal corner geometry extended the lifespan of the cavitation bubble on a flat surface and potentially other surfaces.
  - As the target geometry changed from the largest concave radius to the largest convex radius, the bubble lifetime reduced by at most 15.17%.
  - The increase in frequency increased bubble lifetimes by 4.3%, attributed to a laser characteristic which increased the pulse energy when the pulse repetition rate changed from 1 Hz to 10 Hz.
  - The bubble lifetimes of flat targets in flowing and stagnant water were comparable within 0.0684%.
  - The geometry or shape of the target had greatest effect on bubble lifetime, the water flow field had the next greatest effect.

8 Discussion

The practical objective of this study was to evaluate the use of cavitation bubbles as a diagnostic tool to monitor the LSP process. This was achieved by identifying and quantifying factors that affect (1) the accuracy of the diagnostic (i.e. stability) and (2) the useful range (i.e. saturation behaviour).

The experiments presented here explored the initial behaviour of bubbles within stagnant conditions, in both tap and deionised water. The study progressed to more realistic industrial operating conditions, with flowing tap water and variations in geometry.

8.1 Objectives Achieved

Within the first experiments, the conditions for successful evaluation of laser induced cavitation bubbles were achieved. Results produced here compare favourably to that in literature:

High speed imagery shows that the bubbles formed on a flat surface grow and collapse in a symmetrical fashion. In particular, Figures 7.10, 7.12 and 7.13 emulate the results of Nguyen in Figure 2.10 [36]. This is in spite of an orientation to gravity that differs by ninety degrees.

The waveform, in Figure 7.3, obtained with the 113B21 pressure transducer shows high signal to noise ratio, good peak prominence and repeatable response characteristics. This is comparable to the waveform found in Figures 2.14, 2.19a and 2.20b [41, 28, 61]. The shock detail in Figure 7.4 displays a steep laser shock wave and rise in the bubble collapse shock wave, comparable to that in Figure 2.15 [43].

As power intensity was increased, the bubble lifetime for both stagnant and flowing water displayed a continuous, gradual, non-obvious point of saturation, in Figure 7.35. Making use of the discrete curve that was fitted gave a comparable power intensity saturation to that found in Figures 2.7 and 2.6 at 532 nm [27, 31]. The earliest reasonable power intensity at which the bubble lifetime saturated was around $6\,\mathrm{GW/cm^2}$.

The lifetime of a hemispherical bubble in Figure 7.46 is extended with concave targets and reduced with convex target surfaces. This is a similar result found by Tomita et al. in Figure 2.12 however, with their bubbles formed at a distance with the surfaces [40].

In submerged LSP, the diagnostic potential of cavitation bubble lifetimes is comparable to the previous real time diagnostic attempts in thin water LSP [13] [60]. In particular, Figure 7.35 shows an increasing (albeit non-linear) trend comparable to the PMT in Figure 2.21 and saturation of power intensity very similar to Figure 2.19b.

The acceptable correlation between the observed results and literature affirms the scientific value of the methods employed.

8.2 Unexpected Results

The lack of conductivity change within the long duration experiment, as seen in Figure 7.22, and the implied unsuitability of the conductivity meter in detecting laser transmission conditions, were not expected prior to this experiment. As a conductivity study was not a primary objective, the research was able to continue without meaningful comparison between water conductivity and breakdown susceptibility.

The laser spot size was not anticipated to change significantly over the course of the day, since the laser cooling and room conditioning systems were both temperature controlled at 20°C. As indicated in Figure 7.2, the spot size clearly decreased over the course of multiple measurements in one day. This change was anticipated to be due to the thermal effect that a slight increase in room temperature (due to warm bodies, laser power supply, computers, warming building in the sun) had on the optical path. As observed in literature, under pump radiation, a YAG crystal (such as Nd:YAG used here) will display a positive lens effect, which means the spot size reduces as the temperature of the rod increases [64]. However, the effect of increasing the heat rate into the system (higher repetition rate means higher heat rate, discussed in Section 7.8.3) showed the opposite, an increase in spot size, also indicated in Figure 7.2. The daily changes and variability of spot size were recorded and included in the power intensity uncertainty within each of the results.

The initial tests for displayed saturation of around 10 GW/cm^2, is supported by literature with 1064 nm [26, 5] and one source with 532 nm lasers, [28]. However for 532 nm, subsequent studies have demonstrated that saturation occurs earlier at 6 GW/cm^2 to 8 GW/cm^2 [27]. Before understanding this, and in the limited experimental time, a mid-point of laser capability of around 9 GW/cm^2 was chosen based solely on the mid-point of laser capability, and kept as the default power intensity during the geometry experiments. In hindsight, a more suitable default power intensity would be below 6 GW/cm^2.

In Figures 7.8 and 7.7, the true peak pressure values above 2130 kPa are attenuated by the presence of the inline clipper circuit, intended to limit the voltage to 10 V. The first implication of this (discussed in Section 7.1.3) is that the bubble lifetime measurement includes a temporal uncertainty of at most 1.2 μs. This contributes minimally to the overall uncertainty, as explained in Section 6.3.3.

The second implication is that any comparison between the peak pressure values of the laser induced shock wave and the bubble lifetimes (such as that in Figure 7.29) are only valid at pressures below 2130 kPa.

The third implication is that the transducer is potentially exposed to over-pressure values [69], which can introduce resonances into the waveform, shorten its serviceable lifetime or damage the internal piezoelectric element. Within this study, this may have occurred in Figure 7.6, but by virtue of the diagnostic itself, was quickly identified and remedied with a new transducer.

The transducer response, which as explained by Walter [77] in Section 6.4 as less than ideal, can still measure the medium to large cavitation bubble lifetimes found in LSP. This implies that the diagnostic technique here need not use (but can benefit from) specialised needle or fibre-optic hydrophones, and can accommodate cheaper transducers with a rise time of 1 μs.

8.3 Limitations

The growth and collapse of laser induced cavitation bubbles can be used as a diagnostic tool in LSP.

Strictly speaking, the primary limitation of this diagnostic is the measurable presence of laser induced cavitation bubbles, rather than the transfer of laser energy. Improving the efficiency or predictability of laser energy transfer to the target will not necessarily improve the diagnostic potential of the resulting cavitation bubbles. However, since the diagnostic cannot be separated from the practical limitations of submerged or thick water layer LSP, any improvements made in laser energy transfer leads to improved calibration, range and operation of the diagnostic itself.

If stagnant water is used, deionised water is the preferred confinement medium as the larger bubble size (and therefore higher laser energy transfer) in Figure 7.12 can attest. The transfer of laser energy is most greatly assisted, however, through replenishing the water along the beam path, more so than when using stagnant deionised water as the confinement medium.

This is evident when comparing bubble lifetimes in Figures 7.27 and 7.30: both the stability and magnitude of cavitation bubbles are significantly improved with flowing water.

The secondary limitation of this diagnostic is the sensitivity to changes in target geometry. Naturally, the laser energy transfer is reduced when some of the light completely misses the target surface. This is indeed confirmed by the rapid change in bubble lifetime in Figure 7.39 of the edge proximity experiment. This experiment also revealed the instability of cavitation bubbles near (within one bubble radius) an edge. This is a limitation if a per-shot diagnostic is needed for LSP treatment near or on an edge, but if the bubble instability and average values are used to identify proximity to the end of a work piece, such a characteristic could prove beneficial in a diagnostic.

LSP can be applied to intricate shapes beyond that of a simple flat geometry. Tomita et al. and Godwin et al. demonstrate that nearby geometry plays an important role in the behaviour of cavitation bubbles, particularly manner in which collapse occurs [39, 40]. As a consequence, the manner in which this diagnostic tool is affected by target geometries is explored in the final experiment. The common shapes found on turbine blades and gear teeth are simplified by round concave and convex diameters. Figure 7.46 illustrates that the effect these target shapes have on bubble lifetime is significant, the largest difference from a flat target being $+7.17\%$ and -9.08% on concave and convex shapes respectively.

An important assumption, that was not confirmed, was to show that laser-induced and bubble-collapse shock waves have similar speeds and shapes. It was assumed, for uncertainty calculations in Section 6.3.3, that the bubble collapse shock wave is half the speed of the laser induced shock wave - within the same cavitation bubble measurement. Comparing the first and second peaks in Figures 2.14, 2.19 and 2.20b as well as the aforementioned results in Section 7.1 however, the difference is at most half, confirming that this assumption is conservative. The true value of the shock wave velocity is difficult to obtain with the single transducer available to this project, but would be easily verified with two transducers separated by a known distance.

This investigation would have been improved if the shape, direction and strength (and corresponding speed) of the shock front could have all been validated and better understood using flow visualisations such as Schlieren photography or similar. With this understanding, the placement of the transducer may also be improved in future work. Further work should also include the testing of other aerospace target materials such as aluminium, magnesium and titanium alloys.

8.4 Findings

The stability and resulting sensitivity of bubble times as a diagnostic tool to monitor LSP is affected by the clarity of water in the beam path, whether the water was stagnant or flowing, target geometry, laser material interaction and changing repetition rate. The greatest changes were observed with water flow and target geometry.

In industrial applications, the investigated diagnostic tool may be limited to flat or predictable geometries that do not significantly change over the area being treated. A suitable application is the processing of large flat plates, such as those found in tanks and aeroplane panels.

Each application is likely to have unique geometry, shape or material. This means extensive calibration and understanding of how laser and flow variations affect bubble life time would be required before value adding peening takes place. For this reason, absolute measurements of localised laser energy cannot be correlated from bubble energy, only relative measurements within the process (on the same part, on the same day) can be made.

Thus, the growth and collapse of laser induced cavitation bubbles can be used on uniform targets as a useful diagnostic tool, and under the right conditions in the LSP process.

Contribution to Knowledge

The early preliminary experimental progress of this work was presented by Prof. C. Polese and was well received in the 2nd European Workshop on Laser Peening and Related Phenomena held in Hamburg between the 16th and 19th of September 2019 [79] as well as at the OSA Laser Congress, Laser Applications Conference held in Vienna between the 29th of September and 3rd of October 2019 [80].
This work was also intended for presentation at the International Conference of Laser Peening and Related Phenomena (ICLPRP) in China mid 2020, but was unfortunately postponed due to the COVID-19 global pandemic.

9 Conclusions

- An experimental test rig was successfully developed to measure pressure information, observe dynamic behaviour and evaluate laser induced cavitation bubbles.
- This test rig was able to demonstrate the effect of increasing delivered laser power intensity for a range of experimental conditions.
- The effect that target geometries (flat plates, concave channels and convex semi-cylinders with 5 mm to 10 mm radii) and flow regimes have to the behaviour (stability) of laser induced cavitation bubbles was determined.
- The output energy and spot size of the laser used here was affected by the laser pulse repetition rate.
- The time between successive shots (repetition rate) was critical to laser energy delivery if stagnant water was used. The effective laser energy transfer was highly dependent on sufficient time to restore beam path conditions between shots, and (in general) diminished with an increase in repetition rate.
- Flowing water along the beam path improved both the stability as well as the magnitude of the transferred energy, with a laser repetiton rate of up to 10 Hz.
- For flowing conditions, the power intensity at which bubble lifetime begins to saturate is around $6\,\mathrm{GW/cm^2}$.
- Greatest bubble lifetime stability across all power intensities was achieved with fixed repetition rate, constant tap water flow and uniform, flat target geometry.
- Cavitation bubbles offer a diagnostic potential that can operate within the limitations of thick water layer LSP.

10 | Recommendations

Much of the experimental shortfalls in this study could have been overcome with progressive cycles of experimentation, data review, and then experimentation with a revised method. In this study, due to a global pandemic limiting lab access, only one cycle of experimentation was performed leaving no room for further improvements.

Further investigation is recommended into the use of water flow to stabilise the thick water submerged LSP process. A quantitative flow rate investigation is required in order that the lower and upper limits of water velocity to ensure adequate clearing at a given laser repetition rate are found.

Further studies should be done to quantify the water requirements needed if the thick water peening with cavitation is to occur outside a contained tank, that is in a stream of water alone.

A comparative study between transducers should be made. This is to be carried out using the same transducer used in this study (PCB 113B21) alongside a transducer that is suited to the high pressure, short rise time requirements of cavitation measurements. One such suggestion is as a needle hydrophone and a fast digital oscilloscope. Using the same shock events in a single test tank, the output waveforms of either can be compared. In addition, rather than being controlled with separate computers, the laser, high speed camera and data acquisition systems should all be on a synchronised trigger with a known or specified delay. This would greatly improve repeatability of the results and simplify the measurement procedure.

While not the focus of this work, the effect that collapsing cavitation bubbles has on the residual stress below the metal surface should be explored. As the cavitation collapse occurs over a larger area than the initial laser spot (sometimes a cavitation cloud), there is a possibility that this may either relax or increase the residual stress in the spot.

References

[1] A S. Ribeiro, A L. L Silva, and A M. P. de Jesus. Evolution of the Fatigue History. In *21st Brazilian Congress of Mechanical Engineering*, pages 1–11, 2011.

[2] P. Peyre, R. Fabbro, P. Merrien, and H. P. Lieurade. Laser shock processing of aluminium alloys. Application to high cycle fatigue behaviour. *Materials Science and Engineering A*, 210(1-2):102–113, 1996. ISSN 09215093. doi: 10.1016/0921-5093(95)10084-9.

[3] P. Peyre and R. Fabbro. Laser shock processing: a review of the physics and applications. *Optical and Quantum Electronics*, 27(12):1213–1229, 1995. ISSN 03068919. URL https://www.researchgate.net/profile/Remy_Fabbro/publication/225219489_Laser_shock_processing_A_review_of_the_physics_and_applications/links/0c96052985e81f393a000000.pdf.

[4] Y. Sano, K. Akita, K. Masaki, Y. Ochi, I. Altenberger, and B. Scholtes. Laser peening without coating as a surface enhancement technology. *Journal of Laser Micro Nanoengineering*, 1(3):161–166, 2006. ISSN 18800688. doi: 10.2961/jlmn.2006.03.0002.

[5] R. Fabbro, P. Peyre, L. Berthe, and X. Scherpereel. Physics and applications of laser-shock processing. *Journal of Laser Applications*, 10(6):265–279, 1998. ISSN 1042-346X. doi: 10.2351/1.521861.

[6] C. Polese, D. Glaser, and R. Bedekar. Water Confinement Influences on the Laser Shock Peening process. *30th International Congress on High-Speed Imaging and Photonics*, 2012. URL https://www.researchgate.net/profile/Claudia_Polese2/publication/293645302_Water_Confinement_Influences_on_the_Laser_Shock_Peening_process/links/56ba0bcd08ae3b658a8a4179.pdf.

[7] D. Glaser and C. Polese. Cavitation bubble oscillation period as a process diagnostic during the laser shock peening process. *Applied Physics A: Materials Science and Processing*, 123(9):1–10, 2017. ISSN 14320630. doi: 10.1007/s00339-017-1209-6.

[8] D. C. van Aswegen and C. Polese. Experimental and analytical investigation of the effects of laser shock peening processing strategy on fatigue crack growth in thin 2024 aluminium alloy panels. *International Journal of Fatigue*, 142(September 2020):105969, 2021. ISSN 01421123. doi: 10.1016/j.ijfatigue.2020.105969.

[9] D. Glaser, C. Polese, R. D. Bedekar, J. Plaisier, S. Pityana, B. Masina, T. Mathebula, and E. Troiani. Laser shock peening on a 6056-t4 aluminium alloy for airframe applications. In *11th International Fatigue Congress*, volume 891 of *Advanced Materials Research*, pages 974–979. Trans Tech Publications Ltd, 5 2014. doi: 10.4028/www.scientific.net/AMR.891-892.974.

[10] S. N. van Staden, C.a Polese, D. Glaser, J. Nobre, A. M. Venter, D. Marais, J. Okasinksi, and J. Park. Measurement of residual stresses in different thicknesses of laser shock peened aluminium alloy samples. *Materials Research Proceedings*, 4:117–122, 4 2018. ISSN 2474-395X. doi: 10.21741/9781945291678-18.

[11] M. Newby, A. Steuwer, D. Glaser, and C. Polese. Synchrotron XRD Evaluation of Residual Stresses Introduced by Laser Shock Peening for Steam Turbine Blade Applications. *Materials Research Proceedings*, 4:97–102, 2018. doi: 10.21741/9781945291678-15.

[12] D. Glaser, C. Newby, M.and Polese, L. Berthe, and A. M. Venter. Evaluation of Residual Stresses Introduced by Laser Shock Peening in Steel using Different Measurement Techniques. *Mechanical Stress Evaluation by Neutron and Synchrotron Radiation*, 4:45–50, 2018. doi: 10.21741/9781945291678-7.

[13] P. Benicewicz, M. Azer, J. Deaton, P. Wu, and T. Rockstroh. Laser shock peening plasma diagnostics sensors for real-time process monitoring. *24th International Congress on Applications of Lasers and Electro-Optics, ICALEO 2005 - Congress ingings*, 1803: 844–850, 2005. doi: 10.2351/1.5060450.

[14] D. Glaser and C. Polese. System for and method of performing laser shock peening on a target with a fluid flow path sandwiched between a transparent to laser light solid medium and the target, April 2014. International Publication Number WO 2014/170868 A1.

[15] A. Kruusing. Shock Processing. In *Handbook of Liquids-Assisted Laser Processing*, pages 69–142. Elsevier, 2008. ISBN 9780080444987. doi: 10.1016/B978-008044498-7.50004-2.

[16] M. N. James, M. Newby, D. G. Hattingh, and A. Steuwer. Shot-peening of steam turbine blades: Residual stresses and their modification by fatigue cycling. *Procedia Engineering*, 2(1):441–451, 2010. ISSN 18777058. doi: 10.1016/j.proeng.2010.03.048.

[17] A. Rodríguez, L. N. López de Lacalle, A. Celaya, A. Lamikiz, and J. Albizuri. Surface improvement of shafts by the deep ball-burnishing technique. *Surface and Coatings Technology*, 206(11-12):2817–2824, 2012. ISSN 02578972. doi: 10.1016/j.surfcoat.2011.11.045.

[18] H. Soyama. Key Factors and Applications of Cavitation Peening. *International Journal of Peening Science and Technology*, 1(1):3–60, 2017. URL http://www.oldcitypublishing.com/wp-content/uploads/2017/11/IJPSTv1n1p3-60Soyama.pdf.

[19] S. Roy, J. W. Fisher, and B. T. Yen. Fatigue resistance of welded details enhanced by ultrasonic impact treatment (UIT). *International Journal of Fatigue*, 25(9-11):1239–1247, 2003. ISSN 01421123. doi: 10.1016/S0142-1123(03)00151-8.

[20] Y. Zhang, J. You, J. Lu, C. Cui, Y. Jiang, and X. Ren. Effects of laser shock processing on stress corrosion cracking susceptibility of AZ31B magnesium alloy. *Surface and Coatings Technology*, 204(24):3947–3953, 2010. ISSN 02578972. doi: 10.1016/j.surfcoat.2010.03.015.

[21] A. Gujba and M. Medraj. Laser Peening Process and Its Impact on Materials Properties in Comparison with Shot Peening and Ultrasonic Impact Peening. *Materials*, 7(12): 7925–7974, dec 2014. ISSN 1996-1944. doi: 10.3390/ma7127925.

[22] A. H. Clauer and D. F. Lahrman. Laser shock processing as a surface enhancement process. In *Durable Surfaces*, volume 197 of *Key Engineering Materials*, pages 121–144. Trans Tech Publications Ltd, 1 2001. doi: 10.4028/www.scientific.net/KEM.197.121.

[23] P. Peyre, L. Berthe, X. Scherpereel, and R. Fabbro. Laser-shock processing of aluminium-coated 55C1 steel in water-confinement regime, characterization and application to high-cycle fatigue behaviour. *Journal of Materials Science*, 33(6):1421–1429, 1998. ISSN 00222461. doi: 10.1023/A:1004331205389.

[24] X. Hong, S. Wang, D. Guo, H. Wu, J. Wang, Y. Dai, X. Xia, and Y. Xie. Confining medium and absorptive overlay: Their effects on a laser-induced shock wave. *Optics and Lasers in Engineering*, 29(6):447–455, 1998. ISSN 01438166. doi: 10.1016/S0143-8166(98)80012-2.

[25] J. Cao, J. Zhang, Y. Hua, R. Chen, and Y. Ye. Journal of Materials Processing Technology Improving the high temperature oxidation resistance of Ni-based superalloy GH202 induced by laser shock processing. *Journal of Materials Processing Tech.*, 243:31–39, 2017. ISSN 0924-0136. doi: 10.1016/j.jmatprotec.2016.11.040.

[26] L. Berthe, R. Fabbro, P. Peyre, L. Tollier, and E. Bartnicki. Shock waves from a water-confined laser-generated plasma. *Journal of Applied Physics*, 82(6):2826–2832, 1997. ISSN 00218979. doi: 10.1063/1.366113.

[27] L. Berthe, D. Courapied, S. El karnighi, P. Peyre, C. Gorny, and Y. Rouchausse. Study of laser interaction in water flow confinement at high repetition rate. *Journal of Laser Applications*, 29(4):042006, 2017. ISSN 1042-346X. doi: 10.2351/1.5007947.

[28] M. Enoki, K. Kobayashi, and T. Takata. Quantitative Acoustic Emission Measurement of Laser Peening. *30th European Conference on Acoustic Emission Testing and 7th International Conference on Acoustic Emission*, 1(September):12–15, 2012. URL http://212.8.206.21/article/ewgae2012/content/papers/62_Enoki_Rev1.pdf.

[29] A. Sollier, L. Berthe, and R. Fabbro. Numerical modeling of the transmission of breakdown plasma generated in water during laser shock processing. *The European Physical Journal Applied Physics*, 16(2):131–139, nov 2001. ISSN 1286-0042. doi: 10.1051/epjap:2001202.

[30] J. Noack, D. X. Hammer, G. D. Noojin, B. A. Rockwell, and A. Vogel. Influence of pulse duration on mechanical effects after laser-induced breakdown in water. *Journal of Applied Physics*, 83(12):7488–7495, 1998. ISSN 00218979. doi: 10.1063/1.367512.

[31] L. Berthe, R. Fabbro, P. Peyre, and E. Bartnicki. Wavelength dependent of laser shockwave generation in the water-confinement regime. *Journal of Applied Physics*, 85(11): 7552–7555, 1999. ISSN 00218979. doi: 10.1063/1.370553.

[32] C. E. Brennen. *Cavitation and Bubble Dynamics*. Oxford University Press, 1995. ISBN 0-19-509409-3.

[33] M. C.Potter, D. C. Wiggert, and B. Ramadan. *Mechanics of Fluids*. Global Engineering, 4 edition, 2012. ISBN 978149062036.

[34] R. E. A. Arndt, V. H. Arakeri, and H. Higuchi. Some observations of tip-vortex cavitation. *Journal of Fluid Mechanics*, 229:269–289, 1991. doi: 10.1017/S0022112091003026.

[35] A. Vogel, S. Busch, and U. Parlitz. Shock wave emission and cavitation bubble generation by picosecond and nanosecond optical breakdown in water. *The Journal of the Acoustical Society of America*, 100(1):148–165, 1996. ISSN 0001-4966. doi: 10.1121/1.415878.

[36] T. T. P. Nguyen, R. Tanabe-Yamagishi, and Y. Ito. Effects of liquid depth on the expansion and collapse of a hemispherical cavitation bubble induced in nanosecond pulsed laser ablation of a solid in liquid. *Optics and Lasers in Engineering*, 126(October 2019): 105937, 2020. ISSN 01438166. doi: 10.1016/j.optlaseng.2019.105937.

[37] T. Takata, M. Enoki, P. Chivavibul, A. Matsui, and Y. Kobayashi. Effect of confinement layer on laser ablation and cavitation bubble during laser shock peening. *Materials Transactions*, 57(10):1776–1783, 2016. ISSN 13459678. doi: 10.2320/matertrans.M2016150.

[38] P. K. Kennedy, D. X. Hammer, and B. A. Rockwell. Laser-induced breakdown in aqueous media. *Progress in Quantum Electronics*, 21(3):155–248, jan 1997. ISSN 00796727. doi: 10.1016/S0079-6727(97)00002-5.

[39] R. P. Godwin, E. J. Chapyak, J. Noack, and A. Vogel. Aspherical bubble dynamics and oscillation times. In *Proceedings of Laser-Tissue Interaction X*, 1999. doi: 10.1117/12.350042.

[40] Y. Tomita, P. B. Robinson, R. P. Tong, and J. R. Blake. Growth and collapse of cavitation bubbles near a curved rigid boundary. *Journal of Fluid Mechanics*, 466:259–283, 2002. ISSN 00221120. doi: 10.1017/S0022112002001209.

[41] C. F. Delale. *Bubble dynamics and shock waves.* Springer-Verlag Berlin Heidelberg, 2013. ISBN 9783642342974. doi: 10.1007/978-3-642-34297-4.

[42] C. E. Bell and J. A. Landt. Laser-induced high-pressure shock waves in water. *Applied Physics Letters*, 10(2):46–48, 1967. ISSN 00036951. doi: 10.1063/1.1754840.

[43] A. Vogeland and W. Lauterborn. Acoustic transient generation by laser-produced cavitation bubbles near solid boundaries. *Journal of the Acoustical Society of America*, 1988. ISSN NA. doi: 10.1121/1.396852.

[44] A. Vogel, J. Noack, K. Nahen, D. Theisen, S. Busch, U. Parlitz, D. X. Hammer, G. D. Noojin, B. A. Rockwell, and R. Birngruber. Energy balance of optical breakdown in water at nanosecond to femtosecond time scales. *Applied Physics B: Lasers and Optics*, 68(2):271–280, 1999. ISSN 09462171. doi: 10.1007/s003400050617.

[45] R. Somers, M. Winiarz, and J. D. Risbeck. Laser shock peening quality assurance by volumetric analysis of laser shock peened dimple, 1999. US Patent 5948293.

[46] S. Mannava, W. D. Cowie, P. K. Wright, and R. D. McClain. Method of monitoring and controlling laser shock peening using an in plane deflection test coupon, 1999. US Patent 5951790.

[47] T. J. Rockstroh and W. D. Scheidt. Holographic interferometry for monitoring and controlling laser shock peening, 2000. US Patent 6094260.

[48] M. E. O'Loughlin, A. H. Clauer, D. W. Sokol, J. L. Dulaney, and S. M. Toller. Quality control for laser peening, 2003. US Patent US6512584B1.

[49] U. W. Suh and J. D. Risbeck. Laser shock peening quality assurance by acoustic analysis, 2003. US Patent US6629464B2.

[50] B. M. Davis, R. D. McClain, U. W. Suh, and S. R. Mannava. Real time laser shock peening quality assurance by natural frequency analysis, 2002. US Patent US6914215B2.

[51] J. B. Deaton, M.N. Azer, D. E. Williams, M. S. Bailey, M. A. Foister, M. Paul, and J. J. West. System and method for controlling laser shock peening, 2010. US Patent US7816622B2.

[52] M. Mathai and G. Della-Fera. Laser shock peening measurement systemand method, 2013. US Patent US8520470B2.

[53] R. L. Trantow and U. W. Suh. Method for monitoring and controlling laser shock peening using temporal light spectrum analysis, 2000. US Patent 6075593.

[54] D. W. Sokol, C. T. Walters, H. M. Epstein, A. H. Clauer, J. L. Dulaney, and Mark O'Loughlin. Quality control plasma monitor for laser shock processing, 2001. US Patent US6254703B1.

[55] D. W. Sokol, C. T. Walters, H. M. Epstein, A. H. Clauer, J. L. Dulaney, and Mark O'Loughlin. Quality control plasma monitor for laser shock processing, 2003. US Patent US6554921B2.

[56] P. P. Wu, P. K. Benicewicz, and M. N. Azer. System and method for monitoring laser shock processing, 2007. US Patent US7273998B2.

[57] C. B. Dane, E. W. H. Lao, and S. N. Fochs. Polarization compensated beam spltter and dagnostic system for highpower laser systems, 2014. US Patent US8810792B2.

[58] R. E. Warren and P. R. Staver. Monitored laser shock peening, 2006. US Patent US7148448B2.

[59] J. B. Deaton, F. H. Azad, M.N. Azer, and T. J. Rockstroh. Laser shock peening system with time-of-flight monitoring, 2011. US Patent US7906746B2.

[60] U. W. Suh and J. D. Risbeck. Laser shock peening quality assurance by acoustic analysis, October 7 2003. US Patent 6,629,464.

[61] T. Takata, M. Enoki, P. Chivavibul, A. Matsui, and Y. Kobayashi. Acoustic emission monitoring of laser shock peening by detection of underwater acoustic wave. *Materials Transactions*, 57(5):674–680, 2016. doi: 10.2320/matertrans.M2015401.

[62] Y. Zhang, J. Lu, and K. Luo. *Laser Shock Processing of FCC Metals*, volume 179 of *Springer Series in Materials Science*. Springer Berlin Heidelberg, Berlin, Heidelberg, 2013. ISBN 978-3-642-35673-5. doi: 10.1007/978-3-642-35674-2.

[63] Thales Group. Saga HP, 2015. URL https://www.thalesgroup.com/sites/default/files/database/d7/asset/document/thales_fiche_saga_25.03.15_medres_pour_web.pdf. Accessed 30 January 2019.

[64] W. Koechner. Thermal lensing in a Nd:YAG laser rod. *Appl. Opt.*, 9(11):2548–2553, Nov 1970. doi: 10.1364/AO.9.002548.

[65] Coherent Inc. Fieldmaxii-p user manual, 2014. URL https://www.coherent.com/assets/pdf/FieldMaxII-P-Quick-Start-Guide_FORMFIRST.pdf. Accessed 07 July 2020.

[66] MakeItFrom.com. Half-hard 304 stainless steel, 2020. URL https://www.makeitfrom.com/material-properties/Half-Hard-304-Stainless-Steel. Accessed 24 September 2020.

[67] AMS B Finishes Processes and Fluids Committee . Laser peening, 2020. doi: https://doi.org/10.4271/AMS2546A. Accessed 21 September 2020.

[68] DIY Electronics. Creality cr-20 pro 3d printer, 2020. URL https://www.diyelectronics.co.za/store/8741-thickbox_default/creality-cr-20-pro-3d-printer.jpg. Accessed 31 July 2020.

[69] PCB. 113B21, 2016. URL https://www.pcbpiezotronics.fr/produit/capteurs-de-pression/113b21/. Accessed 25 April 2018.

[70] Wayne Storr. Diode clipping circuits, 2014. URL https://www.electronics-tutorials.ws/diode/diode-clipping-circuits.html. Accessed 11 September 2020.

[71] Thermofisher. Orion Star ™A212 Conductivity Benchtop Meter, 2020. URL https://www.thermofisher.com/order/catalog/product/STARA2126#/STARA2126. Accessed 30 September 2020.

[72] Optek-Danulat Inc. Conductivity basics, 2020. URL https://www.optek.com/en/conductivity-basics.asp. Accessed 22 August 2020.

[73] J. Hokanson. TDMS reader, 2018. URL https://uk.mathworks.com/matlabcentral/fileexchange/30023-tdms-reader. Accessed 12 February 2019.

[74] MATLAB. *Version 9.2.0.959691 (R2017a)*. The MathWorks Inc., Natick, Massachusetts, 2017.

[75] R. S. Figliola and D. E. Beasley. *Theory and Design for Mechanical Measurements*. John Wiley & Sons Inc., 4 edition, 2006. ISBN 0471445932.

[76] L. F. Chaparro. Chapter 7 - Sampling Theory. In *Signals and Systems using MATLAB*, pages 419 – 449. Academic Press, Boston, 2011. ISBN 978-0-12-374716-7. doi: https://doi.org/10.1016/B978-0-12-374716-7.00011-9.

[77] P. L. Walter. Shock and Blast Measurement - Rise Time Capability of Measurement Systems. *Piezotronics, PCB*, Measurement(Technical Note), 2019. URL https://www.pcb.com/contentstore/MktgContent/linkeddocuments/technotes/TN-11-0904_Calculating_Rise_Time.pdf.

[78] D. C. Montgomery and G. C. Runger. *Applied Statistics and Probability for Engineers*. John Wiley & Sons, 6 edition, 2014. ISBN 9781118744123.

[79] C. Polese, D. Glaser, and N. J. Stiekema. The Heartbeat of Laser Shock Processing. In *2nd European Workshop on Laser Peening and Related Phenomena*, 2019. (Invited Speaker).

[80] C. Polese, D. Glaser, and N. J. Stiekema. The South African Heartbeat of Laser Shock Peening. In *OSA Laser Congress, Laser Applications Conference*, 2019. (Invited Speaker).

[81] Engineering ToolBox. Water - density, specific weight and thermal expansion coefficient, 2003. URL https://www.engineeringtoolbox.com/water-density-specific-weight-d_595.html. Accessed 09 January 2021.

[82] Engineering ToolBox. Water - saturation pressure, 2004. URL https://www.engineeringtoolbox.com/water-vapor-saturation-pressure-d_599.html. Accessed 09 January 2021.

[83] Weather Underground. Lynwood - ipretori51, 2020. URL https://www.wunderground.com/dashboard/pws/IPRETORI51/table/2020-01-23/2020-01-23/monthly. Accessed 09 January 2021.

A | Appendix

A.1 Data Acquisition Uncertainty Analysis

The details of the Design Stage uncertainty outlined in Section 6.3.1 are documented here.

$$U_d = \sqrt{(U_0)^2 + (U_c)^2} \tag{A.1}$$

The typical accuracy values were chosen in Table A.1.

Table A.1: Specification of data acquisition

Specification	Value
DC gain accuracy	±0.32% calibrated
DC offset accuracy	±0.08% calibrated
Resolution	14 bits ⇒ 2^{14}, for 10 V range: $\frac{10}{2^{14}}$ V
Usual input range	7.5 V for pressure, 0.6 V for energy.

$$\Delta DAQ = \sqrt{(U_0)^2 + (U_c)^2}$$

For the data acquisition device, with a 10 V maximum input, the interpolation error $(U_0)_v$ is the resolution and the instrument error $(U_c)_v$ is the accuracy:

$$(U_0)_v = \frac{10}{2^{14}} = 0.000610352\,\text{V}$$
$$(U_c)_{v1} = \sqrt{(0.0032 \times 7.5)^2 + (0.0008 \times 7.5)^2} = 0.02473863375\,\text{V}$$

The design stage uncertainty for the transducer channel ($v1$) of the data acquisition device is

$$(U_d)_{v1} = \sqrt{((U_0)_v)^2 + ((U_c)_{v1})^2}$$
$$= \sqrt{((0.000610352)^2 + (0.02473863375)^2} = 0.02474616192\,\text{V}$$

Similarly with a 0.6 V input (around 900 mJ), the design stage uncertainty for the energy meter channel ($v2$):

$$(U_c)_{v2} = \sqrt{(0.0032 \times 0.6)^2 + (0.0008 \times 0.6)^2} = 0.0019790907\,\text{V}$$

$$(U_d)_{v2} = \sqrt{((U_0)_v)^2 + ((U_c)_{v2})^2}$$
$$= 0.002071069667\,\text{V}$$

Table A.2: Energy meter specifications

Specification	Value
Analogue Output Voltage Accuracy	$\pm 1.0\%$ of $0.6\,\text{V}$
Listed Uncertainty	$\pm 1.0\%$
Resolution	0.1% of full scale
Full scale output	$0.6\,\text{V}$

A.1.1 Laser Energy Uncertainty

For the specified conditions in Table A.2, the interpolation error $(U_0)_{Ed}$ is the resolution over this scale and the instrument error $(U_c)_{Ed}$ is the accuracy:

$$(U_0)_{Ed} = 0.1\% \times 0.6\,\text{V} = 0.0006\,\text{V}$$
$$(U_c)_{Ed} = 1\% \times 0.6\,\text{V} = 0.006\,\text{V}$$

The design stage uncertainty for the energy meter display (Ed) is

$$\begin{aligned}(U_d)_{Ed} &= \sqrt{((U_0)_{Ed})^2 + ((U_c)_{Ed})^2} \\ &= \sqrt{(0.0006)^2 + (0.006)^2} = 0.006029925373\,\text{V}\end{aligned}$$

Pyroelectric sensor:

Table A.3: Specification of pyroelectric sensor

Specification	Value
Listed uncertainty	$\pm 2\%$
Linearity	$\pm 3\%$
Max Energy density	assume $0.5\,\text{J/cm}^2$

$$(U_0)_{Es} = 0$$
$$(U_c)_{Es} = \sqrt{(0.02 \times 0.5)^2 + (0.03 \times 0.5)^2} = 0.018028\,\text{J}$$

The energy scale most used is $3\,\text{J}$. Converting to voltage using the relationship as defined by Coherent Inc. in Equation 4.1:

$$V_{out} = E_{laser}\frac{V_{scale}}{E_{scale}} = 0.018028\,\text{J} \times \frac{2\,\text{V}}{3\,\text{J}}$$
$$\therefore\ (U_c)_{Es} = 0.0120185\,\text{V}$$

As it is an analogue device, the resolution of the pyroelectric sensor is considered negligible.

$$\therefore \; (U_0)_{Es} = 0$$

The design stage uncertainty for the energy meter sensor (Es) is

$$\begin{aligned}(U_d)_{Es} &= \sqrt{((U_0)_{Es})^2 + ((U_c)_{Es})^2} \\ &= \sqrt{0 + (0.0120185)^2} \qquad = 0.0120185\,\text{V}\end{aligned}$$

Complete meter uncertainty;

$$\begin{aligned}(U_d)_E &= \sqrt{((U_d)_{Ed})^2 + ((U_d)_{Es})^2} \\ &= \sqrt{(0.0120185)^2 + (0.006029925373)^2} \qquad = 0.01344635052\,\text{V}\end{aligned}$$

Because the energy meter voltage is measured with the DAQ, the uncertainty of the final laser energy measurement is:

$$\begin{aligned}(U_d)_{LaserEnergy} &= \sqrt{((U_d)_E)^2 + ((U_d)_{v2})^2} \\ &= \sqrt{(0.002071069667)^2 + (0.01344635052)^2} \\ &= 0.01360491352\,\text{V} = \mathbf{0.0204}\,\text{J}\end{aligned}$$

A.1.2 Uncertainty of Pressure Transducer

Table A.4: Specification of pressure transducer

Specification	Value
Linearity error	1% of full scale
Resolution	0.007 kPa or 0.0000252 V
Full scale output	7.2 V
Sesitivity (±15%)	3.6 mV/kPa

$$\begin{aligned}(U_0)_{tr} &= 25.2 \times 10^{-6}\,\text{V} \\ (U_c)_{tr} &= 0.01 \times 7.2 = 0.072\,\text{V}\end{aligned}$$

The design stage uncertainty for the transducer itself (tr) is

$$\begin{aligned}(U_d)_{tr} &= \sqrt{((U_0)_{tr})^2 + ((U_c)_{tr})^2} \\ &= \sqrt{(25.2 \times 10^{-6})^2 + (0.01 \times 7.2)^2} = 0.072000004\,\text{V}\end{aligned}$$

Because the pressure voltage is measured with the DAQ, the final uncertainty is:

$$\begin{aligned}(U_d)_{Pressure} &= \sqrt{((U_d)_{tr})^2 + ((U_d)_{v1})^2} &&= \sqrt{(0.072000004)^2 + (0.02474616192)^2} \\ &= 0.07613391561\,\text{V} \div 3.6\,\text{mV/kPa} &&= \mathbf{21.148}\,\text{kPa}\end{aligned}$$

A.1.3 Sequential Perturbation

When the equation describing a response is complicated or the inputs are difficult to verify analytically, the perturbation technique is a useful method of determining uncertainty around an operating point. In summary, it is sequentially changing or perturbing each of the contributing variables by the magnitude of their individual uncertainties. All other variables are constant at a reasonable set point. The effect of each perturbation on the larger equation is then squared, summed and square root taken to produce an overall uncertainty. [78].

Using reasonable input values for each of the independent variables $x_1,\ x_2,\ \ldots$, the resultant operating point R_0 is found

$$R_0 = f\{x_1,\ x_2,\ \ldots x_L\} \tag{A.2}$$

Each of the independent variables are separately increased by their respective uncertainties $x_i + u_{xi}$. The result R_i^+ is recalculated for each of these changes. If the variable is not altered, it is kept at the original operating point value:

$$\begin{aligned}R_1^+ &= f\{x_1 + u_{x1},\ x_2,\ \ldots x_L\}, \\ R_2^+ &= f\{x_1,\ x_2 + u_{x2},\ \ldots x_L\}, \\ &\ldots \\ R_L^+ &= f\{x_1,\ x_2,\ \ldots x_L + u_{xL}\}\end{aligned}$$

Similarly, the result R_i^- is recalculated for each independent variable reduced by their uncertainty, $x_i - u_{xi}$.

The difference is then calculated:

$$\begin{aligned}\delta R_i^+ &= R_i^+ - R_0 \\ \delta R_i^- &= R_i^- - R_0\end{aligned}$$

An average magnitude is taken as the uncertainty contribution of each independent variable

$$\delta R_i = \frac{\delta R_i^+ - \delta R_i^-}{2} \approx \theta_i u_i$$

The final uncertainty result is

$$u_R = \left[\sum_{i=1}^{L}(\delta R_i)^2\right]^{\frac{1}{2}}$$

A.1.4 Sequential Perturbation of Bubble Energy

A good candidate for sequential perturbation analysis is the uncertainty of the bubble energy for a given bubble lifetime. To determine this uncertainty u_R, Table A.6 documents the case for a single operating point or bubble lifetime.

The terms in the bubble energy equation are each assessed for their contribution to the perturbation uncertainty evaluation:

$$R_0 = \frac{\left(P_{0_{day}} - Pv_{temp}\right)^{\frac{5}{2}}}{\left(1.43031(\rho_{temp})^{\frac{1}{2}}\right)^3}\tau_b^3$$

The bubble time uncertainty τ_b is a function of three changes $\tau_{b_{velocity}}$, $\tau_{b_{peak}}$, $\tau_{b_{movement}}$.

If the speed of the laser induced shock wave differs to the speed of the cavitation induced shock wave, the true uncertainty of the bubble lifetime will need to include this difference and its variability. If the two shocks differed by a factor of 2 (waves at Mach 0.5 and Mach 1), the time delay between them over 20 mm is $u\tau_{b_{velocity}} = 0.02/740.5 - 0.02/(1481) = 13.504\,\mu$s at 20°C. The time difference between two shock waves over the distance to the laser site is three orders of magnitude less than the bubble lifetimes studied here, but still contributes to the overall uncertainty. It is understood that by the time the shock wave reached the transducer, its shape may been disturbed as the waveform in Figure 7.5 indicated. The effect of this disruption was not quantified however.

The peak detection uncertainty is governed by the transducer uncertainty as well as the proximity of nearby points within that uncertainty range. Peak detection is evaluated in Section 7.1.4 and was found to be $u\tau_{b_{peak}} = 1.20\,\mu$s.

If the transducer were to move a full 20 mm between the first and the second shock wave, assuming a Mach 1 shock speed at 20°C, the uncertainty of measuring the second shock wave after the transducer movement is $u\tau_{b_{movement}} = \frac{0.02}{1481} = 13.504\,\mu$s. In reality, from the high speed images, the movement of the transducer is around 0.03 mm, making this uncertainty very conservative.

A temperature change would affect uncertainties associated with density and vapour pressures that make up the constant term in Equation 2.6. These can be readily obtained from the properties of water at the given temperatures. The conservative difference between 20°C and 30°C results is a density change of $u\rho_{temp} = (998.2067 - 995.6488) = 2.5579\,\text{kg/m}^3$ [81]. The same temperature difference results in a vapour pressure change of $uPv_{temp} = (4247 - 2339.3) = 1907.7\,\text{Pa}$ [82].

The pressure variation for the location of the lab was found [83]. The standard deviation over the course of test month is taken as the uncertainty of the atmospheric static pressure. $uP_{0_{day}} = 2.06 \cdot 10^3\,\text{Pa}$.

Table A.5: Each individual uncertainty u_i.

Term	u_i	
$\tau_{b_{velocity}}$	$1.35 \cdot 10^{-5}$	[s]
$\tau_{b_{peak}}$	$1.20 \cdot 10^{-6}$	[s]
$\tau_{b_{movement}}$	$1.35 \cdot 10^{-5}$	[s]
ρ_{temp}	2.56	[kg/m^3]
Pv_{temp}	$1.91 \cdot 10^{+3}$	[Pa]
$P_{0_{day}}$	$2.06 \cdot 10^{+3}$	[Pa]

With a 1.0 ms bubble lifetime and independent variables fixed at the values x_i (also found in Table A.6), this bubble's energy from (Equation 2.6) is:

$$\begin{aligned} R_0 &= \frac{\left(P_{0_{day}} - Pv_{temp}\right)^{\frac{5}{2}}}{\left(1.43031(\rho_{temp})^{\frac{1}{2}}\right)^3}\,\tau_b^3 \\ &= 15.019 \times 10^{-3} \pm u_R \;\; \text{J} \end{aligned} \tag{A.3}$$

The rest of the steps are done colummn-wise in Table A.6.

Table A.6: Example using the sequential perturbation technique to obtain the uncertainty at a single operating point.

Operating Point: Bubble lifetime $\tau_b = 1\,\text{ms} \implies R_0 = 15.019 \times 10^{-3}$ J								
	x_i	u_i	R_i^+	R_i^-	δR_i^+	δR_i^-	δR_i	$(\delta R_i)^2$
$\tau_{b_{velocity}}$	$1.00 \cdot 10^{-3}$	$1.35 \cdot 10^{-5}$	$1.56 \cdot 10^{-2}$	$1.44 \cdot 10^{-2}$	$6.17 \cdot 10^{-04}$	$-6.00 \cdot 10^{-4}$	$6.09 \cdot 10^{-4}$	$3.70 \cdot 10^{-7}$
$\tau_{b_{peak}}$	$1.00 \cdot 10^{-3}$	$1.20 \cdot 10^{-6}$	$1.51 \cdot 10^{-2}$	$1.50 \cdot 10^{-2}$	$5.41 \cdot 10^{-05}$	$-5.40 \cdot 10^{-5}$	$5.41 \cdot 10^{-5}$	$2.92 \cdot 10^{-9}$
$\tau_{b_{movement}}$	$1.00 \cdot 10^{-3}$	$1.35 \cdot 10^{-5}$	$1.50 \cdot 10^{-2}$	$1.50 \cdot 10^{-2}$	$9.45 \cdot 10^{-06}$	$-9.44 \cdot 10^{-6}$	$9.45 \cdot 10^{-6}$	$8.92 \cdot 10^{-11}$
ρ_{temp}	$9.98 \cdot 10^{2}$	2.56	$1.50 \cdot 10^{-2}$	$1.51 \cdot 10^{-2}$	$-5.75 \cdot 10^{-05}$	$5.79 \cdot 10^{-5}$	$-5.77 \cdot 10^{-5}$	$3.33 \cdot 10^{-9}$
Pv_{temp}	$2.33 \cdot 10^{3}$	$1.91 \cdot 10^{3}$	$1.42 \cdot 10^{-2}$	$1.59 \cdot 10^{-2}$	$-8.32 \cdot 10^{-04}$	$8.60 \cdot 10^{-4}$	$-8.46 \cdot 10^{-4}$	$7.16 \cdot 10^{-7}$
$P_{0_{day}}$	$8.70 \cdot 10^{4}$	$2.06 \cdot 10^{3}$	$1.59 \cdot 10^{-2}$	$1.41 \cdot 10^{-2}$	$9.29 \cdot 10^{-04}$	$-8.95 \cdot 10^{-4}$	$9.12 \cdot 10^{-4}$	$8.32 \cdot 10^{-7}$
$\therefore$ Uncertainty $u_R = \left[\sum_{i=1}^{L}(\delta R_i)^2\right]^{\frac{1}{2}}$ $u_R = 1.387 \times 10^{-3}$ J								

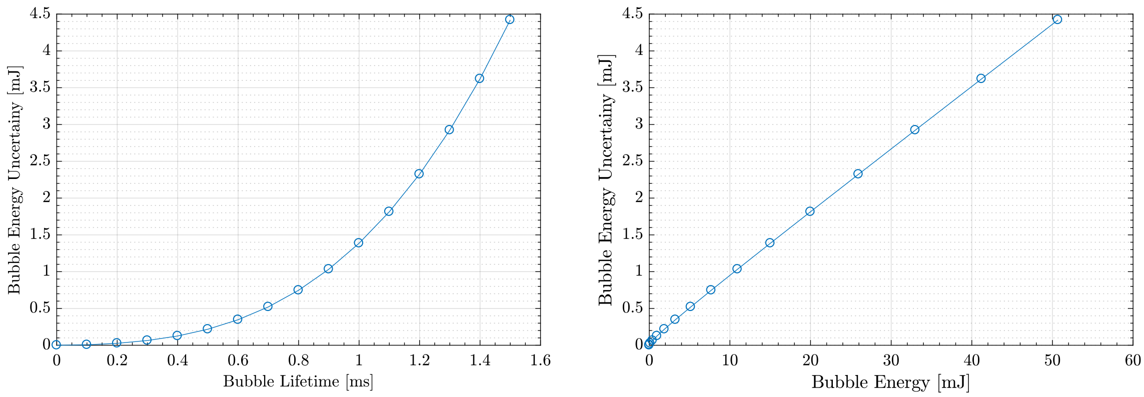

(a) E_b Uncertainty vs τ_b **(b)** E_b Uncertainty vs E_b

Figure A.1: This study produced bubble lifetimes not larger than 1.6 ms.

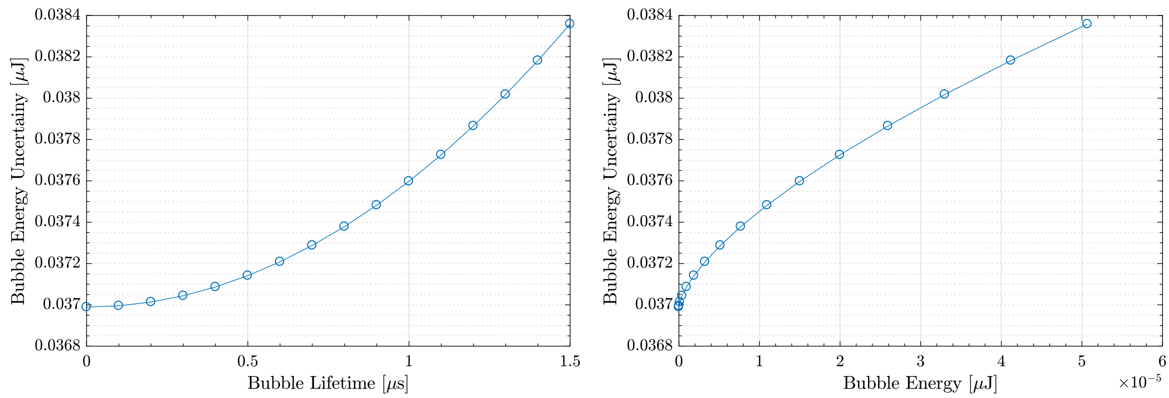

(a) E_b Uncertainty vs τ_b **(b)** E_b Uncertainty vs E_b

Figure A.2: The behaviour of bubble energy uncertainty with tiny bubbles.

Thus, the energy of a 1 ms bubble is

$$R_0 = (15.019 \pm 1.387) \times 10^{-3}\,\text{J}$$

For varying operating points, the uncertainty changes. Figure A.1a shows how the uncertainty of bubble energy increases with larger bubbles, a linear relationship to the magnitude of bubble energy in Figure A.1b.

If the operating point is moved to much smaller bubbles the relationship between bubble energy and bubble energy uncertainty becomes nonlinear, shown in Figure A.2b. This is due to the bubble lifetime approaching the same order of magnitude and having less of an effect than the other terms (Pv_{temp}, ρ_{temp},...) within the bubble energy uncertainty in Equation A.3.

A.2 Marlin Firmware Modifications

These minor modifications enabled the Creality CR20 Pro 3D printer to be used as a sample articulation stage for the LSP experiments. The C++ and header files that were modified within the "CR-20 Pro1.1.6BLTouchV3PowerLossContinueEnglishandChinese.rar" firmware are:

Marlin/Configuration.h:

```
#define STRING_CONFIG_H_AUTHOR "(Wits)" // Who made the changes.
#define SHOW_BOOTSCREEN
#define STRING_SPLASH_LINE1 DETAILED_BUILD_VERSION // will be
// shown during bootup in line 1

//#define Z_MIN_PROBE_USES_Z_MIN_ENDSTOP_PIN //Wits commented

#define PROBE_MANUALLY // Wits uncommented

#define DISABLE_Y true //Wits changed to true

#define INVERT_X_DIR true  //Wits reversed this because the
// x_axis motor was turned upsidedown.

#define X_BED_SIZE 148   //Wits X_axis size due to tank

#define Z_MAX_POS 60  //Wits new Z axis size due to tank

//#define AUTO_BED_LEVELING_BILINEAR //Wits commented
//#define AUTO_BED_LEVELING_UBL
#define MESH_BED_LEVELING //Wits uncommented

#define LCD_BED_LEVELING ///Wits uncommented
```

Marlin/language.h:

```
#define MSG_DETAILED_BUILD_VERSION          "Wits LSP CNC"
```

```
251 #define MSG_WEBSITE_URL                         "www.wits.ac.za"
```

Marlin/Marlin_main.cpp:

```
3914 //Wits commented:
3915 // if (!axis_known_position[X_AXIS] || !axis_known_position[Y_AXIS]) {
3916 //Wits replaced with removed Yaxis condition:
3917 if (!axis_known_position[X_AXIS]) {
```

```
9652 //        if (WITHIN(diff, -20, 20)) { //Wits commented
9653 //Wits modified to carefully allow for greater Zaxis offset distances:
9654 if (WITHIN(diff, -100, 100)) {
```

Marlin/SanityCheck.h:

```
812 //Wits commented:
813 //#if ENABLED(DISABLE_X) || ENABLED(DISABLE_Y) || ENABLED(DISABLE_Z)
814 //Wits removed Yaxis dependent condition:
815 #if ENABLED(DISABLE_X) || ENABLED(DISABLE_Z)
```

Marlin/ultralcd.cpp:

```
2655 // Wits commented:
2656 //  enqueue_and_echo_commands_P(PSTR("G92 X0 Y0 Z0")); // move all axis home
2657 enqueue_and_echo_commands_P(PSTR("G92 Y0")); // Zero Y axis home // Wits
2658 enqueue_and_echo_commands_P(PSTR("G28")); // move all axis homed
```

```
2686 // Auto Home
2687 // Wits rewritten to manually zero Yaxis if required
2688 // MENU_ITEM(gcode, msg_auto_home(), PSTR("G28")); //Wits commented
2689 MENU_ITEM(function, msg_auto_home(), lcd_autohome);
2690 #if ENABLED(INDIVIDUAL_AXIS_HOMING_MENU)
2691 MENU_ITEM(gcode, msg_auto_home_x(), PSTR("G28 X"));
2692 MENU_ITEM(gcode, msg_zero_y(), PSTR("G92 Y0")); //Wits modified
2693 MENU_ITEM(gcode, msg_auto_home_z(), PSTR("G28 Z"));
```

A.3 GCODE Run on the 3D Printer

Below is an example of the GCODE that was run to move the stage back and forth during the curvature tests. For longer tests the GCODE moved in a raster pattern seen in Figure A.3. Another example of GCODE is found attached 1mmVerticalLSP.gcode.

```
G21 ; Set units to mm
;G90 ; Absolute positioning
G28 X0 Z0 ;Home
G92 X0 Z0 ;specify that the nozzles current XYZ position is 0, 0, 0
;Put printing message on LCD screen
M117 Rastering...
M106 S255 ;fan on
G1 Z13.4 F300
G1 X-6+ F300
G92 X0 Z0 ;specify that the nozzles current XYZ position is 0, 0, 0
;Extrude to rotate round
;G1 F200 E3000
G1 X8.5 F300;  ----
G1 Z0.000 F0;      |
G1 X11.5 F30;      |---- These steps are repeated as long as needed
G1 X8.5 F30;       |
G1 X11.5 F30;  ----
M107 S255 ;fan off
G1 X0 Z0 F720
```

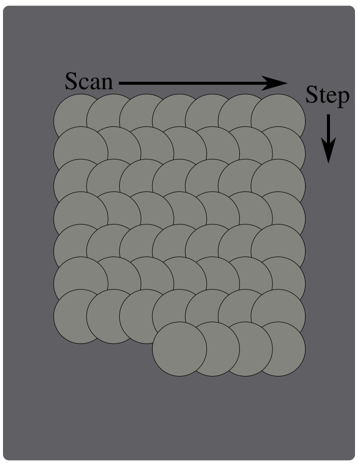

Figure A.3: GCODE raster scanning pattern.

A.4 MATLAB Scripts

The findpeaks built-in function which enabled reliable peak detection is attached findpeaks.m.

In addition, attached are the MATLAB scripts written to aid this study:

LSP_TDMS.m

PlottingFuncLSP.m

SpotSizeLookup.m

EnergyToPI.m

BubbleEnergyLSP.m

LSPStats.m

LSPScatterplot.m

LSPBatchProcessing.m

PointOfSaturation.m

PerturbationUncertainty.m

A.5 Laser SOP

The laser start up SOP is:

1. Ensure that the lab is safe to operate the laser through mini risk assessment. Obtain permission to start the laser while informing all nearby individuals.
2. Obtain the necessary Personal Protection Equipment (PPE); laser grade goggles at the required Optical Density (OD) at the laser frequency.
3. Switch on the water chiller, establish that the coolant water is flowing into and out of the laser power supply.
4. Ensure that the door to the laser lab is closed. Double check PPE, do not remove until the laser is unplugged.
5. Switch on the laser warning light outside the lab.
6. Turn on the power to the laser at the wall socket.
7. Ensure that the laser energy meter/application is running and that the control computer is connected to the laser via USB cable.
8. Turn on the laser control laptop computer.
9. On the laser power supply, turn on the front key switch, and the rear power switch.
10. Test the functionality of the beam shutter.
11. Open the Thales laser operating software on the Laptop.
12. Click the run button. Wait and watch for errors.
13. If start up was successful, open the stepper motor application, reload settings from flash ensuring that doesn't move quicker than 400 steps per interval.
14. Block the beam path with closed beam shutter.
15. Set the pulse repetition rate divisor in the application.
16. Open the lasing shutter from the application.
17. Observe the output energy on the energy meter.
18. Adjust attenuator stepper motors until the desired energy output is obtained.

19. Allow at least 30 minutes for the laser to warm up.
20. Open and close the beam shutter to use laser in an experiment.

The shut down standard operating procedure:

1. Before shutdown, reduce output energy with the attenuator to less than 10 mJ at 1 Hz.
2. Close the lasing shutter.
3. Stop laser on the application.
4. Shut off power on the power supply rear switch, then front switch.
5. Close the Thales laser and stepper motor software on the laptop.
6. Shut off water chiller.
7. Turn off computers and warning light.
8. Turn off and unplug the laser at the wall socket to avoid damage from overnight power surges.
9. Remove PPE.

If there are any errors or abnormalities during start up, the laser is shut down and the start up procedure is repeated. If the laser fails to start up a second time, the test is aborted.
If the laser loses connection with the computer while running, every effort to shut down the laser within software is taken before cutting the power to the power supply.